DYNAMIC EARTHQUAKE RUPTURE SIMULATIONS IN THE SEA OF MARMARA

by

Yasemin Korkusuz Öztürk

B.S., Physics, Marmara University, 2008
M.S., Geophysics, Boğaziçi University, 2012

Submitted to the
Kandilli Observatory and Earthquake Research Institute
in partial fulfillment of the requirements for the degree of
Doctor of Philosophy

Graduate Program in Geophysics
Boğaziçi University
2019

DYNAMIC EARTHQUAKE RUPTURE SIMULATIONS IN THE SEA OF MARMARA

APPROVED BY:

Assoc. Prof. Dr. Ali Özgün Konca

(Thesis Supervisor; Boğaziçi University)...…………….…………………..

Prof. Dr. Nurcan Meral Özel

(Co-Supervisor; Boğaziçi University) …………….………………….

Prof. Dr. Semih Ergintav

(Boğaziçi University)   ……………….………………….

Prof. Dr. Şerif Barış

(Kocaeli University)   ……………….………………….

Assoc. Prof. Dr. Gülüm Tanırcan

(Boğaziçi University)   ……………….………………….

Assoc. Prof. Dr. Onur Tan

(İstanbul University)   ……………….………………….

DATE OF APPROVAL: 24.05.2019

Dedicated to

my mother Songül Korkusuz & my daughter

ACKNOWLEDGEMENTS

ABSTRACT

DYNAMIC EARTHQUAKE RUPTURE SIMULATIONS
IN THE SEA OF MARMARA

The 1912 Mürefte and 1999 Izmit M_w7.4 earthquakes are the last devastating events of the western and eastern sections of the Marmara region, respectively. The center of the Sea of Marmara, the region between locations of these two earthquakes, is prone to creating another large earthquake. The main objective of our study is to determine 3D dynamic earthquake rupture scenarios, considering non-planar and heterogeneous stress distribution in the Sea of Marmara. Recent studies show that some segments of the North Anatolian Fault (NAF) beneath Marmara are partially creeping. In this study, it is the first time that we attempt to generate realistic earthquake scenarios by putting constrains on initial stress on the fault using regional stress from earthquake focal mechanisms, in addition to stress release during past earthquakes and strain accumulation during interseismic period using geodetical measurements on slip-rate and locking depth at various segments along the NAF beneath the Sea of Marmara. In order to constrain the regional stress in addition to our previous five cluster analysis a new earthquake cluster is analyzed in the Central Marmara Basin. We use 3D Finite Element Method (PyLith) for dynamic earthquake simulations and tetragonal mesh for better smoothing at the fault bends, which allows us to implement nonplanar fault geometry and initial stress heterogeneity using slip-weakening friction law. We place constraints on initial shear stress from geodetic and seismic studies of locking depth and interseismic strain accumulation. We consider 80 rupture scenarios and calculate slip distribution, rupture velocity and moment magnitude in addition to slip-rate and traction on the fault surface, and displacement and velocity on the ground surface. We find that for the most scenarios possible earthquake magnitude does not exceed Mw7.2. In addition, in none of the possible scenarios we obtain super-shear rupture velocity. We find that depending on the location of the initiation point, asperities in the partially creeping segments and loaded initial stress, the rupture may not extend into the Prince's Island Segment.

ÖZET

MARMARA DENİZİ'NDE DİNAMİK DEPREM KIRILMASI MODELLEMELERİ

Büyüklüğü 7.4 olan 1912 Mürefte ve 1999 İzmit Depremleri, Marmara Bölgesi'nin doğu ve batı kesimlerinde meydana gelen son yıkıcı depremlerdir. İki depremin lokasyonlarının arasında bulunan Orta Marmara Denizi büyük bir deprem üretme yetkinliğine sahiptir. Çalışmanın hedefi Marmara Denizi'ndeki düzlemsel olmayan ve heterojen gerilim yüklü yapıları kullanarak üç boyutlu dinamik deprem kırılmaları modellemektir. Güncel çalışmalar KAF'ın Marmara'daki bazı segmentlerinin kaydığını göstermiştir. Bu çalışmada, deprem odak mekanizmalarından elde edilen bölgesel gerilim sonuçlarına ek olarak, Marmara Denizi içerisindeki KAF'ın segmentleri boyunca kayma hızı ve kilitlenme derinliği ile ilgili yapılmış jeodezik ölçümler, geçmiş depremlerde açığa çıkmış olan gerilim ve sismik aktiviteler arası yüklenen gerinimin kullanılmasıyla fay üzerindeki başlangıç gerilim miktarları sınırlandırılarak, ilk kez gerçekçi deprem senaryoları üretilmiştir. Bölgesel gerilimi kestirmek için, önceden incelediğimiz beş kümeye ek olarak Orta Marmara Havzası'nda yeni bir deprem kümesi analiz edilmiştir. Dinamik deprem simülasyonları için üç boyutlu sonlu elemanlar algoritması (PyLith) ve düzlemsel olmayan fay modelinin ve ilksel gerilim heterojenliğinin yavaşlayan-slip sürtünme modeline göre uygulanabilmesine olarak veren tetragonal gridleme yöntemi kullanılmıştır. Kayma gerilimi, jeodezik ve sismik çalışmalardan elde edilen kilitlenme derinliği ve sismik aktiviteler arası biriken gerinim yüklenmelerinden hesaplanmıştır. 80 tane kırılma senaryosu incelenmiş, fay üzerindeki kayma hızı ile gerilim ve yer yüzündeki hız ile yer değiştirmeye ek olarak, kayma dağılımı, kırılma hızı ve moment büyüklük hesaplamaları yapılmıştır. Senaryoların çoğunda depremin moment büyüklüğünün 7.2'yi geçmeyeceği görülmüştür. Hiçbir senaryo için yüksek kırılma hızı elde edilmemiştir. Ayrıca, depremin başlangıç noktası lokasyonuna, kısmen kayan segmentlerin içerisindeki kilitli kısımlara ve yüklenen ilksel gerilim miktarlarına göre kırılmanın Prens Adaları segmentine ilerlemeyebileceği görülmüştür.

TABLE OF CONTENTS

LIST OF FIGURES

LIST OF TABLES

LIST OF SYMBOLS

a_i	or	$\vec{a}$	Vector field a
a_{ij}	or	$\underline{a}$	Second order tensor field a
BB			Broad band
d_i	or	$\vec{d}$	Fault slip vector field
Erlt			Error of latitude
Erln			Error of longitude
Erdp			Error of depth
f_i	or	$\vec{f}$	Body force vector field
Lat			Latitude
Lon			Longitude
ML			Local magnitude
Mw			Moment magnitude
n_{ij}	or	$\vec{n}$	Normal vector field
P (Az)			Azimuth of pressure axis
P (Pl)			Plunge of pressure axis
Pl			Polarity
P	or	ρ	Mass density scalar field
SP			Short period
T (Az)			Azimuth of tension axis
T (Pl)			Plunge of tension axis
T_i	or	$\vec{T}$	Traction vector field
T_o			Initial traction at the along strike direction
T_y			Yield traction at the along strike direction
u_i	or	$\vec{u}$	Displacement vector field
Vp			Velocity of primary wave
Vs			Velocity of secondary wave
σ			Sigma, principal stress axis
σ_{ij}			Stress tensor field

LIST OF ACRONYMS/ABBREVIATIONS

2D	Two dimensional
3D	Three dimensional
BIEM	Boundary Integral Equation Method
BU	Boğaziçi University
CB	Central Basin
CMB	Central Marmara Basin
ÇB	Çınarcık Basin
ECMB	Eastern Central Marmara Basin
EÇB	Eastern Çınarcık Basin
EGO	Eastern Ganos Offshore
EH	Eastern High
ETB	Eastern Tekirdağ Basin
FEM	Finite Element Method
FMP	First Motion Polarity
FPS	Fault Plane Soltution
GS	Ganos Segment
IS	İzmit Segment
KB	Kumburgaz Basin
JAMSTEC	Japan Agency for Marine-Earth Science and Technology
JICA	Japan International Cooperation Agency
KOERI	Kandilli Observatory and Earthquake Research Institute
MarDiM	Earthquake and Tsunami Disaster Mitigation in the Marmara Region and Disaster Education in Turkey
MARsite	Marmara Supersite
MMF	Main Marmara Fault
MPI	Message Passing Interface
MRC	Marmara Research Center
NAF	North Anatolian Fault
NAFZ	North Anatolian Fault Zone

NEMC	National Earthquake Research Center
PI	Prince's Island Segment
SCEC	Southern California Earthquake Center
TB	Tekirdağ Basin
TETAM	Boğaziçi University
	Telecommunications and Informatics Technologies Research Center
TUBITAK	Scientific & Technological Research Council of Turkey
TRUBA	Turkish Academic Network and Information Center
ULAKBIM	Turkish Academic Network and Information Center
UTOKYO	University of Tokyo
WH	Western High

1. INTRODUCTION

Located between the collision zone of the Arabian and Eurasian plates the Anatolian block moves toward west 20-25 mm/yr along the North Anatolian Fault Zone (NAFZ) (Reilinger et al., 2006). Holocene and GPS derived slip-rates present increasing velocities from east to west (Reilinger et al, 2010; Dresen *et al.,* 2008; Şengör et al., 1985). The Marmara Region is located at the western end of the 1500 km long NAFZ, which is a dextral strike-slip faulting system extending from the Karlıova triple junction to the East and vanishing in the Aegean Sea. Due to being at the transition zone from the right lateral strike-slip faulting character of the NAFZ to the extensional structure of the Aegean Region, the seismotectonic feature of the Marmara Region is extremely complicated.

During the 20th century, significant number of large strike-slip earthquakes occurred along the NAFZ which was initiated by the M7.9 Erzincan Earthquake in 1939 and migrated westward (Parejas *et al.,* 1942). The latest rupture terminated at the eastern end of the Main Marmara Fault (MMF).

1912 Ganos Earthquake in the Western Sea of Marmara and the 1999 İzmit Earthquake in the Eastern Sea of Marmara are the last destructive earthquakes in the Marmara Region where recurrence intervals of large earthquakes near İstanbul is almost one century (Gürbüz *et al.,* 2000). Also, the western end of the rupture of the 1999 İzmit event might have propagated below the Çınarcık Basin (Wright *et al.,* 2001; Çakır et al., 2003). Despite uncertainties about the slip distribution, it is clear that a major seismic gap exists between the ruptured zones of 1912 Ganos and 1999 Izmit earthquakes.

A critical question about the Marmara Seismic Gap is that why it has not ruptured during the last 250 years considering that no large earthquake is recorded since 1766? One possible explanation is the heterogeneity of strain accumulation during the interseismic period. If the strain accumulation is less than the plate rate of ~20 mm/yr this would explain the lack of large events beneath Marmara in comparison to Ganos and Izmit segments. In

addition, the heterogeneous strain accumulation may be the reason for the time extention of the next devastating earthquake.

Recent studies present that the Central Marmara segment is creeping while the Çınarcık segment is locked down to around 10 km in terms of KOERI catalogue (Klein et al., 2017; Schmittbuhl et al., 2016; Ergintav et al., 2014) or 7 ± 3.2 km depth (Korkusuz Öztürk and Meral Özel., 2018). On the other hand, locking issue of Tekirdağ and Kumburgaz segments are still under debate considering less seismicity in the central Marmara, repeating earthquakes in the Western High and Central Marmara Basin (Bohnhoff et al., 2017; Schmittbuhl and Karabulut, 2016), and lack of slip deficit in the Central Marmara (Klein et al., 2017; Ergintav et al., 2014).

In order to achieve a better understanding on rupture propagation properties and damage levels of earthquakes, generation of realistic dynamic earthquake fracture simulations are very important. Regarding to slip distribution results from dynamic simulations, ground motion and tsunami models can be derived, as well. Discovering physical and chemical process of an earthquake rupture is a challenge and can be investigated by fully dynamic and spontaneous earthquake rupture simulations. The geometry is very important to define rupture progress (e.g., Aochi et al., 2015 and 2003; Douilly et al., 2015; Fukuyama and Hao, 2013; Oglesby et al., 2012 and 2003; Kase, 2010; Aochi and Kato, 2010; Harris and Day, 1999), as dynamic simulations are fault constitutive. Most of the dynamic earthquake fracture models in the world are done for the subducting fault models through the usage of post-earthquake information (e.g. Tsuda et al., 2017; Douilly, ve diğ., 2014; Kozdon and Dunham, 2013). The main problem for the future dynamic modelling is the estimation of stress on the fault that is generally nonhomogeneous. Identification of medium parameters is also another significant issue.

Dynamic earthquake rupture simulations rely upon magnitudes of initial maximum, intermediate and minimum principal stress axes, and define slip and slip-rate occurred on the fault surface, and displacement and velocity on the ground surface via the stress drop on the fault surface. A rupture can extend with the transferred stress from an initiation point to its surrounding area and may continue to extend with the transferred stress to the neighboring elements. The start and extend of a rupture depend on the total (initial+incoming) stress on

the sub-faults. When the friction criterion is not satisfied (total stress in not large enough) rupture terminates. Slip weakening friction models are used to calculate final slip and stress on the fault surface. Identification of initial stress, crustal velocity and frictional parameters are significant to derive realistic earthquake properties. On the other hand, calculation of stress amounts and frictional parameters are extremely difficult, so globally assumed stress and friction parameters are generally used for future earthquake analyzes. Since stress kernels of the problem has to be calculated for each time step at each sub-fault, dynamic simulations require super computers and parallel programming. As a result, the application of numerical dynamic earthquake rupture simulations is a challenge due to high computational demand, being too lengthy, having singularities depending on the used approach and boundary conditions, and restricted applicability of complex fault geometries.

Several studies focused on dynamic rupture simulation in the Marmara Region up to this date. One of them is performed for the 1999 Düzce earthquake using kinematic inversion data to constrain dynamic rupture parameters on the planar fault (Tanircan et al., 2017). Other two are done for possible events in the Sea of Marmara considering the nonplanar MMF. These previous studies of dynamic rupture simulations consider the 3D fault geometry and whether it would be possible to break the whole unruptured segments in one large earthquake or the rupture would be segmented due to complex geometry. Aochi and Ulrich (2015) model the eastern part of the MMF including the Central Marmara Basin and use a Boundary Integral Equation Method. Oglesby and Mai (2012) model the whole MMF using a Finite Element Model. In both forward models, a homogeneous and regional stress regime is assumed and rectangular mesh type is used. A common result of both of these studies is that rupture does not propagate to the PI segment for ruptures that initiate from eastern Marmara and super-shear rupture is observed. Especially in the model of Aochi and Ulrich rupture does not enter into the PI fault segment in any case. In addition, Oglesby and Mai (2012) deliver that 10º rotation in the strike angles of initial stresses is very important leading large changes in results.

One element missing in previous MMF studies is the heterogeneity of the stress distribution in the region (Aochi and Ulrich, 2015; Oglesby and Mai, 2012). Usually, as a first order approximation, a homogeneous regional stress is projected on to the fault planes. However, the initial stress can be heterogeneous depending on the coupling on the fault

plane, the past rupture history, and slip-rate on the fault. Recent geodetic and seismic studies show that the slip-rate and historical events on different segments are not the same for the MMF.

The objective of this study is to generate realistic 3D dynamic earthquake rupture simulations in the Sea of Marmara considering stress heterogeneities on the non-planar geometry. In order to achieve this objective, we combine several factors that contribute to the heterogeneous stress distribution; we refine the regional stress from focal mechanisms, use the geodetic slip-rates on faults and locking on each fault segment using the elapsed time since the last major earthquake for the initial stress conditions. We start by combining findings of historical earthquake data (Ambraseys, 2009; Ambraseys, 2002; Guidoboni et al., 1994; Soysal et al., 1981) and turbidity records (Drab at al., 2015; McHugh et al., 2014; Drab et al., 2012; and McHugh et al., 2006) to investigate elapsed time since last large earthquake and rupture extend of the last earthquake for each fault segment. Next, we calculate initial stress values and frictional values by the help of recent seismic (Korkusuz Öztürk et al., 2015; Korkusuz Öztürk and Meral Özel, 2018; Pınar et al., 2016; and MarDiM Project) and geodetic (Klein et al., 2017; Ergintav et al., 2014; Hergert and Heidbach, 2010) results. Some parts of the seismicity analyses are done as part of this study, as well (Chapter 3). We work on different methodologies, 2D and 3D BIEM and 3D FEM, to have a better understanding on earthquake source processes and select the most suitable approach for our heterogeneously stressed non-planar fault geometry. In addition, we take into account recent findings of repeating earthquake studies to adapt creeping and locking parts of the fault segments in the Central Marmara Sea (Yamamoto et al., 2019; Bohnhoff et al., 2017; and Schmittbuhl et al. 2015). Consequently, we generate 80 different dynamic simulation cases for the expected large Marmara earthquake considering the non-planarity and stress heterogeneity of the MMF using a Finite Element Method (PyLith).

In this study, we make forward dynamic earthquake rupture modellings for the expected devastating Sea of Marmara earthquake which completed its occurrence period considering recurrence intervals of previous $M \geq 7.0$ earthquakes. One critical element in dynamic rupture simulations is to put constraints on initial stress distribution.

This thesis consists of 7 chapters in total. The introductory chapter gives a brief information about the study area, studies related to our investigations, basic concepts in dynamic earthquake scenarios and a summary of our analyzes.

Chapter 2, not only mention about the tectonic setting of the Marmara Region, but also introduce results of our research on the combination of historical earthquake catalogues and turbidity records. Also, recent slip-rates from latest geodetic studies are represented.

In chapter 3, our earthquake relocation and stress tensor inversion study in the Eastern Central Marmara Basin, and relative location process of six clusters of earthquakes in the Sea of Marmara are given. These analyses are done in order to calculate orientations of maximum principal compressive stress axes and visualize vertical alignments of earthquakes.

In chapter 4, a dynamic rupture simulation code based on a 2D BIEM is written. Our stress and slip velocity field results are compared to the results of the refence study (Cochard and Madariaga, 1994). In addition, time dependent slip-rate results are presented. In the second part of this section, our experience on a 3D BIEM is given (Ando, 2016).

In section 5, details about 3D dynamic earthquake rupture simulation code (PyLith) that we use for the creation of scenarios in the Sea of Marmara are given. Also, our fault models for different initial shear traction distributions are given. In section 6, 3D dynamic earthquake rupture simulation results of the MMF for the given initial models in section 5 are presented, and obtained results are discussed. Finally, chapter 7 concludes this thesis with a summary of findings as a result of 3D dynamic earthquake rupture simulations in the Sea of Marmara.

2. TECTONIC SETTING AND SEISMIC ACTIVITY OF THE MARMARA REGION

2.1. Tectonic Setting

The complex tectonic structure of the Marmara Region is controlled by the dextral strike-slip motion of the 1500-km long North Anatolian Fault Zone (NAFZ) that starts from the Karlıova triple junction in the east and enters to the Aegean Sea in the west. The NAFZ accommodates westward motion of the Anatolian block relative to Eurasian block due to the collision between Arabian and Eurasian Plates and rollback along the Hellenic subduction zone (Reilinger et al., 2010). The Marmara Sea Basin is about 230 km long and 70 km wide. It has a shallow shelf to the south and five sub-Basin at the north which are Tekirdağ, Central, Çınarcık, Karamürsel, and İzmit Basin (Ambraseys, 2002) from west to the east. Transtensional and transpressional zones attribute to the unclear features (Dewey *et al.,* 2012) illustrating that Marmara Region is a complex tectonic region.

The NAFZ, which bifurcates into three main strands in the Marmara Region, has complex features. The northern branch enters to the İzmit Gulf by passing through Sapanca Lake, the central one forms the Gemlik Gulf, and the southern strand enters to the İznik Lake and Bursa region with its central and south parts. The Northern branch of the NAF in the Sea of Marmara forms the extensional Princes Island's segment at the west of the İzmit Gulf, while the Main Marmara Fault has primarily dextral strike-slip characteristics. On the other side, the Ganos Segment in the the MMF comprises small extensional and thrust earthquakes.

Moreover, Tekirdağ Basin has the highest sedimentation being in accord with the steep subsidence near the fault branch as defined in Seeber et al. (2004) (Drab et al., 2012). The Central Basin has simultaneous mass wasting events with the Tekirdağ Basin (Drab et al., 2012).

Several models of evolution of Marmara Region is suggested including debated for Pull-apart, En-echelon, and Master Fault models (Yaltırak, 2002; Imren et al., 2001; Aksu et al., 2000; Okay et al., 2000; Siyako et al., 2000; Le Pichon et al., 1999; Parke et al., 1999; Ergün and Özel, 1995; Wong et al., 1995; Barka, 1992; Barka and Kadinsky-Cade, 1988). In the current study, we use a model from a multi-beam bathymetry and high resolution multichannel seismic reflection study (Le Pichon et al., 2003) which gives significant information about the tectonic and morphological structure of the Sea of Marmara.

2.2. Historical Earthquake Activity in the Sea of Marmara

Recurrence relations and characteristics of historical earthquakes are important in order to evaluate occurrence time and determining the stress build up for potential future events. Considering the non-planarity of the MMF, some segments can be broken on their own or a few of them can rupture together (Oglesby and Mai, 2012; Armijo et al., 2005; Le Pichon et al., 2001). The main difficulty is that we don't know exact locations of earthquakes. Thus, it is difficult to identify recurrence relations, exact rupture extensions, and fault characteristics of the historical events from the paleo-seismology or historical human based records. On the other hand, considering that our goal is to generate the most realistic earthquake simulations in the Sea of Marmara, selection of the best combinations of rupture extensions and recurrence intervals of historical earthquakes is crucial.

We consider historical earthquake records with M≥7.0 in the Sea of Marmara via previous earthquake catalogues (Başarır Baştürk et al. 2017; Ambraseys, 2009; Ambraseys, 2002; Ambraseys and Jackson, 2000; Ambraseys and Finkel, 1995; Guidoboni et al., 1994; Soysal et al., 1981), as their effect on state of stress is higher in comparison to M~6.0 events. Possible epicenter locations of historical earthquakes with intensities ≥IX are presented in Fig 2.2.1 although evaluations of their sizes are debated. For example, 860-861 and 68-69 events can be single events considering possible misinformation. Also, if we focus on the latest historical events, occurrences of two magnitude ≥7.0 earthquakes in the Çınarcık Basin (1754 and 1766) within 12 years are not realistic, so one or both of them might have occurred at different fault segments. Similar arguments can be made for the 1343 and 1354 Ganos earthquakes, as well.
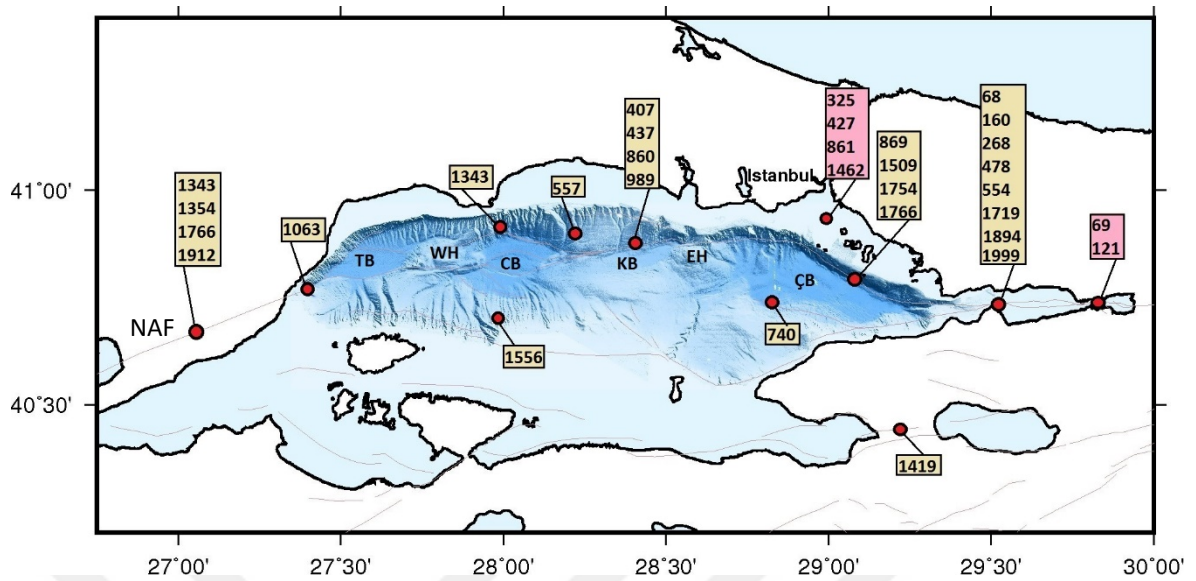
Figure 2.1. The occurrence years and possible locations (red dots) of historical destructive earthquakes from Ambraseys (yellow boxes; 2002) and others (pink boxes; Ambraseys, 2009; Ambraseys, 2002; Guidoboni et al., 1994; Soysal et al., 1981).

Considering unclear event locations and lack of rupture extension information from the historical earthquake data, we mainly focus on recent paleoseismological records, such as coring at the deepest parts of the Basin which contains turbidity records involving traces of previous events even from a few thousand years before (McHugh et al., 2014; Drab et al., 2012; Çağatay et al., 2012; Beck et al., 2007; McHugh et al., 2006). Recent turbidity records present imprints of 740 AD the earthquake in the Tekirdağ, Central and Çınarcık basins, while the signs of the 860 AD event are found in the Tekirdağ Basin, Central Basin and in the İzmit Gulf (Fig.2.2.2). Occurrences of two large earthquakes to fracture the whole MMF within 120 years show the rupture complexity of the MMF. More than one ruptures might have existed during the 740 AD and 860 AD earthquakes, as it is the case for 1343 earthquake including two major shocks within a few hours (Ambraseys, 2009). Besides, finding no core sample in the Çınarcık Basin for the 860 AD event is another question, but core data may not be available for every event.

Combination of all seismicity-turbidity records shows that large earthquakes in the Western Marmara Sea occurred in 268, 557, 740, 860, 1063, 1343, 1766 and 1912 (Fig.2.2.1) with the time intervals of 289, 183, 120, 203, 280, 423 and 146 years, respectively. Since

423-year time interval is very long, looking at the historical records, 1462 (IX) and/or second 1509 (23 October, VIII) earthquakes have high possibility to be occurred in the Western Marmara Sea. For the Eastern Marmara Sea, earthquakes are recorded for 325, 427, 861, 1462, 1509, 1754, 1766 and 1894 (Fig.2.2.1) with the time intervals of 102, 434, 601, 47, 245, 12, 128, respectively, showing aperiodic earthquake sequences. Earthquake occurrence intervals are further complicated in the Eastern Marmara Sea due to the bifurcation of the NAF in the İzmit Gulf, so some of these earthquakes should be located at the southern branch. Therefore, recurrence interval of the earthquakes in the Çınarcık Basin is unclear, while it may be ~140 years in terms of Pondard, et al. (2007).

McHugh et al. (2006) and Drab et al. (2015) obtain seismicity-turbidity relations for 268, 557, 740, 860, 1063, 1343 and 1912 earthquakes in the Tekirdağ Basin (Fig.2.2.2). Interestingly, they do not find samples for the 1766b event as it is expected from the historical data.

In terms of seismicity-turbidity results of McHugh et al. (2014), eastern extensions of the ruptures of 1063 and 1912 Western Marmara earthquakes reached up to the Tekirdağ Basin, and 1912 earthquake also can be traced along the Western High (Fig.2.2.2). No indicator of the 1766b event is obtained, but signs of 740, 1509, 1766a and 1894 earthquakes are found in the Çınarcık Basin. On the other hand, it is difficult to be sure if 1894 rupture is on the northern (Princes Islands Fault) or southern branch of the Çınarcık Basin, since the core location is almost at the center of the Basin. Besides, exactly the same implications are obtained in the Hersek Delta comparing with the Çınarcık Basin. A submarine study presents the western extension of the 1999 rupture terminating at the eastern end of the Çınarcık Basin which may act as a barrier with its normal faulting mechanism (Uçarkuş et al., 2011). Also, considering the historical records in the Sea of Marmara and in the İzmit Gulf, 740, 1343 and 1509 earthquakes should include sedimentary records in the Çınarcık Basin (McHugh et al., 2014). Hence, McHugh et sl. (2014) visualize indicators of 180, 268, 358, 740, 860, 1296, 1509 and 1999 earthquakes in the İzmit segment. In addition, seismicity-turbidity correlations of Çağatay et al. (2012) at the İzmit Gulf also overlap with the results of McHugh et al. (2014).
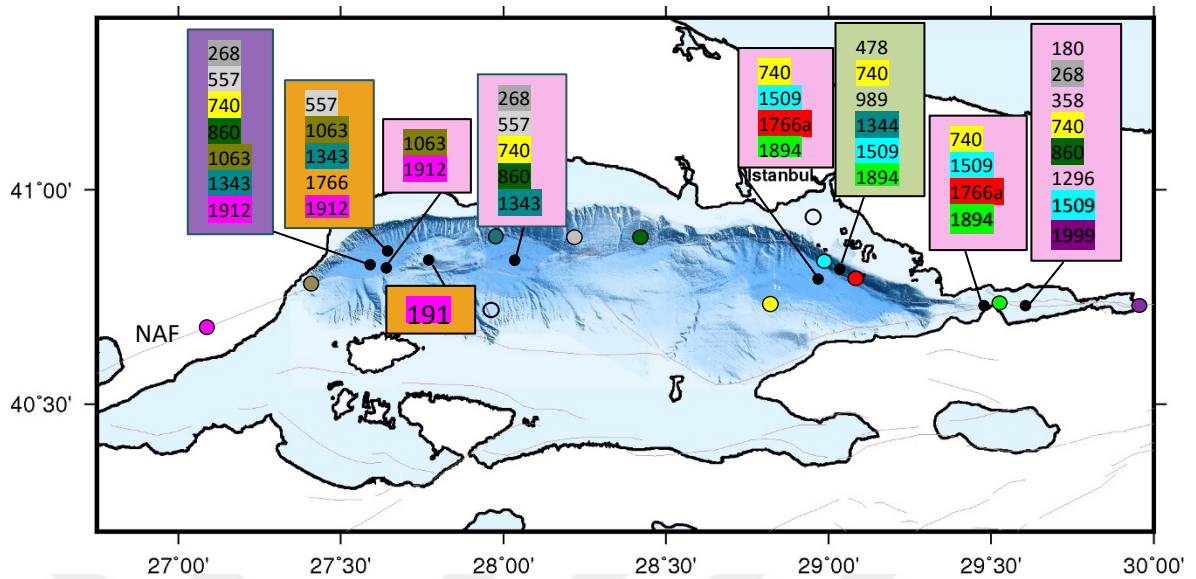
Figure 2.2. Purple is from McHugh et al. (2006) and Drab et al. (2013), orange rectangles are from Drab et al. (2012), the green rectangle is from Drab et al. (2015), and pink rectangles are from the turbidity results of McHugh et al. (2014). Colorful dots are the possible epicenters of the previous earthquakes in the Sea of Marmara. Each color represents the related earthquake as its occurrence date is written with the same highlight. The 1963 and 1964 earthquakes (M6.4) in the Marmara Sea are ignored due to their relatively smaller sizes.
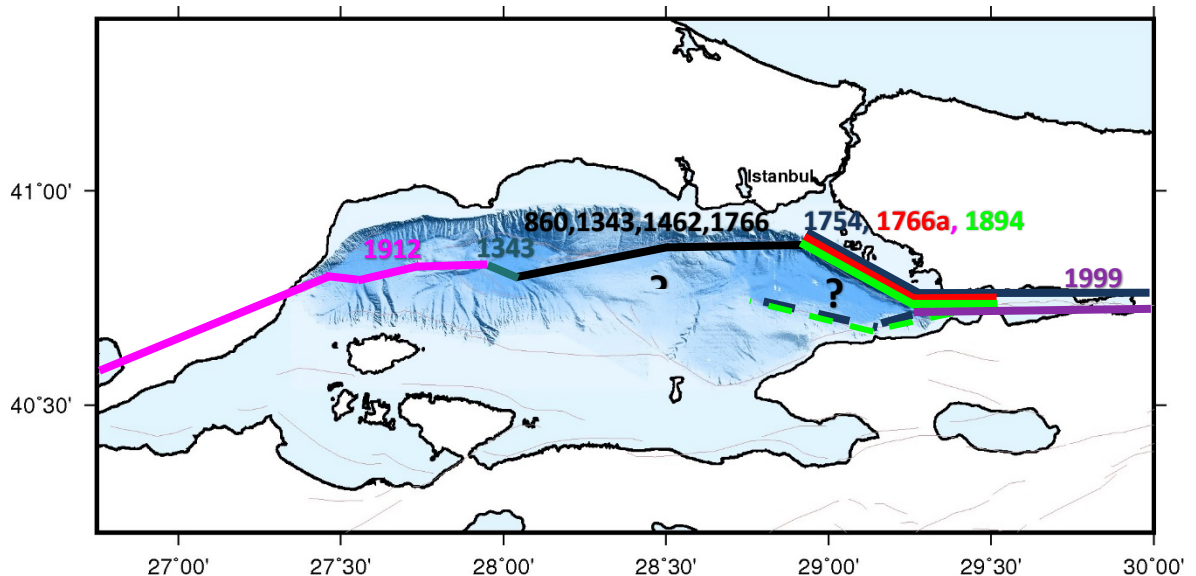
Figure 2.3. The most possible rupture extensions of the latest M≥7.0 earthquakes in the main strand of the MMF.

Drab et al. (2012) find out relations for 557, 1063, 1343, 1766 and 1912 earthquakes in the Tekirdağ Basin and the 1912 earthquake in the Western High via their turbidity study (Fig.2.2.2). They state a sedimentary imprint of the 1912 earthquake in the Central Basin due to the rupture on the Tekirdağ Basin. Also, they attribute the low number of seismo-turbidities and high chemical diversity in the Central Basin comparing to the Tekirdağ Basin as representatives of the shallow creep in the Central Marmara Sea. On the other side, a seismicity study proposes that not only the Central Basin, but also the Western High and the Tekirdağ Basin are creeping at shallow parts of the segments (Schmittbuhl et al., 2015).

In this study, we also try to identify the rupture extensions of the latest earthquakes located at the northern branch, main strand, of the MMF. The Western Sea of Marmara is last ruptured, 146 years after the 1766b earthquake, in 1912, and combinations of seismicity, turbidity and historical data sets indicates the rupture termination at the western entrance of the Central Basin (Fig.2.2.3). In the Central Basin no turbidity information exists since 1343, and the Kumburgaz Basin is also silent for a long time. Considering the lack of evidence from paleoseismologic data about the latest events in the Central Marmara Sea, and recent studies from geodesy and seismicity support creep in the central segments of the MMF (Schmittbuhl et al., 2015, Ergintav et al., 2014).

Parsons (2004) presents that only the northern (PI) segment of the Çınarcık Basin ruptured during the 1754 event although historical data indicates that İzmit is the epicentre of his event, but large damage occurred in İstanbul, as well (Ambraseys, 2009). Indeed, the intensity of this earthquake is defined as IX (Soysal et al., 1981), and it is very large for a rupture only on the PI segment. Considering slip deficit distributions with Coulomb stress interactions, Pondard et al. (2007) present their most plausible rupture scenarios. One of them is that the northern segment is broken by the 1894 event and the southern one is by the 1754, and the other possibility is vice versa, via assuming the 1766a rupture did not propagate into the Çınarcık Basin. Nevertheless, recent seismicity-turbidity studies have findings of the 1766a event in the Çınarcık Basin, and even near the Hersek Delta. Therefore, neither the date of the latest event nor the extension of it could be defined accurately in the Çınarcık Basin. On the other hand, Drab et al. (2015) obtain records of the 1894 earthquake on the PI fault segment.

Despite significant uncertainties about the rupture extent of the historical earthquakes, they still give the best information about the stress build up on the fault zones in the region. Our final interpreted historical earthquake rupture extensions are shown in Figure 2.2.3.

2.3. Seismicity and Geodetic Slip-Rates along the MMF

In order to understand current fault behavior and characteristics in the Sea of Marmara, fortunately, scientists are able to use instrumental data and can analyze recent seismicity and surface deformations in detail (Korkusuz Öztürk and Meral Özel, 2018; Schmittbuhl et al., 2016; Korkusuz Öztürk et al. 2015; Schmittbuhl et al., 2015; Ergintav et al., 2014; Karabulut et al. 2011; Örgülü 2011; Bulut et al. 2009; Pinar et al. 2009; Sato et al. 2004; Tunç et al. 2011; Karabulut et al. 2002; Özalaybey et al. 2002; Örgülü and Aktar 2001; Gürbüz et al. 2000).

Ganos Onshore, in the west, is locked up to 9±2 km or 14 km (Ergintav et al. 2014; Schmittbuhl et al. 2015, respectively), as shown by very little background seismicity which is a characteristic of a fully locked fault zone. Geodetic evidence also shows that Ganos segment is a locked fault zone. The seismogenic zone extends from 2 km to 17 km depth at the complex Eastern Ganos Offshore segment with its branches (Korkusuz Öztürk et al., 2015).

The sedimentary thickness of the Tekirdağ Basin is ~5.5 km (Bayrakçı et al. 2013). The main earthquake activity at the Eastern Tekirdağ Basin area is located between 9-15 km in terms of the study of Korkusuz Öztürk and Meral Özel (2018) for the crustal structure from Karabulut at al. (2003) using data from land and OBS stations, or it is located between 10 - 26 km depths in terms of the study of Yamamoto et al. (2017) considering fault structure from Yamamoto et al. (2015) with data from only OBS stations, or it is located between 0 - 20 km depths in terms of study of Wollin et al. (2018) considering the velocity model of Karabulut et al. (2011) with data from land stations. Also, the region is defined as deep creeping above ~15 km (Schmittbuhl et al., 2015), instead of above ~10 km (Sakıç et al., 2016; Korkusuz Öztürk et al., 2015). Considering the attributed aseismic creep (Schmittbuhl et al., 2015) and occurrence of moderate size (ML4.5–5.2) earthquakes with one year intervals since 2008, this segment may not be accumulating stress at the plate slip-rate

(Korkusuz Öztürk and Meral Özel, 2018). Furthermore, a recent study using underwater dilatometers measures 4-8 mm/yr strain rate in the Tekirdağ Basin region (Yamamoto et al., 2016).

The sedimentary layer of the Central Basin is ~6 km (Bayrakçı et al., 2013), and the strike-slip strain rate is 2 mm/yr (Ergintav et al, 2014). The seismically active area is located between 10.5 - 14 km or 7 - 14 km depth intervals (Yamamoto et al., 2017; and Korkusuz Öztürk and Meral Özel 2018, respectively).

For the Çınarcık Basin area, the sediment layer is between 1.5 and 3 km (Bayrakçı et al., 2013), and the vertical dipping angle is around 70˚ (Oglesby and Mai, 2012). Extension of the region is 6±2 mm/yr and while right-lateral offset is 15±2 mm/yr, as a result of a GPS study (Ergintav et al. 2014). In addition, the seismic zone seems to be between 8 km and 13 km depths in the Eastern Çınarcık Basin (Korkusuz Öztürk et al., 2015). Moreover, the Çınarcık Basin should be locked up to ~7 km (Korkusuz Öztürk and Meral Özel, 2018) or ~10 km (Klein et al. 2017; Schmittbuhl et al. 2015; Bohnhoff et al. 2013).

Consequently, it is challenging to identify sedimentary layer thicknesses, seismic zone intervals, earthquake histories and stress orientations rigorously from historical data and recent instrumental data. Findings reveal that earthquakes in the Sea of Marmara may not be periodic. Therefore, we try to promote segmentation details (locking percentages and layer depths) and estimation of loaded stresses through the use of combinations of geodetic and seismic studies. In the current study, we do not consider sedimentary thicknesses owing to their inaccuracies and the complexity of our fault model.

3. A STRESS TENSOR ANALYSIS IN THE CENTRAL MARMARA BASIN AND RELATIVE LOCATIONS OF SIX CLUSTERS OF EARTHQUAKES IN THE SEA OF MARMARA

3.1. Introduction

The 9 August 1912 Mürefte earthquake with Mw7.4 (Aksoy et al., 2010) in the west and 17 August 1999 İzmit earthquake with Mw7.4 (Barka et al., 2002) in the east are the last destructive events in the Marmara Region. A 70-150 km long seismic gap exists between the extensions of these events (Geli et al., 2008; Barka et al., 2002; Hubert-Ferari et al., 2000; Ambraseys and Finkel, 1987), and no destructive earthquake have been recorded in the Central Marmara Sea, since the 22 May 1766, destructive İstanbul earthquake. On the other hand, rupture extensions of the latest earthquakes are still argued (Korkusuz Öztürk et al., 2015; Bouchon et al., 2002; Özalaybey et al., 2002; Pınar et al., 2001; Wright et al., 2001). As a result, a large earthquake is expected in the Sea of Marmara (Erdik, 2013; Erdik et al., 2004; King et al., 2001), so detailed earthquake relocation and stress axes orientation analyzes are significant.

The strain-partitioning, rotated stress axes (Korkusuz Öztürk et al., 2015) and lack of strain accumulation in the Central Marmara Sea (Ergintav et al., 2014; Ergintav et al., 2007), increase the complexity of the recent stress state analyzes. Current seismic studies reveal normal fault structures in the Eastern Marmara Sea (Korkusuz Öztürk et al., 2015; Karabulut et al., 2011; Bulut et al., 2009; Pınar et al., 2009; Sato et al., 2004; Tunç et al., 2011; Karabulut et al., 2002; Özalaybey et al., 2002; Örgülü and Aktar, 2001), even though previous investigations (Le Pichon et al., 2001; Gürbüz et al., 2000) support a pure dextral strike-slip stress regime in the Marmara Region. On the other side, the central Marmara Sea studies are limited due to the insufficient seismicity information and small number of seismic and geodetic stations.

Some of the latest studies prefer to handle P-wave first motion polarities technique in order to derive the complex stress and strain structures in the Sea of Marmara and its surroundings (Korkusuz Öztürk et al., 2015; Örgülü, 2011; Pınar et al., 2009; Polat et al., 2002; Gürbüz et al., 2000), while others, prefer moment tensor inversion techniques using larger events (Pınar et al., 2003; Kiratzi 2002). Furthermore, a relative location study for the aftershock activity of the 1999 İzmit earthquake using HYPODD method in the Yalova area (Bulut and Aktar, 2007) figures out a northward dipping fault with an angle of 56°. Thus, no relative location study is done previously in the Sea of Marmara using natural seismicity due to the low signal detection capabilities increasing errors and decreasing realistic analyzes of event clusters. On the other hand, the signal detection capability in the Sea of Marmara rises in time because of the increment in the number of land and sea seismic stations, originates from some recent projects (TURDEP, MARsite, MarDiM).
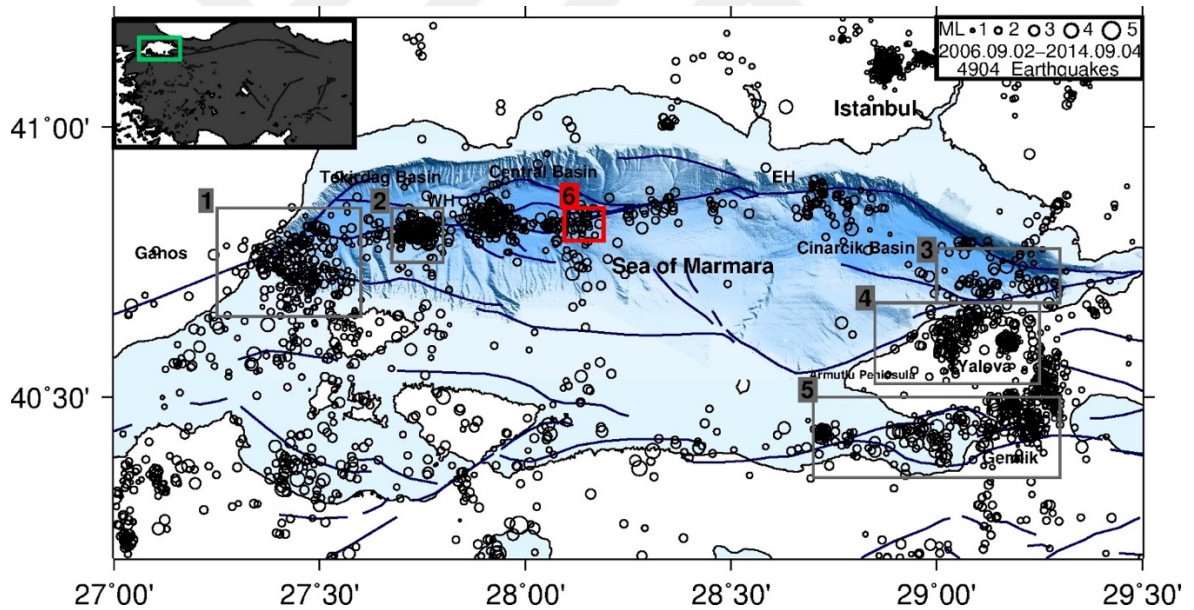
Figure 3.1. The seismic activity between 02.09.2006 and 04.09.2014 in the Marmara Region taken from the earthquake catalogue of the KOERI (Korkusuz Öztürk and Meral Özel, 2018). Black circles represent ML≥1.0 earthquakes. Grey rectangles are our previously analyzed event clusters; Eastern Ganos offshore (1), Eastern Tekirdağ Basin (2), Eastern Çınarcık Basin (3), Yalova (4) and Gemlik clusters (5) (Korkusuz Öztürk et al., 2015). The red rectangle shows the Eastern Central Marmara Basin cluster (6). Fault and bathymetry data are from Armijo et al. (2002) and Rangin et al. (2001), respectively.
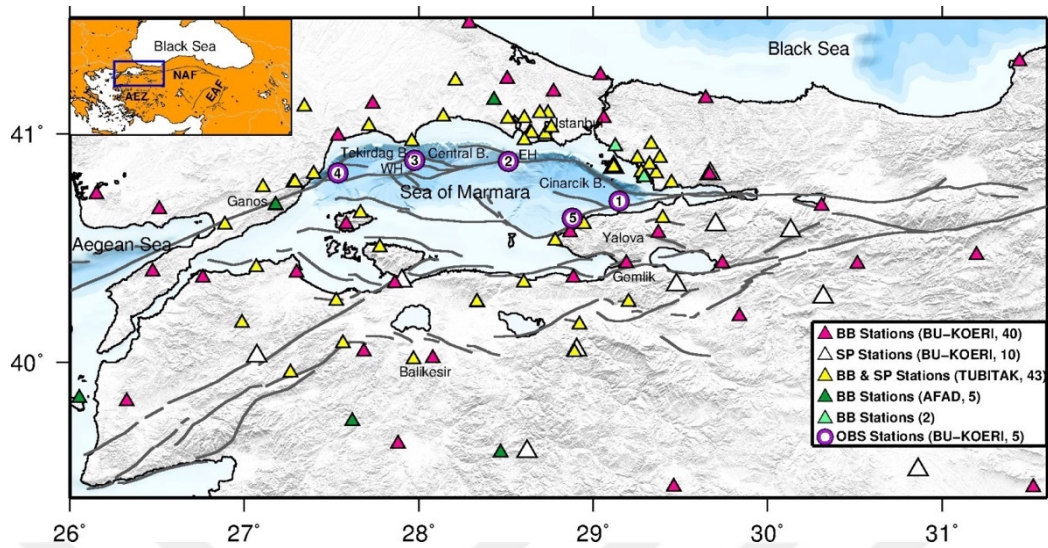
Figure 3.2. The station distribution map (Korkusuz Öztürk and Meral Özel, 2018). Pink and white triangles are BB (40) and SP (10) stations of KOERI, respectively. Yellow triangles present BB and SP (43 in total) stations of TUBITAK (Inan et al., 2007). Dark green triangles are BB (5) stations of AFAD and light green triangles are BB (2) stations of other constitutions. Purple circles depict real-time continuous observation points of KOERI (Korkusuz Öztürk et al., 2015). Fault traces on the main figure are from Armijo et al. (2002), while fault traces on the legend are from Şaroğlu et al. (1992). The topographic and bathymetry data are from Reuter et al. (2007) and Le Pichon et al. (2001), respectively.
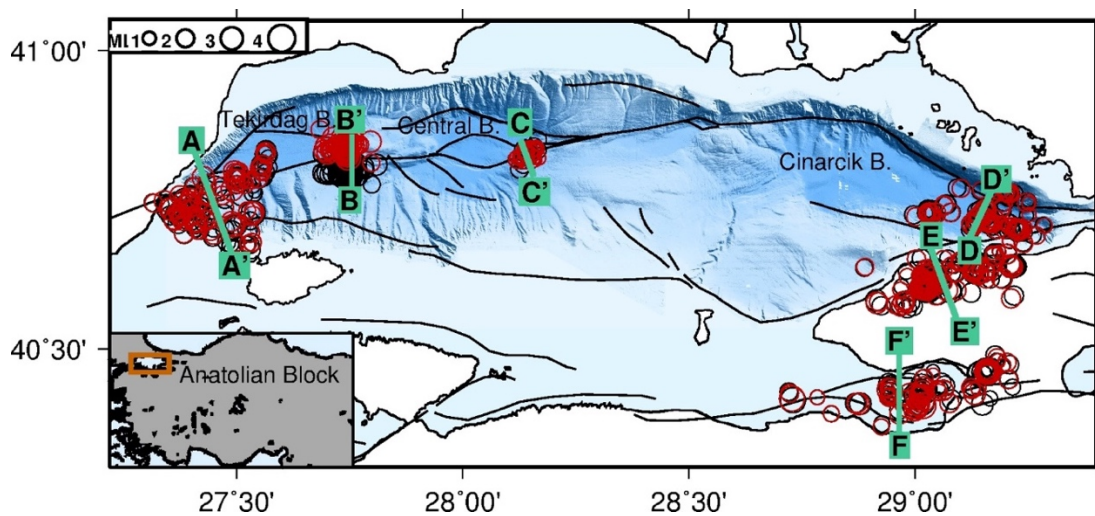
Figure 3.3. The map of epicenters of individual (black circles), and relative locations of earthquakes (red circles) within the six visible clusters (Korkusuz Öztürk and Meral Özel, 2018). Green profiles are for the fault perpendicular cross sections.

We derive maximum, intermediate and minimum principle stress axes (σ_1, σ_2 and σ_3) in the Eastern Central Marmara Basin earthquake cluster. A homogeneous local state of stress is assumed to allow us to linearize the stress-strain relationship and decrease the elasticity tensor to the Young's modulus. 27 of 53 events are selected in order to figure out concurrent fault plane solutions and principal stress axes orientations (Horiuchi et al., 1995). Unlike the study of Örgülü (2011), obtaining a right lateral strike-slip state of stress in the northwest of the CMB, we find out an extensional state of stress in the eastern CMB. In addition, we derive relative locations of six clusters of earthquakes; Eastern Ganos offshore (EGO), Eastern Central Marmara Basin (ECMB), Eastern Tekirdağ Basin (ETB), Çınarcık Basin (CB), Yalova (Y) and Gemlik clusters (G). Stress tensor inversion analyzes of five of these clusters are previously done by Korkusuz Öztürk et al. (2015). Although our main goal was to identify dipping angles of the fault segments in the Sea of Marmara by the relative relocation technique, the vertical alignments of the fault segments are not clear. On the other side, we can identify seismically active zones. As a result, we have the chance to compare and interpret creeping and locking parts for each segment.

3.2. Data and Methodology

The joint data and the methodology of individual locations, focal mechanism solutions and stress tensor inversions for the ECMB are exactly the same with our previous analyses (Korkusuz Öztürk et al., 2015). Namely, data from stations of TUBITAK, KOERI and AFAD are merged, and 100 land and 5 OBS are benefited in total. The time span is 2006.09.02-2014.09.04, and 27 of 53 events are selected after the elimination in terms of having at least 10 high quality P-wave first motion polarities. In order not to affect polarities, no filter is used. Pql-II program is (Boaz, 2009) is preferred for the data observation.

Earthquakes which are not further than 2 km are selected to be in the ECMB cluster. Events are located based on the crustal model from Karabulut et al. (2003), and the Vp/Vs ratio is selected as 1.75 owing to giving the minimum location errors (Table 3.1). Locations are done via hypocenter method (Lienert and Havskov 1995; Lienert 1991; Lienert et al 1986). Stations further than 200 km are not included in any part of the progress.

Next, stress tensor orientations of the ECMB are derived via the approach of Horiuchi et al. (1995). This method uses actual P-wave first motion polarities and useful especially for local earthquake clusters. As a result, it calculates orientations of maximum, intermediate and minimum principal stress axes (Table 3.2). Tables 3.1 and 3.2 represent location and stress orientation details for EGO, ETB, EÇB and ECMB clusters which are important staying on the MMF to make 3D dynamic rupture simulations.

Table 3.1. The average errors come from relocations. The azimuthal GAP in station coverage, depth (Erdp), latitude (Erlt) and longitude (Erln) are presented. Minimum (Min), maximum (Max), average (Av) and total (Tot) number of used polarities, and the total number of inconsistent stations (Misfit Polarity) for the selected cluster.

Cluster	Cross Section	Av-Gap (°)	Av-Erdp (Km)	Av-Erlt (Km)	Av-Erln (Km)	Min/Max/Av/Tot-Polarity	Misfit Polarity
1-EGOC	AA'	65±21	2.6±0.93	1.0±0.23	1.2±0.32	10/58/21/1768	22
2-ETBC	BB'	58±23	3.1±0.85	1.2±0.21	1.4±0.29	10/65/28/2063	28
3-ECBC	CC'	64±22	2.8±0.69	0.8±0.16	1.2±0.22	10/44/20/1494	12
4-YC	DD'	55±22	2.5±0.85	0.9±0.23	1.2±0.24	10/63/23/2336	23
5-GC	EE'	75±39	3.0±0.80	1.1±0.32	1.4±0.28	11/61/25/1565	19
6-ECMBC	FF'	67±27	3.2±1.04	1.3±0.30	1.3± 0.36	10/45/21/574	7
TOTAL		63±25	2.8±0.84	1.0±0.23	1.27±0.27	10/65/23/9800	111

Moreover, relative locations of our five previous and one new (ECMB) clustered earthquakes in the Sea of Marmara are identified via HYPODD approach for the purpose of the identification of fault dipping angles and seismic zones (Waldhauser 2001). The HYPODD technique works with the double-difference algorithm from Waldhauser and Ellsworth (2000), and much more effective than regular individual or joint location methods. Although fault vertical angles are still not clear, important information is gained about the seismogenic zones via relative locations of clustered events. More details on the techniques of Horiuchi et al. (1995) and Waldhauser (2001) are presented in Korkusuz Öztürk and Meral Özel (2018).

3.3. Results and Discussion

Eastern Ganos Offshore Cluster (1-EGOC)

We derive relative locations of 85 earthquakes in the EGOC, as individual locations from the joint data set and orientations of principal stress axes are already obtained (Korkusuz Öztürk et al., 2015). Differences in horizontal and vertical locations are negligible from the comparison of individual and relative locations of hypocenters of earthquakes in the EGOC (Fig. 3.4) Even though slight changes are visible in the FPSs after the relative location process, still reverse FPSs are dominantly presented in the west of the EGOC, oblique FPSs and a few thrust FPSs are shown in the northeast of the cluster, and dextral strike-slip and extensional fault characteristics are mainly represented at the south east of the cluster.

Figure 3.4. Fault perpendicular cross sections for individual (left) and relative (right) locations for the profile AA' (Fig. 3.3). The left figure is obtained via Hypocenter software, while the right one is derived through HYPODD relative location technique (Korkusuz Öztürk and Meral Özel, 2018).

In terms of individual relocations, events are deeper than 2 km depth, whether some of them are shallower in terms of relative locations.

16 well-located earthquakes are observed in the sedimentary Basin (Bayrakçı et al., 2013), and four of those events have minor strike-slip components. Namely, sedimentary Basin events are mostly normal and thrust, as it is expected. The seismically active zone extends to the 17 km depth. Moreover, although curvature like event alignments are observable in the NW of the cluster, it is not possible to identify deep angles of the complex multi segments. Furthermore, recent geodetic studies imply that the Ganos Onshore segment, which has lower seismicity, is locked up to 9±2 km or 14 km depth (Ergintav et al., 2014; Schmittbuhl et al., 2015, respectively).

Eastern Tekirdağ Basin Cluster (2-ETBC)

Double-difference locations of 75 earthquakes in the ETBC are obtained, as their individual relocations and stress tensor orientations are previously derived (Korkusuz Öztürk et al., 2015). The main earthquake activity of the region represents pure extension although some dextral strike-slip FPSs with some normal and thrust components also exist.
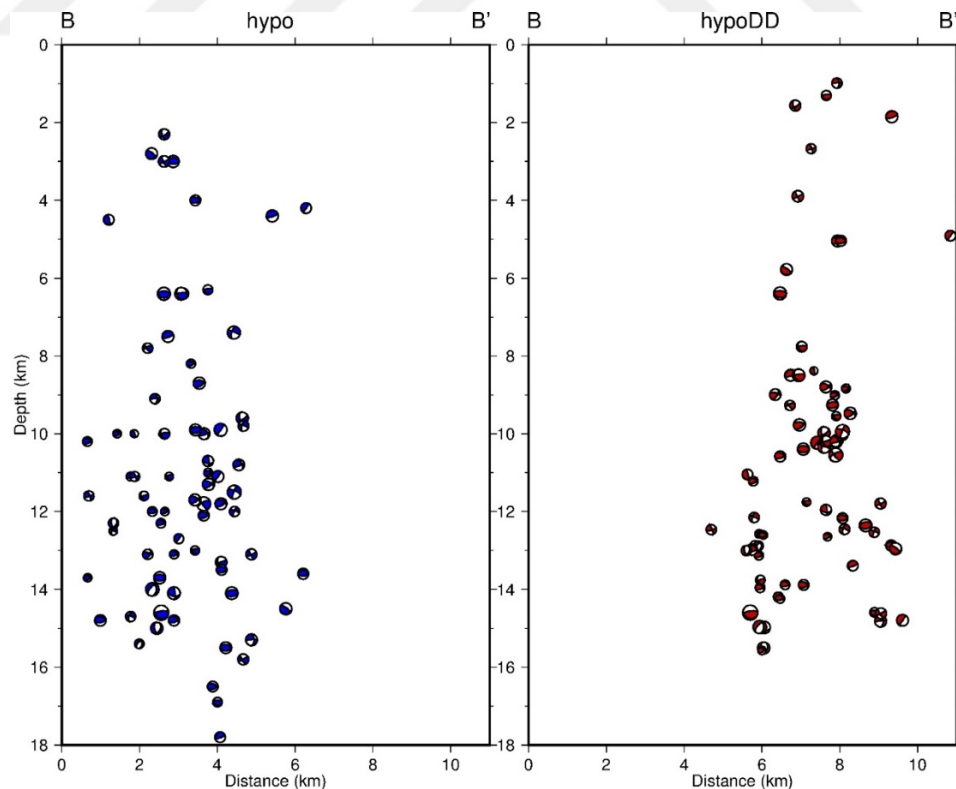
Figure 3.5. Fault perpendicular cross sections for individual (left) and relative (right) locations for the profile BB' (Fig. 3.3) (Korkusuz Öztürk and Meral Özel, 2018).

Epicentral locations of earthquakes are moved from south to north through the application of the HYPODD double difference technique (Fig. 3.3 and 3.5). As a result of this movement the fault segment seems to be compatible with the fault trace defined by Armijo et al. (2002). Besides, hypocenters of very shallow events move from 2 km to 1 km, and the main earthquake activity is shifted from 10-15.5 km to 8.5-15 km. Also, vertical alignment of the hypocenters of the earthquakes draw a line with around 84° dip angle from horizontal. Nevertheless, a study from an OBS data set presents that the micro-earthquake activity of this region is located between the 10-26 km depth interval (Yamamoto et al., 2017). Moreover, 4-8 mm/yr strain rate is found out via recent extensometers (Yamamoto et al., 2016). Therefore, the working area may be creeping ~10 km or less. Schmittbuhl et al. (2015) also attribute the region as a deep creep above ~15 km depth. Our double-difference relocations present that the main earthquake activity is deeper than 8.5 km, the creeping part of the segment should be shallower. Furthermore, the Eastern Tekirdağ Basin segment may not load stress, regarding the suggested creep, existence of ML3.5-4.5 events with a few month recurrence intervals and ML4.5-5.2 events with around one-year occurrence intervals since 2008, and hypocentral depths of some events shallower than 10 km (Korkusuz Öztürk et al., 2015; KOERI Catalogue).

Eastern Central Marmara Basin Cluster (6-ECMBC)

We re-identify P and S phase arrivals in the ECMB, and read P-wave first motion polarities for 53 earthquakes. The number of selected earthquakes decreases to 27 as a result of our criteria each event must have at least 10 high quality P-wave FMPs and maximum 1 misfit station. Next, events are relocated not only individually using HYPOCENTER software, but also relatively using HYPODD software, and their FPSs are obtained (Fig. 3.6 and Fig. 3.7). Additionally, alignments of principal stress axes are derived through individual locations of events (Fig. 3.8).

Locating at the center of the Marmara Sea, the analysis of this cluster has been a challenge until the deployment of the latest OBSs. On the other hand, we could investigate the ECMBC with 67˚ azimuthal gap in station coverage via our joint data set and extended time span.
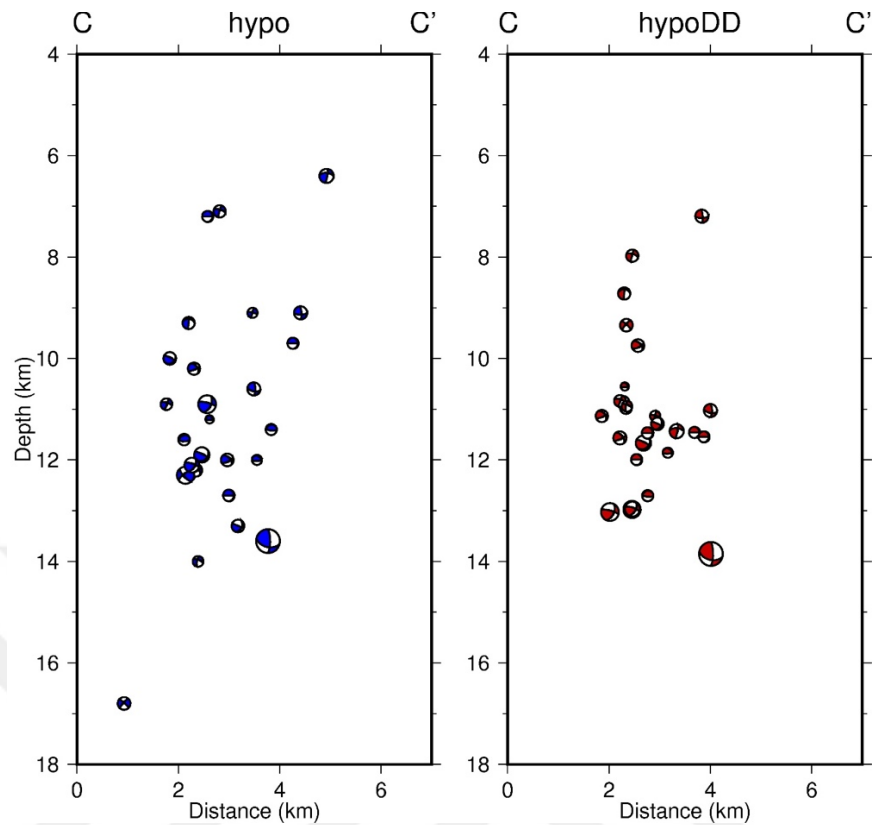
Figure 3.6. Fault perpendicular cross sections for individual (left) and relative (right) locations for the profile CC' (Fig.3.3) (Korkusuz Öztürk and Meral Özel, 2018).

The mean location errors are 1.3±0.3 km, 1.3±0.4 km, and 3.2±1.0 km in latitude, longitude, and depth, respectively (Table 3.1). The majority of FPSs in this cluster exhibit NE-SW oriented extension, even though some of the events have right lateral strike-slip components, as well (Fig. 3.7). Besides, a former study finds only pure right lateral strike-slip FPSs via the investigation of 13 earthquakes within the whole CMB (Örgülü, 2011). The calculated azimuth and plunge angles of the maximum, intermediate and minimum principal stress axes are; 90°/79°, 304°/3°, 214°/5°, respectively (Fig. 3.8 and Table 3.2).

Little horizontal and vertical alterations are visible in the hypocentral locations of earthquakes from the comparison of individual and relative locations, as their locations become closer as an outcome of the HYPODD approach (Fig. 3.6).
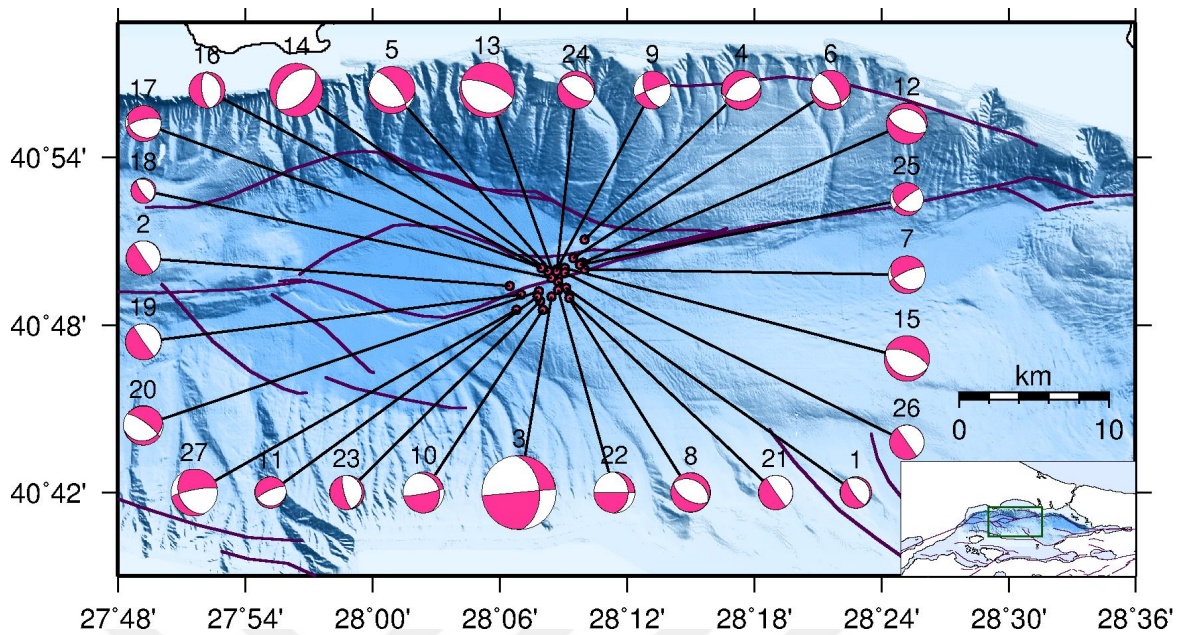
Figure 3.7. Focal mechanism solutions of 27 earthquakes in the Eastern Central Marmara Basin cluster, used for the calculations of principal stress axes orientations (Korkusuz Öztürk and Meral Özel, 2018).
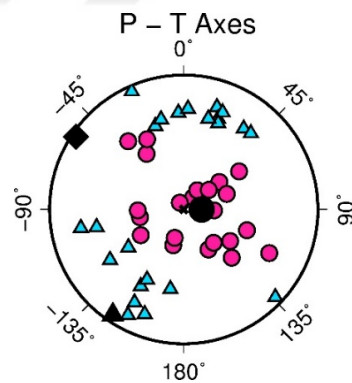
Figure 3.8. Simultaneously identified lower hemisphere projections of pressure (Pink circles) and tension (Turquoise triangles) axes (Korkusuz Öztürk and Meral Özel, 2018). The black dot, diamond and triangle are the maximum, intermediate and minimum principal compressive stress axes, respectively.

As an output of our vertical cross sections, hypocenters of earthquakes are condensed between the depth interval of 10.5 km and 14 km. In addition, the ECMBC has a few events above the 10.5 km depth, so this segment may be creeping at the upper part (Fig. 3.6), as it

is already attributed by recent investigations, as well (Klein et al., 2017; Schmittbuhl et al., 2015; Ergintav et al., 2014). Alternatively, no event is observed shallower than 7 km depth, so the upper part may be locked. Therefore, the only creeping part may be limited between the depths 7 km and 10.5 km. On the other hand, the silence of the upper part may be an outcome of the ~4 km sediment layer (Bayrakçı et al., 2013). Moreover, the 989 AD earthquake at the eastern section of the MMF and the 1343 event at the CMB segment have been the only earthquakes for last 2000 years (Şengör et al., 2005; Ambraseys,2002; Pondard et al., 2007). Also, recent strike-slip strain rates are ~2mm/yr and the slip deficit is smaller than 2 m (Ergintav et al., 2014). As a result of all these recent studies, the possibility of existence of aseismic creep in the Central Marmara Fault is high, and this segment may not be able to lead a large earthquake (Ergintav et al., 2014; Meade et al., 2002) although energy release may have occurred or not during the 1766 earthquake.

Eastern Çınarcık Basin Cluster (3-ECBC)

In the ECBC, double-difference locations of 73 earthquakes are derived through our previous results (Korkusuz Öztürk et al., 2015) from a joint data set, as it is done for other clusters, as well. The Basin is mainly considered as a dominant strike-slip motion (Örgülü, 2011; Pınar et al., 2003; Bulut et al., 2009), and even both strike-slip and reverse behaviors (Bohnhoff et al., 2012). The bifurcation of the ECB and the strain partitioning may even be denied considering the fault pattern defined by Zachariasen & Sieh (1995) (Pınar et al., 2003). Nevertheless, following works from individual (Polat et al., 2002) and composite (Sato et al., 2004) FPs, and our individual and relative locations of earthquakes in this cluster present extensional fault motions. Besides, latest GPS analyzes express 6±2 mm/yr extensional and 15±2mm/yr right-lateral offset (Ergintav et al., 2014). The 18 September 1963 M6.3 earthquake also, which is the last devastating event in the Northern Çınarcık Basin, has a WNW-ESE oriented extensional FPS (Başarır Baştürk et al., 2016; Taymaz et al., 1991). In addition to these right lateral strike-slip and normal fault motions, and 70° dip angle of the northern segment of the Basin, high stress states are investigated as an indicator of the Princes' Island segment at the north of the Basin via result of Coulomb models (e.g. Bohnhoff et al., 2013; Uçarkuş et al, 2011; Parsons, 2004; Hubert-Ferrari et al., 2000).
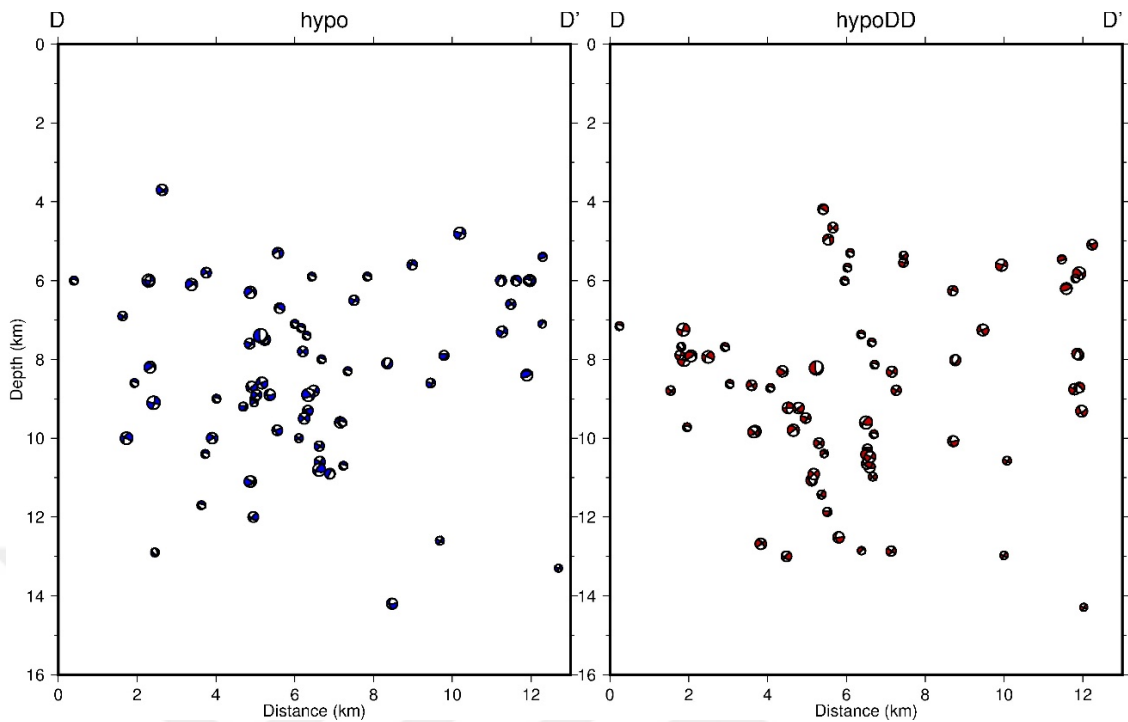
Figure 3.9. Fault perpendicular cross sections for individual (left) and relative (right) locations for the profile DD' (Fig.3.3) (Korkusuz Öztürk and Meral Özel, 2018).

Individual and relative locations do not exhibit important differences horizontally, while some fault traces become visible vertically when the HYPODD method is used (Fig. 3.9). Thus, a negative flower structure comes to exist with the double difference approach, especially at the south of the Basin, as it is also proposed previously (Beyhan and Selim, 2007; Aksu et al., 2000). This feature seems to be compatible with bathymetry data of the Eastern Çınarcık Basin. Besides, it should be noted that the north of the Basin is steep, while the negative flower structure is to the south. In other respects, the northern segment of the Basin is not very precise as it has around 70° dip angle (Oglesby and Mai, 2012). Hence, the normal component of the ECB should not be passed. The sedimentary Basin of the ECB alters between 1.5 and 3 km depths (Bayrakçı et al., 2013).

Furthermore, the seismogenic zone is shown much clearly via the relative relocation technique. The seismic activity is focused at the 8-13 km depth interval at the south, whether it is condensed at the 5-13 km depth interval at the north of the Basin (Fig. 3.9). Therefore, our findings from the analysis of the 30 km eastern section of the Çınarcık Basin, reveal that the northern segment of the Çınarcık Basin (The Princes' Island Fault) is locked above ~7

km depth, even though it is previously attributed to be locked above 10 km depth (Klein et al., 2017; Schmittbuhl et al., 2015; Ergintav et al., 2014, Bohnhoff e al., 2013). This variation may originate that we use a dense network and have the chance of analysis with very small error amounts or we analyze only the east of the Basin due to the small number of events in the western section.

Yalova Cluster (4-YC)

We derive relative locations of 102 earthquakes in the Yalova region. The dominant earthquake source mechanisms from the aftershocks of the 1999 İzmit event, which has a pure right-lateral strike slip FPSs, have mostly normal faulting mechanisms (Pınar et al., 2009; Bohnhoff et al., 2006; Pınar et al., 2003; Karabulut et al., 2002; Özalaybey et al., 2002). Our HYPODD relocations also present extensional and oblique FPSs which are compatible with recent studies based on individual (Korkusuz Öztürk et al., 2015, Karabulut et al., 2011; Örgülü 2011) and composite source mechanisms (Bulut et al., 2009; Sato et al., 2004).
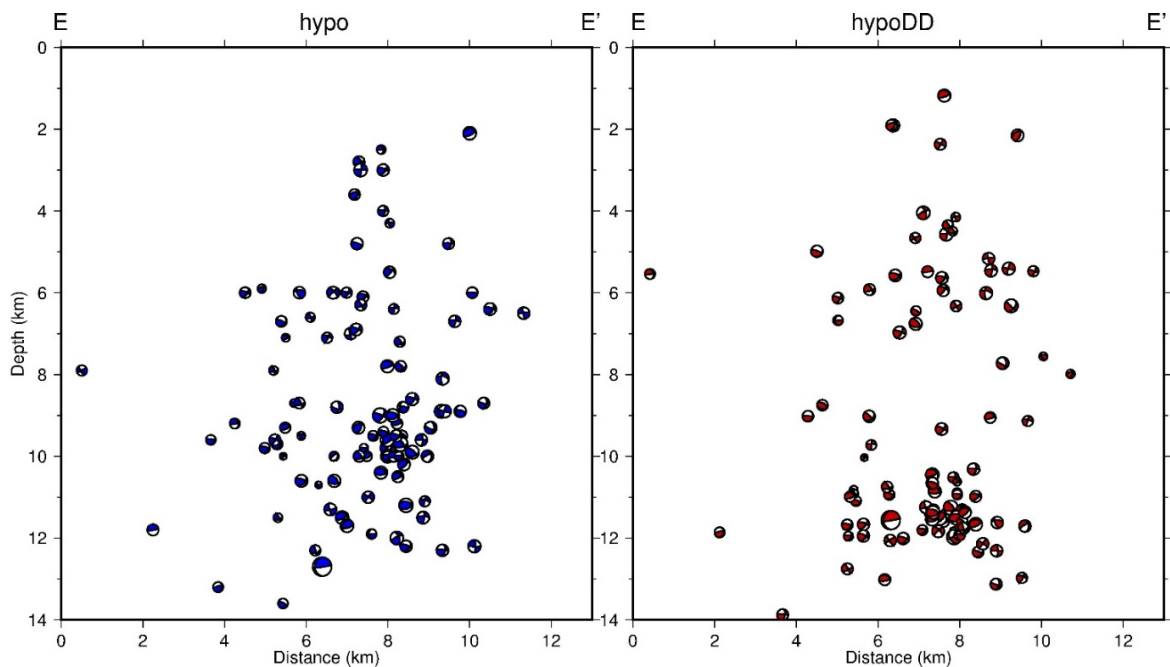
Figure 3.10. Fault perpendicular cross sections for individual (left) and relative (right) locations for the profile EE' (Fig.3.3) (Korkusuz Öztürk and Meral Özel, 2018).

Through the relative relocation process, we observe very little shift in the horizontal alignments of the hypocenters, and relatively high amount of vertical shift in the vertical alignments (Fig. 3.10). Furthermore, some previous studies of aftershock activity of the 1999 İzmit Earthquake obtain that Yalova region events are shallower than 5 km depth (Pınar et al., 2009; Pınar et al., 2003; 2001), and some others find that the seismogenic zone is between 12.5 km or 3-14 km depth intervals (Ito et al., 2002; Özalaybey et al., 2002, respectively). On the other side, we observe that the seismically active zone of the cluster situates between ~2 km and 14 km depth interval. On the other hand, it should be noted that the dense earthquake activity between the 10 km and 12.5 km depth interval may be the outcome of the 12 March 2008 ML4.6 main shock (Korkusuz Öztürk et al., 2015). Moreover, we reveal a new silent zone between the depths 7 km and 9 km stem from the alignments of the HYPODD relocations.

Gemlik Cluster (5-GC)

Relative locations of 63 events, some of which are aftershocks of the 24 October 2006 ML5.2 earthquake, located in the Gemlik region. Earthquakes in the Gemlik gulf mainly have normal FPSs, and the ones in the Gemlik onshore have right lateral strike-slip and oblique FPSs.
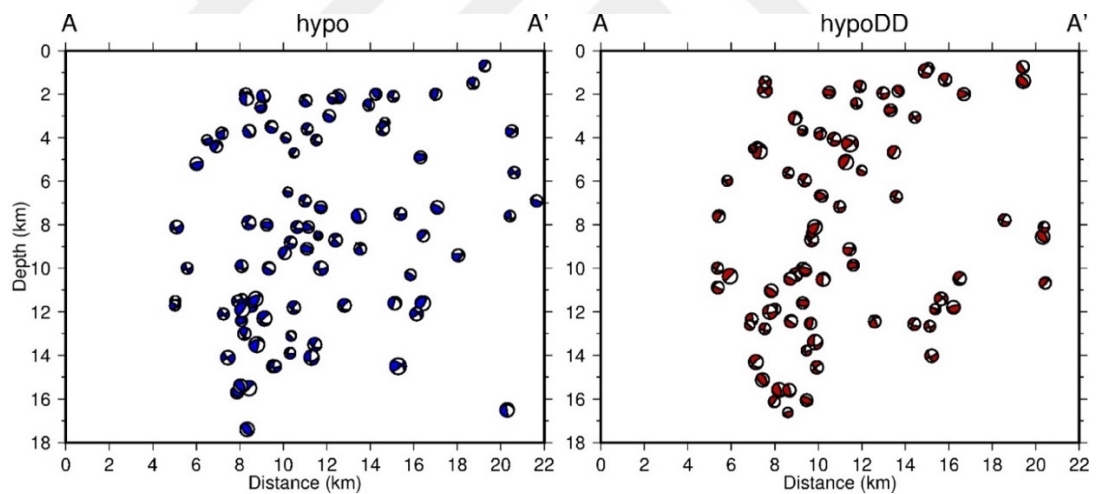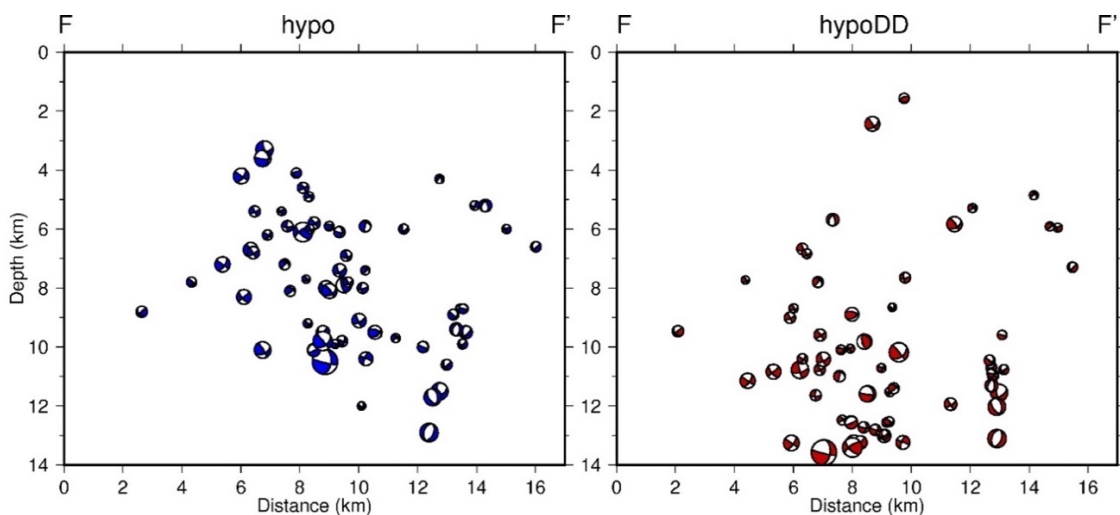

Figure 3.11. Fault perpendicular cross sections for individual (left) and relative (right) locations for the profile FF' (Fig.3.3) (Korkusuz Öztürk and Meral Özel, 2018).

As a result of comparison of individual and relative locations, very little shift is observed horizontally, while deepening is visible vertically (Fig. 3.11). In addition, strings, consisted by 6-10 earthquakes, might be representatives of different branches of the main fault segment which passes from the Gemlik Gulf. Also, the seismogenic zone is located between the depths of ~5 and ~13 km.

3.4. Conclusion

We complement our previous study which derive stress tensors from the data from 2006 to 2011 (Korkusuz Öztürk et al., 2015). We expand the time interval from 2006 to 2014 for the ECMBC owing to the lack of seismicity. A joint data set is used via the seismic stations from KOERI, TUBITAK and AFAD. P and S phases are re-identified, and P wave first motion polarities are also read for 53 ML$\geq$1.5 earthquakes. As a result of selection of well-defined hypocentral locations and fault plane solutions, the number of earthquakes decreased to 27.

A NE-SW oriented extensional stress state is obtained from the orientations of SHmax axes, while a few oblique FPSs also exist with right-lateral components.

Relative locations are defined by HYPODD software for the six most visible earthquake clusters, EGOC, ETBC, ECMB, ECB, YC, GC. Because earthquakes within the clusters are not further than 2 km hypocentral distance, numbers of earthquakes do not decrease and hypocenters of earthquakes do not change significantly when relative locations are derived. Since we use data from 105 three-component stations, important knowledge on the depth of the seismic zones are obtained.
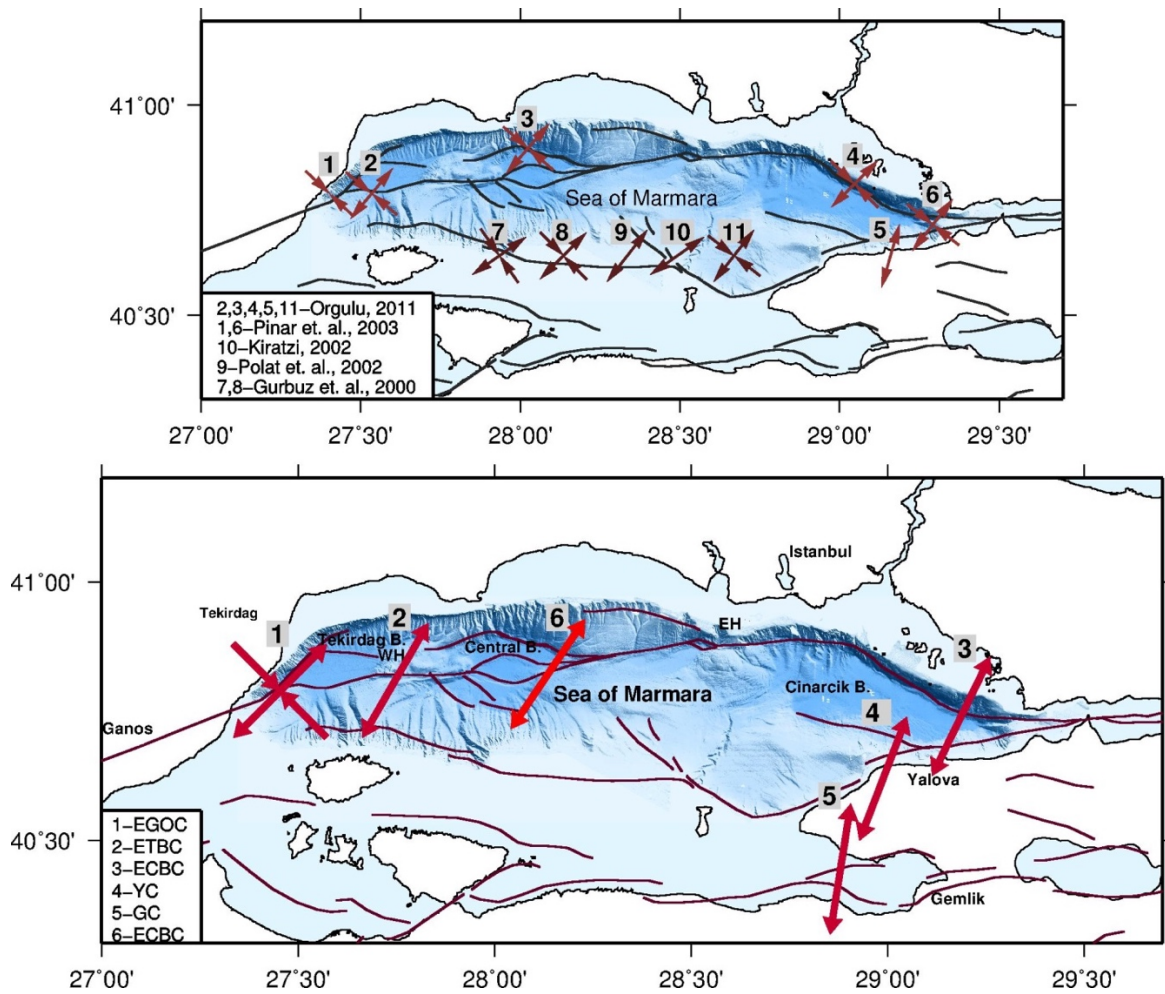
Figure 3.12. The map of alignments of the maximum horizontal stress axes from previous studies (the top figure); 2, 3, 4, 5 (light brown) for local analyzes in the Marmara Sea; 1 and 6 (light brown) for the western and the eastern Marmara regions; and 7, 8, 9, 10, 11 (dark brown) for the whole Marmara Region (Gürbüz et al., 2000; Kiratzi, 2002; Polat et al., 2002; Pınar et al., 2003; Örgülü, 2011). The below map is for the recent stress states in the Sea of Marmara five of them are derived by Korkusuz Öztürk et al. (2015) and one of them (6, light red) is obtained during this thesis study (Korkusuz Öztürk and Meral Özel, 2018). Orientations of horizontal stress axes for the Eastern Ganos offshore (1), Eastern Tekirdağ Basin (2), Eastern Çınarcık Basin (3), Yalova (4), Gemlik (5) and Eastern Central Marmara Basin (6) clusters.

Table 3.2. Stress tensor inversion results. The second column shows the amount of selected and total earthquakes recorded in the cluster. Third, fourth and fifth columns present azimuth and plunge angles of σ_1, σ_2 and σ_3 axes, respectively.

Cluster	Used/All Events	σ_1 Az-Pl	σ_2 Az-Pl	σ_3 Az-Pl
1-EGOC	85/144	315-35	141-50	221-7
2-ETBC	75/105	293-70	143-30	30-0
3-ECBC	73/116	123-80	298-10	206-5
4-YC	102/124	285-75	115-7	201-2
5-GC	63/100	102-58	285-30	189-5
6-ECMBC	27/53	90-79	304-3	214-5

The Eastern Ganos Offshore Cluster (EGOC), dominating a dextral stress structure, drives a seismic zone up to ~17 km depth, while the number of events within the sedimentary Basin (top 2 km depth) is significantly low. The Eastern Tekirdağ Basin Cluster (ETBC), having a NE-SW extensional structure, may have a creeping section above ~10 km depth. Also, this segment generates moderate size events within a few months or a year intervals during last years. As a result, this segment may load high stresses to create large events. The Eastern Central Marmara Basin Cluster (ECMBC) present an extensional state of stress, and the shallow part of the Basin may be creeping up to ~10.5 km depth, or totally locked up to ~7 km depth and creeping between ~7-10.5 km depth interval. The zone between ~10.5 and 14 km is already seismically active. The Eastern Çınarcık Basin Cluster (ECBC), which dominates an extensional regime, may be locked above ~7 km or ~10 km depths, so this segment may be capable of creating large earthquakes. The Yalova Cluster (YC), where many normal faulting earthquakes are found, is seismically very active area up to ~14 km depth. Nevertheless, a 2-km silent zone is observed between the ~7-9 km depth interval. Also, the shallow (<6.0 km depth) event activity may originates from the hot springs of the region. The Gemlik Cluster (GC), where onshore events have right lateral strike-slip characteristics, while offshore events mainly represent normal and oblique structures with right lateral components, has a seismogenic zone between ~5-13 km depths.

4. DYNAMIC EARTHQUAKE RUPTURE SIMULATION STUDIES BASED ON BIEM

The boundary integral equation method (BIEM) is a numerical computational method that is mostly used for proving the existence of solutions or the construction of solutions to linear partial differential equations (Costabel, M., wikipedia). It can be implemented to the problems for which Green's functions can be calculated. Nonlinearities can be included in the formulation even though they mostly lead use of volume integrals which requires discretization.

BIEM is the most efficient and accurate method in seismology compared to the other numerical approaches such as finite element method (FEM) and finite difference method (FDM), particularly when a homogeneous medium is under the consideration (Kame, N., and Kusakabe, T., 2012, Wikipedia). Hence, it is widely used in dynamic rupture simulations especially on non-planar faults. Even though BIEM has been first developed for the investigation of earthquake rupture in unbounded homogeneous media, it is currently used in homogeneous half-space models, as well (Kame, N., and Kusakabe, T., 2012). Medium inhomogeneity also can be introduced as it can be also considered in FEM and FDM.

In the first step of this method, computations are done only on the crack boundaries, so the geometrical complexities can be adapted by discretization of the surface into small finite elements. Because the crack extension is defined by placing new boundary elements at the crack tips, it is possible to define special crack patches in a mesh-free behavior (Kame, N., and Kusakabe, T., 2012).

Next, the elasto-dynamic equation of motion is directly solved for the defined boundary conditions via theoretical Green's functions. In the case of an earthquake rupture is under the consideration, a friction law also can be fussily adapted to the equation.

4.1. The 2D Boundary Integral Equation Method

4.1.1. The Methodology

In this part of the study, results of a 2D dynamic earthquake rupture simulation code that is developed in a C programming language are presented. Boundary Integral Equation Method (BIEM) is used for the stress and slip-rate calculations. The method of Cochard and Madariaga (1994) is identically adapted except from using large number of small grids due to the limitations on computation. A laptop with a 16 GB memory is used during this study. The aim is to achieve a better understanding for the effects of rupture parameters on the dynamic rupture simulations and the behavior of boundary integral equations. In addition, improvement in C programming language is one of the benefits.

In order to obtain the most realistic dynamic earthquake rupture simulations, the friction law is the most important aspect, considering the analysis of a more realistic earthquake model in terms of elastodynamics of the rupture propagation. In most of the studies, a constant kinematic friction or a slip-weakening friction law is used. According to some experimental results (e.g., Dieterich, 1972; Rice and Ruina, 1983; Gu et al., 1984), friction includes a set of unknown thermodynamic parameters related to the condition of the fault during an earthquake and it is a function of slip velocity which is nonlinear. In this study, an initial stress heterogeneity is defined as a realistic model coming from the simplified rate-dependent friction law (Carlson and Langer, 1989) (Fig. 4.2, eq. 4.17).
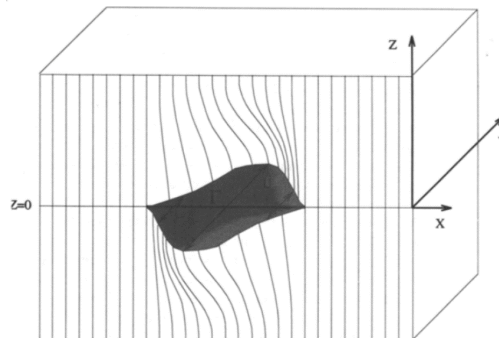
Figure 4.1. The geometry of the anti-plane shear crack. The fault area is on the z = 0 plane. The system is invariant with respect to translation along the Y axis.

In this study, an elastodynamic field caused by a flat antiplane crack $\boldsymbol{\Gamma}$ is used. It extends along the Z=0 axis within a homogeneous linearly elastic medium. β is the S-wave velocity. Opening of the fault is not allowed, and the crack can expand along the X axis. Slip and slip discontinuity are only possible in the direction of "y axis" (Fig. 4.1). Hence, σ_{yx} and σ_{yz} are the only nonzero elements in the stress tensor.
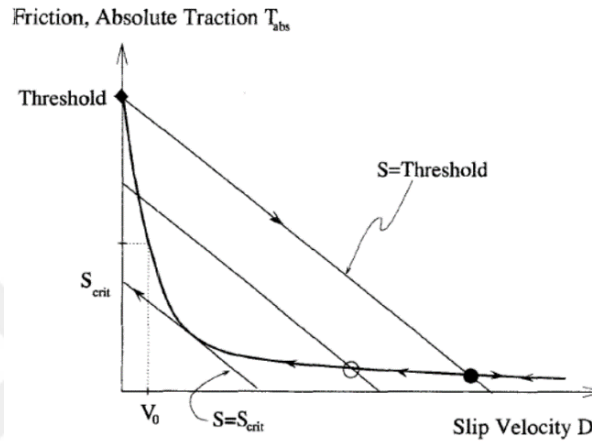
Figure 4.2. Slip velocity weakening friction law and the mechanism of instability for one sub-fault of the crack line (Cochard and Madariaga, 1994).

The equation of motion that represents the slip by $U_y(x,z,t) = U$ where v is velocity, x and z are space parameters and t is for time,

$$\frac{1}{v^2}\frac{\partial^2 u}{\partial t^2} = \nabla^2 u \tag{4.1}$$

Boundary conditions on the fault surface are given below:

$$\sigma_{yz}(x,t) = -T(x,t) \; on \; \Gamma$$
$$\Delta u(x,t) = 0 \; on \; the \; complement \; of \; \Gamma \tag{4.2}$$

Traction change (T(x,t)) is defined by a minus sign, since the Z axis is normal to the upper half space (Fig. 4.1). Also, infinite radiation conditions are assumed. Because the effect of friction is important to observe, the calculation of absolute traction (Tabs), which is the function of slip-rate, is needed. Therefore, the nonlinear boundary value problem can

be solved by numerical methods. In order to solve eq. (4.1) for eq. (4.2), Cochard & Madariaga (1994) seek solutions using the boundary integral equation method (BIEM). Starting with the classical form of the Betti's representation theorem:

$$u(x, z, t) = \int_r \int_0^t \Delta u(\xi, \tau) \Sigma(x, z, \xi, t - \tau) d\tau d\xi \qquad (4.3)$$

Where Σ, the z derivative of the 2D Green Function (eq. 4.4), is the *yz* component of the stress tensor.

$$G(x, z, \xi, t) = \frac{1}{2\pi\mu} \frac{H(t - \frac{r}{v})}{\sqrt{t^2 - r^2/v^2}} \qquad (4.4)$$

$$r = \sqrt{(x - \xi)^2 + z^2}$$

H(t) is the Heaviside function, so the condition $z \to 0$ reduces to an identity (eq. 4.3). Therefore, the change in stress field σ_{yz} caused by slip Δu is calculated by;

$$T(x, t) = -\int_r \int_0^t \Delta u(\xi, \tau) \mu^2 \frac{\partial^2}{\partial z^2} G(x, 0, \xi, t - \tau) d\tau d\xi \qquad (4.5)$$

$$T(x, t) = -\frac{\mu}{2\pi v^2} \int_r \int_0^{t_m} \Delta u(\xi, \tau) / [(t - \tau)^2 - (x - \xi)^2/v^2]^{3/2} d\tau d\xi \qquad (4.6)$$

On the other hand, the equation (4.6) is hyper-singular near the source point, when $\xi \to x$ and $\tau \to t$. As a result, with the assumption that Δu and its derivative with respect to *x* are continuous, they transform eq. (4.6) into eq.(4.7) by using the method of Koller et al. (1992):

$$T(x, t) = -\frac{\mu}{2\pi} \int_r \int_0^{t_m} \left[\frac{t - \tau}{x - \xi} \frac{\partial}{\partial \xi} \Delta \dot{u}(\xi, \tau) + \frac{1}{v^2} \frac{\partial}{\partial \tau} \Delta \dot{u}(\xi, \tau) G(t - \tau; x - \xi) d\tau d\xi \right] \qquad (4.7)$$

$$G(t - \tau; x - \xi) = ((t - \tau)^2 - \frac{(x - \xi)^2}{v^2})^{-1/2}, \tau_m = max \ (0, t - \|x - \xi\|/v)$$

The equation (4.7) is regular everywhere except for the source, but it is not symmetric. Burger's vector is used to represent the first term of the integral equation. The second term includes the instantaneous response of the crack both to a stress change and to laterally

heterogeneous slip functions. Therefore, Cochard and Madariaga (1994) use double Laplace transforms for space and time, and get the following equation that gives Heaviside like slip velocity due to an instantaneous traction change:

$$T(x,t) = -\frac{\mu}{2v}\Delta\dot{u}(x,t) - \frac{\mu}{2\pi}\int_r\int_0^{t_m}\frac{\sqrt{(t-\tau)^2-\frac{(x-\xi)^2}{v^2}}}{(t-\tau)(x-\xi)}\frac{\partial}{\partial\xi}\Delta\dot{u}(\xi,\tau)d\tau d\xi \tag{4.8}$$

The integral equation (4.8) is regular everywhere except for the source ($\xi \rightarrow x$) which is related to the static field of a dislocation. The second term includes not only long-range elastic interactions but also wave interactions because of wave front singularities.

The discretized slip-velocity field is given by equation (4.9), and the kernel of it defined as a simple box-car function as given in equations (4.10) and (4.11). Tabs is the absolute traction, $D_{j,m}$ is slip-rate and $H(.)$ is the Heaviside function.

$$\Delta\dot{u}(x,t) = \sum_{j,m}D_{j,m}d(x,t;x_j,t_m) \tag{4.9}$$

$d(x,t;xj,tm)$ is a simple box car function in the following form;

$$d(x,t;x_j,t_m) = 1 \ \ if \ \ x_j \le x \le x_{j+1} \ \ \ and \ \ \ t_m \le t_m \le t \le t_{m+1}$$
$$d(x,t;x_j,t_m) = 0 \ \ \ \text{otherwise.} \tag{4.10}$$

And d can be written as;

$$d(x,t;x_j,t_m) = H(x-x_j)H(t-t_m) - H(x-x_{j+1})H(t-t_m) - H(x-x_j)H(t-t_{m+1}) + H(x-x_{j+1})H(t-t_{m+1}) \tag{4.11}$$

$$T(x,t) = -\frac{\mu}{2v}\sum_{j,m}D_{j,m}K(x,t; \ x_j,t_m) \tag{4.12}$$

Stress Kernels (Green's functions) are calculated from the equation (4.13) that represents space and time shift terms.

$$K\left(x,t;x_j,t_m\right) = I\left(x - x_j, t - t_m\right) - I\left(x - x_{j+1}, t - t_m\right) - I\left(x - x_j, t - t_{m+1}\right) + I\left(x - x_{j+1}, t - t_{m+1}\right) \tag{4.13}$$

$$I(x,t) = H(t)H(x) + \frac{1}{\pi} H(t - \|x\|/v) \left[\frac{\sqrt{1-(x/vt)^2}}{x/(vt)} - sin^{-1}\left(\sqrt{1 - \left(\frac{x}{vt}\right)^2}\right) sign(x) \right] \tag{4.14}$$

The target equations to be solved for stress and slip-rate are as following:

$$T_{abs_{i,n}} = -\frac{\mu}{2v} D_{i,n} + T_{0_i} - \frac{\mu}{2v} \sum_{m=0}^{n-1} \sum_j D_{j,m} K_{i-j,n-m} \tag{4.15}$$

$$D_{i,n} = -\frac{2v}{\mu} \left[T_{abs_{i,n}} - T_{0_i} \right] - \sum_{m=0}^{n-1} \sum_j D_{j,m} K_{i-j,n-m} \tag{4.16}$$

Positive signs in equation (4.16) are converted into minus signs in our study in order to get accurate solutions. Furthermore, in the following equation (friction law) V_0 is the rupture velocity that depends on the shear wave velocity by a rate-dependence constant V_0. T_{thres} is the threshold for the traction and has the same value along the fault geometry. It should be noted that the rate-dependent friction law (eq. 4.17) is unstable for low values of slip-rate although friction decreases to a finite limit for large slip velocities.

$$T_{abs_{i,n}}\left(D_{i,n}\right) = T_{thres_i} \frac{V_0}{V_0 + D_{i,n}} \tag{4.17}$$

The rupture criterion is given by eq (4.18). For an element i which was locked at time '$n – 1$', we decide that it is going to slip at time n if its absolute traction is equal or greater than the threshold. The dimensionless rupture threshold is taken as 2.5 as it is normalized by $2/\mu$.

$$T_{0_i} - \frac{\mu}{2v} \sum_{m=0}^{n-1} \sum_j D_{j,m} K_{i-j,n-m} \geq T_{thres_i} \tag{4.18}$$

Our stress kernel is in the form below:

$$K_{i-j,n-m} = K(x_i - x_j + \varepsilon_x \Delta x, t_n - t_m + \varepsilon_t \Delta t) \tag{4.19}$$

xi and tn are for space and time at the observation point, and xj and tm are for space and time at the source point, respectively. Coordinates for the collocation points are defines by, $x = xi + ex*\Delta x$ and $t = tn + et*\Delta t$ as a result of the discretization.

Space coordinates are shown in the below figure as dx is the grid size. Red dots indicate locations of collocation points. Similarly, *dt* is the time step between *t(n+1) – tn*.
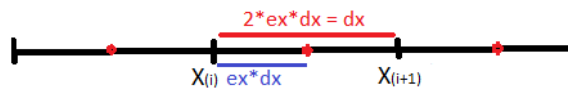
Figure 4.3. Spatial discretization.

ex = 0.5 and *et = 1.0* as they are already suggested by the paper. $\Delta x = 0.05$ and $\Delta t = 0.025$ are selected for the computational easiness, concerning the CFL (Courant–Friedrichs–Lewy) stability Condition *"v . Δt / Δx = C = ½"*. Dimensionless values of rigidity and shear wave velocity are selected as "$\mu = 1.0$" and "$v = 1.0$". Normalizations for stress, velocity, space and time are done as following:

$$T'_{abs} = \frac{2T_{abs}}{\mu}, \qquad D' = \frac{D}{v}, \quad x' = \frac{x}{\Delta x}, \qquad t' = \frac{tv}{\Delta x} \qquad (4.20)$$

Tabs is absolute traction, μ is rigidity, D is slip-rate, x is distance, Δx is grid length (sub-fault size), t is time and v is shear wave velocity. Therefore, stress is normalized by rigidity, slip-rate is by shear wave velocity, distance is by unit grid size and time is by the required time for a shear wave to cross a sub-fault distance.

In this study, two types of stress heterogeneities are used for the fault (Fig. 4.5). In both models, the fault is divided into 100 sub-faults (elements) and stress kernels are calculated. Next, 31 elements ($-15 \leq x \leq 15$) are locked at time n<0 at the rupture threshold (dimensionless 2.5) while stress is zero at other elements. For the twin asperity model, the first asperity ($-25 \leq x \leq 5$) is at rupture threshold by 31 elements (the same with the single asperity model) and the second asperity ($15 \leq x \leq 25$) is ready to break by 11 elements with an initial stress of 2.49 (selected value). The number of elements between the two asperities

is 9. After the definition of the fault geometry, the numerical computation starts. First, using the defined traction (Tabs) and slip information for n<0, slip-rate (eq. 4.16) and Tabs (eq. 4.15) are calculated simultaneously for n=0.
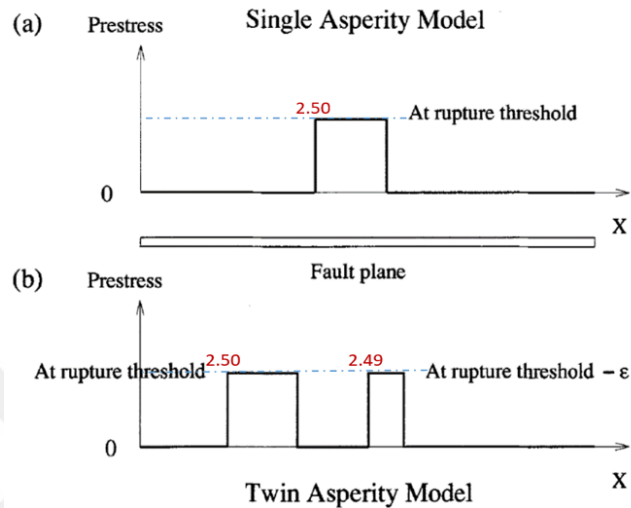
Figure 4.4. Initial stress states for the numerical simulations which are given in the paper. (a) One asperity model. (b) Two asperity model. The stress is zero outside of the asperities Cochard and Madariaga, 1994).

Consequently, using outputs from the summations of stress kernels for n>0, and stress and slip-rate for n=0, slip-rate and absolute traction are calculated for "n>0" for broken and unbroken elements concurrently. The computation of discrete convolution of slip velocity at source and stress kernel (eq. 4.15 and 4.16) are done over space and time. During this procedure the rupture threshold criterion (eq. 4.18) is also taken into the account, as well.

Moreover, when equation (4.17) is inserted into the equation (4.16), the nonlinear equation for the slip-rate is obtained. These two equations are solved simultaneously. As it is a quadratic equation, we have two roots. The manual solution of the quadratic equation and root equations are derived manually. The largest real root is selected in order to define slip-rate. The reason is that we are interested in the smaller stress regarding the friction law (Fig. 4.2). Besides, imaginary roots are ignored that is because imaginary poles coming from the boundary integral equation are already removed by transformations. For the time axis, all imaginary roots are left to the outside of the boundaries for using one-sided Laplace

transforms for the t>0, and those coming from space, as it is symmetrical, are also moved to the negative x axis by using double Laplace transforms and Cagniard-de Hoop method.

Moreover, in the rate-dependent case infinitely strong boundaries (with a high rupture threshold value) are used for the outside of the fault geometry. In this model, rupture extends toward the barriers, then stopping phases are emitted and spread out backward to the center of the fault. As a result, the slip-velocity of a sub-fault decreases slowly till the stopping phases from the boundaries arrive, then it decreases to zero immediately.

4.1.2. Results and Discussion

Stress kernel results (Fig. 4.1.5) represent singularities at source and wave front as it is expected from the integral equation (4.8). When the distance between source and receiver goes to zero, we have a zero factor in the denominator of the integral equation. Being a Cauchy type of singularity, it is associated with the static field of a dislocation. On the other hand, the stress kernels are converging a value around 1.2 with the increase in time. Secondly, we have wave front singularities which cause not only long-range elastic interactions but also wave interactions. Considering the wave front condition $t^2 - (x/v)^2 = 0$ (eq. 4.4), when rupture propagate with the shear wave velocity, it is clear that for an increasing value of |x|, t will converge a larger value of itself as it is the reason for the observation of the triangular wave front shape in Fig. 4.5. Therefore, stress kernels are singular along this triangular wave front.
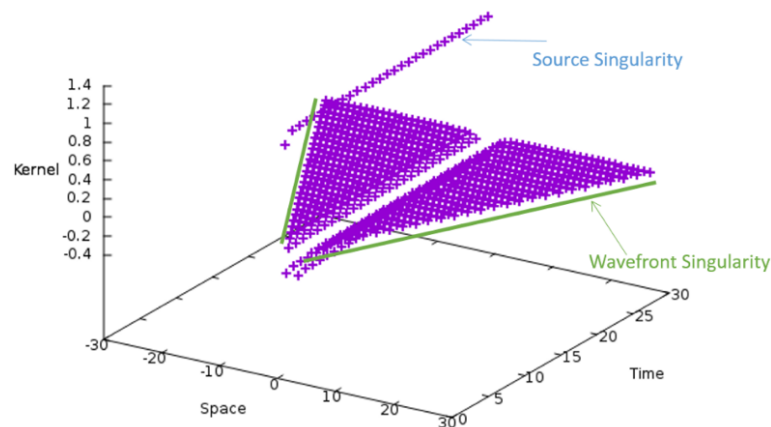
Figure 4.5. Stress kernels are shown by space and time dependently.

As it is also observed that amplitudes of stress kernels are decreasing with the time. Outputs of kernels are proved both quantitatively and qualitatively. It should be noted that each time grid represents 10 grids in our 3D plots, while each time and space grid represent 100 grids in Cochard and Madariaga's results. The reason for plotting less grids is that we have visualization problems as a result of the limited computational memory.

4.1.2.1. Rate-Independent Friction Law

When our slip velocity field findings are compared to the ones from Cochard and Madariaga for a rate-independent friction law (Fig. 4.6), in both results slip-rate at the asperity decreases first within a triangular shape and then it continues to decrease gradually. Since the total number of time steps could not be taken larger than 250 (due to computational restrictions), the termination of rupture is not observed. Besides, slip-velocity field from our code is not as smooth as the one from Cochard and Madariaga (1994) which may be caused by the stability conditions. Relatively large grid sizes (dx=0.05), sparse time steps (dt=0.025), and low number of grid and time steps are used due to computational restrictions.

Comparing absolute traction field from our study with the one from Cochard and Madariaga (1994), traction decreases to zero in both models, after the initiation of slip-rate (Fig. 4.6 and 4.7). Because the traction after the slip is fixed to zero and not enough number of time step is used in our model, the traction overshoot in the right figure is not visible in the left figure. Also, the stress emanates at the rupture edges after around the 400x10[th] time step in the right figure due to the reflections coming from the fault edges. That behavior is slightly visible in the left figure as well, even if it is not very clear because of using a coarser grid model.

Moreover, it is clear (Fig. 4.8) that the slip-rate at the asperity (initiation patch) decrease by the time as it is expected. Each line represents different dx and dt values as dt=dx=2 for v =1.0. Dt=0.6 (purple) and dt=0.3 (blue) lines exactly overlap, and Dt=0.1 (orange) line overlaps with 0.025 (yellow) line (namely, Dt=0.1 gives the same result for Dt smaller than 0.1, as well). The green line is for dx=1.0 and dt=0.5. Namely, for the dt higher than 0.5, we observe high amplitude zigzag shapes which most probably comes from not fine stability conditions.
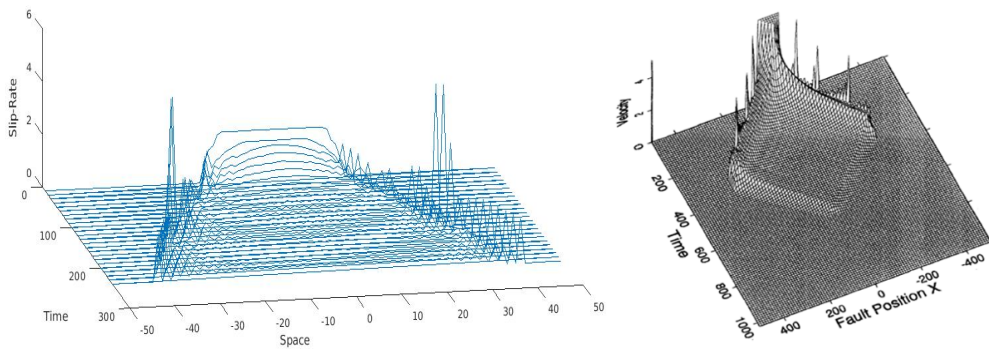
Figure 4.6. Slip velocity field for the single asperity model with a constant friction (rate dependency : $V_0 = 0$). Left figure is from our results while the right one is from Cochard and Madariaga (1994). Note: backwards slip-rate is prevented.
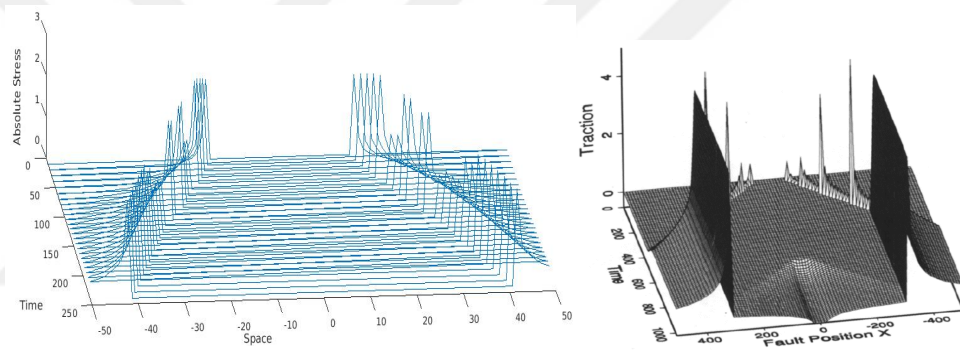
Figure 4.7. The stress field for the single asperity model with a constant friction (rate dependency : $V_0 = 0$).
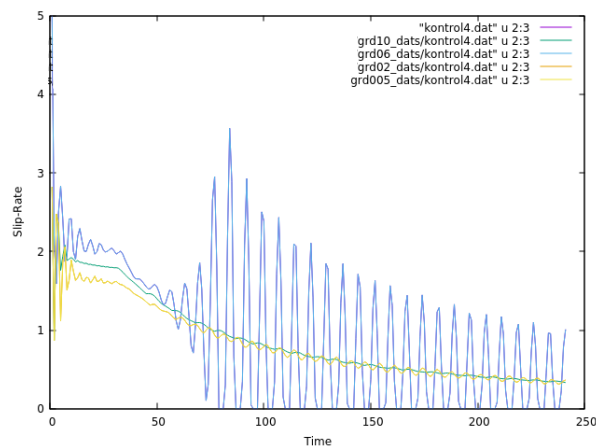
Figure 4.8. Time dependent slip-rate plot for an observation point located inside of the asperity. Dt=0.6 (purple (below blue line), dx=1.2), 0.5 (green, dx=1.0), 0.3 (blue, x=0.6), 0.1 (orange (below yellow line), dx=0.2) and 0.025 (yellow, dx=0.05) are used.

4.1.2.2 Rate-dependent Friction Law (vo=0.07)

For the rate-dependent case of single asperity model (Fig. 4.9), slip-rate at the initiation patch decreases in both figures by causing a triangular shape, and the rupture area is extending with time.
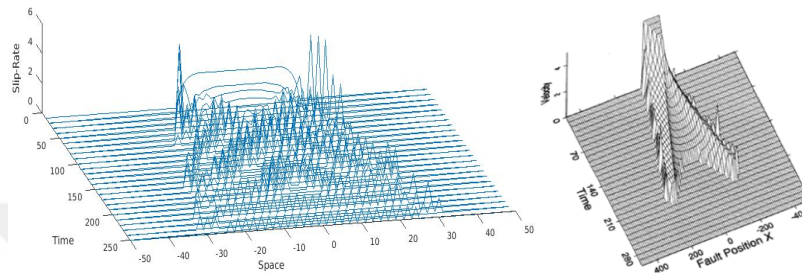
Figure 4.9. The slip velocity field for the single asperity model with a rate-dependent friction (rate dependency : $V_0 = 0.07$). The left figure is from our results while the right one is from Cochard and Madariaga (1994).
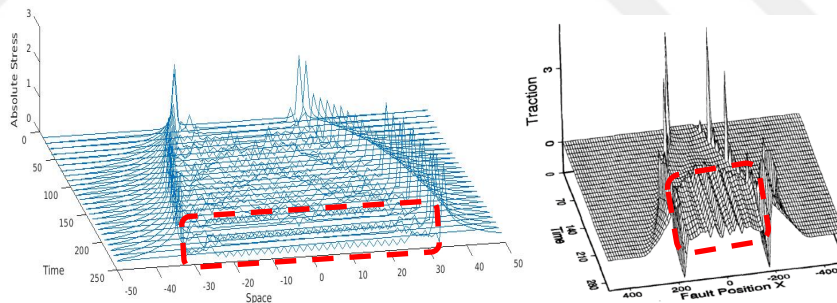
Figure 4.10. The stress field for the single asperity model.
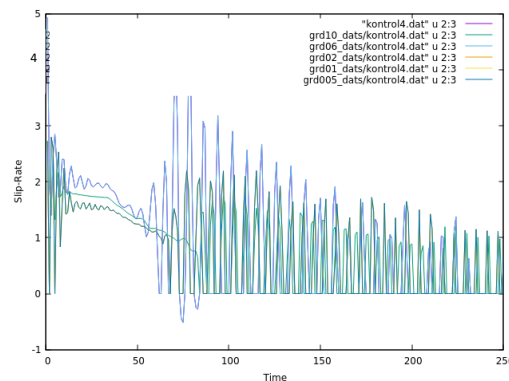
Figure 4.11. Slip-rate and time plot for an observation point located in the asperity.

Fig. 4.10 represents the compatibility of absolute traction results. Both models have some classical overshoot although it is not very clear in the above 3D plot. In addition, traction at the center of the fault increases as shown by zigzag shapes, since they receive information from the other broken elements.

Furthermore, the slip-rate at the asperity (initiation patch) decreases by time (Fig. 4.11). Zigzag shape is due to the sparse time step. The oscillation after the smooth part might be originating from the stability conditions as it is changing for different dt values. Being similar with the rate-independent case, dt=0.6 and dt=0.3 gives the same results, and dt=0.1 and dt<0.1 gives the same ones, as well.

4.1.2.3 Rate-dependent Friction Law (vo=0.045) with Two Asperities

For the twin asperity model (Fig. 4.12 and Fig. 4.13), the rupture is extending faster at the left side for both studies due to the existence of the second asperity. Also, because of the small number of time step in our model, it is not possible to compare termination of the rupture. Besides, the stress field for the twin asperity model of the reference study (Fig. 4.13) presents large over shoot because of inertia.

Moreover, 2D time dependent slip-rate plots (Fig. 4.14) for the both stress patches represent that slip started to occur at the second patch after a while. It is exactly what is expected. Also, for larger dt values we observe high slip-rate oscillation and so backward slip at the second asperity (purple-blue line at the bottom graph in Fig. 4.14).
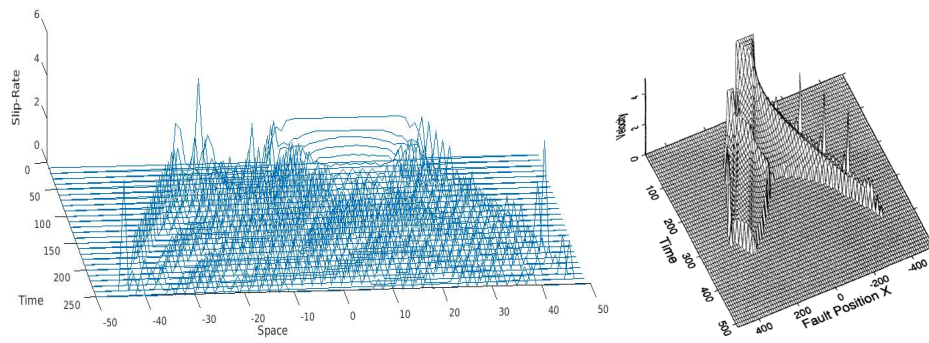
Figure 4.12. Slip velocity field for the twin asperity model with a rate-dependent friction (rate dependency : V_0 = 0.045). The left figure (the second asperity is on the right side) is from our results while the right (the second asperity is at the left) one is from Cochard and Madariaga (1994).
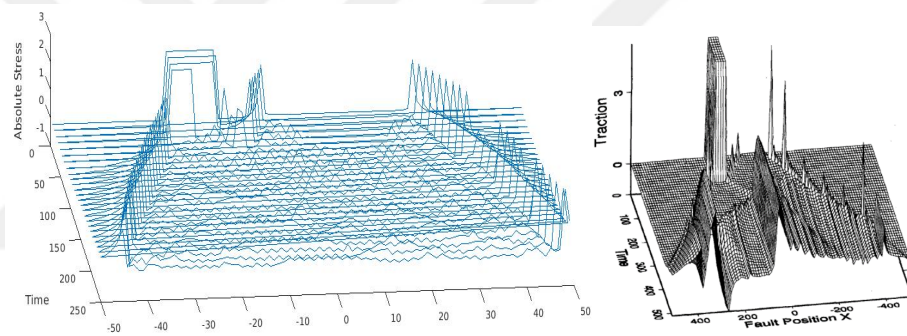
Figure 4.13. The stress field for the twin asperity model with a rate-dependent friction (rate dependency : V_0 = 0.045).
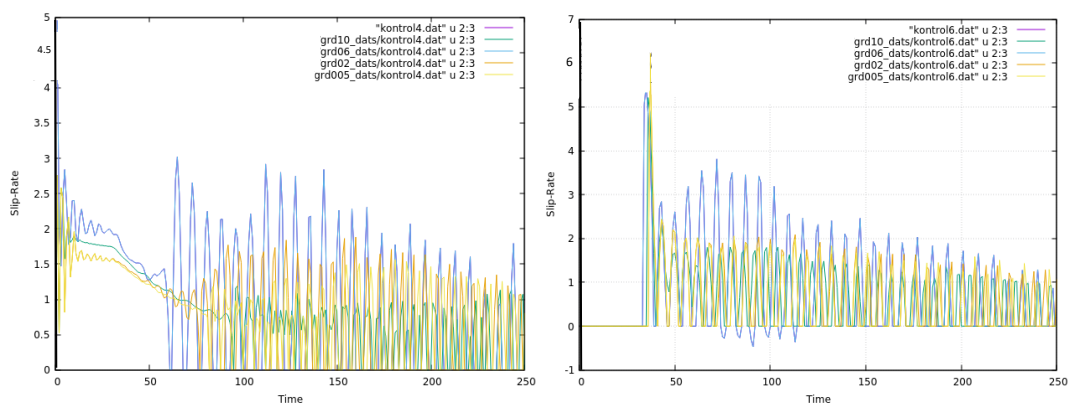
Figure 4.14. Slip-rate and time plot for an observation points located inside of the asperities. Left figure is for a point in the first asperity that breaks at time=0, while the right figure is for the second asperity that is ready to break.

4.1.3. Conclusion

Although some reliable findings are obtained, the stability conditions should be changed in a much sensitive way by changing the grid size and the time step in order to be able to compare our results with the findings of Cochard and Madariaga (1994) effectively. Besides, the total number of time steps should be increased in order to be able to observe the termination of the slip-rate.

Briefly, determinations of the grid size and the time step are very important in the dynamic earthquake rupture simulations, since it strongly affects the stability conditions. Especially the time step can lead dispersion. In addition, it may lead dynamic overshoots and change the termination of the rupture. The amplitude of the slip-rate also changes with the rate-dependency of the friction law. Even though the CFL stability criteria suggests C should be ≤ 1.0, usage of $C \leq 0.2$ gives the best results. Thus, the most convenient time step should be chosen for the best grid size, as well. Furthermore, the size of the initiation patch (asperity) is also significant, as it should be large enough, twice of the characteristic length, to generate a propagating rupture. The characteristic length is also related to the initial and final stress amounts (Details for 3D case are given in section 6).

4.2. Studies Based on a Boundary Integral Equation Method for 3D Dynamic Earthquake Rupture Simulations

Advantages of this Boundary Integral Equation Method (BIEM) code are; the required memory decreases from M^2N to M^2, and the calculation time decreases from MN^3 to MN^2. M is the total number of triangular elements and N is the number of time steps. Therefore, dynamic rupture simulations can be much applicable. Main equations and assumptions are seen in Fig. (4.16).
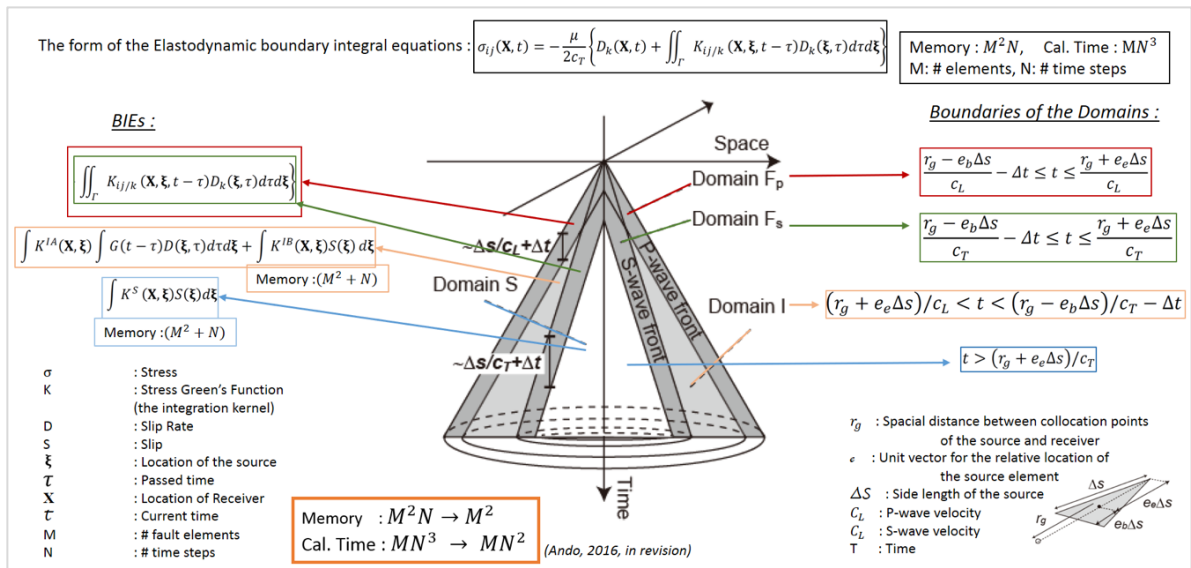
Figure 4.15. The definition of the Fast Domain Partitioning Method for BIEM.

The 3D dynamic earthquake rupture simulation code based on a new BIEM and C language is used (Ando, 2016). After reading the code line by line a user manual is prepared for this new Fast Domain Partitioning Method (FDPM) for BIEM.

Moreover, being under development, the FDPM code has needed verification. First, normalizations for stress, velocity, and displacement are done. Next, SCEC TPV5 code verification case is selected to apply this code and check our results with previously obtained global results from other techniques. Details about the model of the SCEC test case for a FEM case can be seen in the results section (Chapter 6).
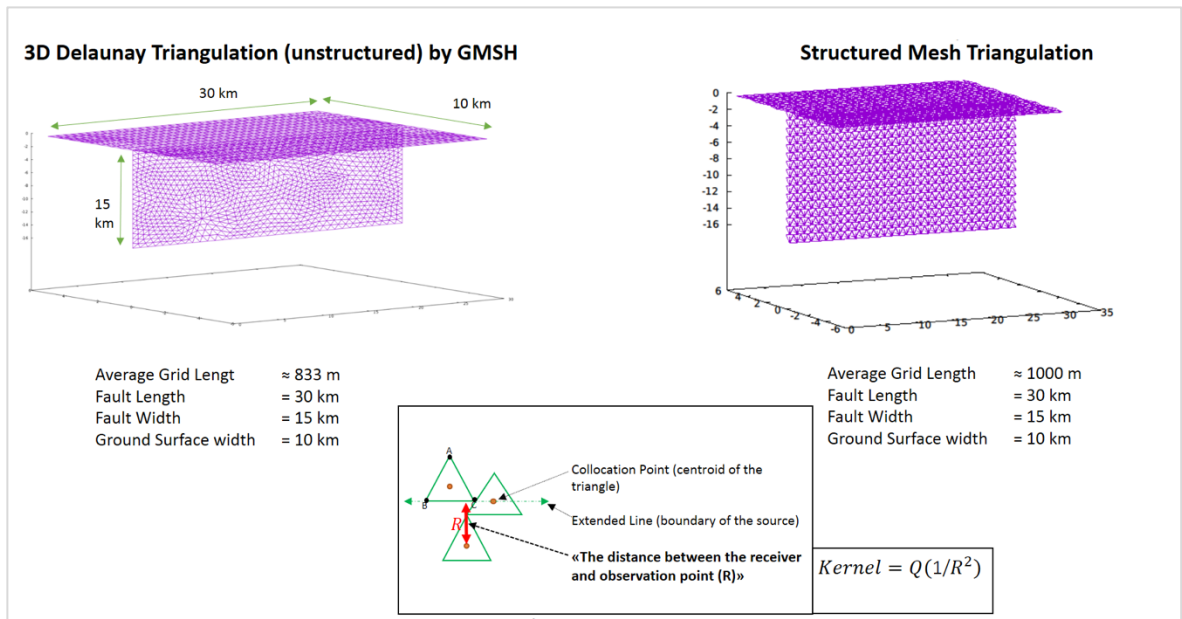
Figure 4.16. The fault geometry for SCEC TPV5 test case. Unstructured (left) and structured (right) meshes.
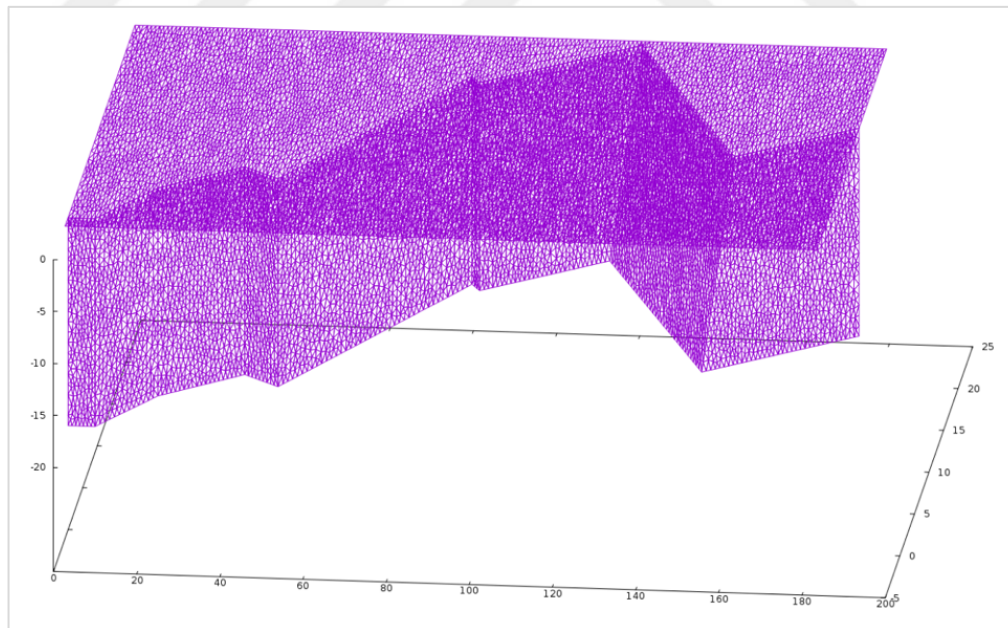
Figure 4.17. The fault geometry based on the model of Oglesby and Mai (2012), grid size is 1 km, the number of triangular elements is 21608, and required memory for the solution of the stress kernels is 4TB.

On the other hand, since stress, slip and slip-rate results of the code are not stable (e.g. stress is going to infinity) when rupture arrives to the ground surface. In order to achieve a solution to the stability problem, the inside of the simulation code is modified by myself to create its own planar geometry with a structured triangular mesh even though the unstructured mesh would be needed for our nonplanar geometry in any case. As a result, using a structured mesh has not solved the stability problem of the code, as well (Fig. 4.17).

Next, since unstructured meshing can lead zero value of the relative distance between sources and receivers (Fig.4.17), best shifting coefficients are determined to make three-dimensional small shifts (negligible size) when the distance is zero. Also, the best CFL condition (stability) parameters are derived from hundreds of runs.

On the other hand, none of our iterations could solve the stability problem even though a number of possible solutions are tried. Also, considering very high computational demand of the method although decreases in stress kernels achieved, application of this method becomes a challenge considering at least 5TB memory requirement for the analysis of the MMF. As a result, this method is not used for the MMF simulations.

3D fault geometry of Oglesby and Mai (2012) is generated for different grid sizes by writing scripts for GMSH program (Fig.4.18) in order to use in simulations for BIEM. A triangular mesh is selected to have a better smoothness at the segment boundaries. Hence, the barrier effect of a sharp geometry on the rupture propagation becomes minimum. The numbering order of apexes of each triangular element is counter-clockwise to be consistent with the BIEM Code (Ando, 2016) we use.

5. THE 3D DYNAMIC EARTHQUAKE RUPTURE SIMULATIONS BASED ON FEM

In order to achieve the main goal of this study, a standard finite element approach is used. In contrast to that BIEM matrixes are growing by the square of the number of the total time steps, the finite element matrices are growing linearly. Even though the computation time of the BIEM can be significantly decreased with the help of discretized Fast Fourier transforms, the FEM requires less computational demand. Therefore, considering the applicability of three dimensional, complex and large dynamic earthquake rupture simulations, PyLith code, based on the FEM is utilized (Aagaard, et al., 2017). The code is open source and user friendly with its detailed manual and support team. In addition, it is verified for most of the SCEC code validation test cases.

Since a forward modelling is processed for a fault constitutive model during the current study, the approach of physical and numerical parameters is very important. The TPV205 SCEC test case is selected to analyze in detail because it has heterogenous stress patches as we have in the Main Marmara Fault, as well. The only difference between the SCEC TPV205 and TPV5 cases is that the grid size increases gradually with increasing distance from the fault surface and ground surface in the former one. In addition, a fault model with two segments is created and the same simulations done to be experienced for the complex MMF. Although TPV5 have been analyzed for our BIEM based study (section 4.2), TPV205 is processed for our FEM based investigation. The reason is that, boundaries of the fault geometry can be identified by the definition of travel time equations of the P and S waves for the BIEM analyses, while boundaries of the fault geometry can't be adapted for FEM cases and the whole 3D medium (in the half space) must be defined which significantly increase the computational demand.

PyLith needs a finite element mesh which is tetragonal or hexagonal generated by CUBIT/TRELIS, LaGriT or text editor in Exudus II format. In this study, Trelis is used to define the fault geometry and create tetragonal mesh for a better smoothness at the fault bends. Vertex ordering of the meshes must be in the counterclockwise direction. PyLith is a

portable and scalable program written to identify crustal deformation simulations. Its main use is for quasi-static and dynamic earthquake rupture modelling. The code has two level of programming languages. The high level of the code is written in Python language and works using Pyre, a simulation code written in Caltech, to make simulations. The low level of the code is written in C++ and depends on PETSC in order to perform matrix operations. Also, SWIG program adapts C++ extensions to the Python, and FIAT schedules basis functions and numerical quadrature points.

PyLith can give outputs in VTK or HDF5/xdmf formats and both can be visualized using Paraview or Visit programs. Usage of HDF5/xdmf files significantly decrease required memory and time for the calculation. Since our geometry is larger than 200 km, HDF5/xdmf outputs are used in this study. Therefore, calculation time for each case of the simulation becomes three times shorter (~12 hours) when 256 GB Ram is used for 20 (or 18) cores by Parallel Programming using MPI.

All input data for PyLith must be defined within '.cfg' files. Initial tractions in the along strike, fault normal and up-dip directions, static and dynamic friction coefficients, P and S wave velocities, density, rigidity and critical slip weakening distance are main parameters for the dynamic simulations. Definition of applicable initiation patch size, zero tolerance and zero tolerance normal coefficients (coefficients to prevent fault opening), the CFL (Courant-Friedrick-Lewy) stability condition parameters (dx and dt), and nondimensionalism coefficients are also very important numeric parameters in order to achieve realistic dynamic earthquake scenarios.

5.1. The Methodology

5.1.1. The Equation of Motion for a Linear Elastic Rheology

Considering a volume V that is bounded by surface S, and implementing a Lagrangian definition of the conservation of momentum brings forth the integral form of the equation of motion,

$$\frac{\partial}{\partial_t} \int_V \rho \frac{\partial u_i}{\partial_t} dV = \int_V f_i \, dV + \int_S T_i \, dS \tag{5.1}$$

Here, the left side of the equality is the momentum, and the right side is the summation of body and surface integrations. The relation between the traction vector field and the stress tensor exists via n_j, the vector normal to S (fault surface),

$$T_i = \sigma_{ij} n_{ij}, \tag{5.2}$$

Substituting equation 5.2 into equation 5.1 gives,

$$\frac{\partial}{\partial t} \int_V \rho \frac{\partial u_i}{\partial t} dV = \int_V f_i \, dV + \int_S \sigma_{ij} n_{ij} \, dS \tag{5.3}$$

Applying the divergence theorem to the last (surface integral) term,

$$\int_V a_{i,j} \, dV = \int_S a_j n_j \, dS, \tag{5.4}$$

Thus, the equation 2.3 yields,

$$\frac{\partial}{\partial t} \int_V \rho \frac{\partial u_i}{\partial t} dV = \int_V f_i dV + \int_V \sigma_{ij,j} dV \tag{5.5}$$

$$\int_V \left(\rho \frac{\partial^2 u_i}{\partial t^2} - f_i - \sigma_{ij,j} \right) dV = 0 \tag{5.6}$$

Due to using an arbitrary volume V, the integrand has to be zero everywhere within the volume. Therefore, the following conditions can be defined,

$$\rho \frac{\partial^2 u_i}{\partial t^2} - f_i - \sigma_{ij,j} = 0 \; in \; V \tag{5.7}$$

$$a_{ij} n_j = T_i \; on \; S_T \tag{5.8}$$

$$u_i = u_i^0 \; on \; S_{u,} \; and \tag{5.9}$$

$$R_{ki}(u_i^+ - u_i^-) = d_k \; on \; S_f \tag{5.10}$$

Tractions, T_i, displacements, u_i^0, and slip, d_k, are specified on surface S_f, on surface S_u and on fault surface S_f, respectively. The vector transformation from the global coordinate system to the local (fault) coordinate system is done by the rotation matrix, R_{ki}.

5.1.2. Finite-Element Formulation of Elasticity Equation

They use Galerkin's method in order to derive equations. They make two assumptions; (1) $\vec{u}$, as a vector field, is a trial solution and it is piecewise differentiable and satisfies the Dirichlet boundary conditions on S_u, and (2) $\vec{\varphi}$, as weighting function vector field, is piecewise differentiable and equals zero on S_u. Starting with the strong form of the wave equation,

$$\sigma_{ij,j} + f_i = \rho \ddot{u}_i \ in \ V \tag{5.11}$$

$$\sigma_{ij} n_j = T_i \ on \ S_T \tag{5.12}$$

$$u_i = u_i^0 \ on \ S_u \tag{5.13}$$

$$R_{ki}(u_i^+ - u_i^-) = d_k \ on \ S_f \ and \tag{5.14}$$

$$\sigma_{ij} = \sigma_{ji} \ (symmetric) \tag{5.15}$$

In order to derive the weak form, they use the dot product of the wave equation and the weighting function, and they fit the domain integral to zero:

$$\int_V (\sigma_{i,j,j} + f_i - \rho \ddot{u}_i) \varphi_i dV = 0 \ or \tag{5.16}$$

$$\int_V \sigma_{ij,j} \varphi_i dV + \int_V f_i \varphi_i dV - \int_V \rho \ddot{u}_i \varphi_i dV = 0 \tag{5.17}$$

By the application of the divergence theorem to the dot product of the stress tensor and the weighting function, $\sigma_{ij} \varphi_i$, the following equation is obtained.

$$\int_V (\sigma_{ij}\varphi_i)_{,j}\, dV = \int_S (\sigma_{ij}\varphi_i)n_i\, dS \qquad (5.18)$$

Then by expanding the left hand side of the equation 5.18,

$$\int_V \sigma_{ij,j}\varphi_i\, dV + \int_V \sigma_{ij}\varphi_{i,j}\, dV = \int_S \sigma_{ij}\varphi_i n_i\, dS \ \ or \qquad (5.19)$$

$$\int_V \sigma_{ij,j}\varphi_i\, dV = - \int_V \sigma_{ij}\varphi_{i,j}\, dV + \int_S \sigma_{ij}\varphi_i n_i\, dS \qquad (5.20)$$

Substituting the equation 5.20 into the equation 5.17 (weak form) derives,

$$- \int_V \sigma_{ij}\varphi_{i,j}\, dV + \int_S \sigma_{ij}\varphi_i n_i\, dS + \int_V f_i\varphi_i\, dV - \int_V \rho\ddot{u}_i\varphi_i\, dV = 0 \qquad (5.21)$$

Furthermore, since they consider the integration over S_T and S_u, they separate the integration over S by focusing the second term. Because tractions will be considered only over the fault surface, S_f, as a result of the fault constitutive model, this separation will provide convenience.

$$- \int_V \sigma_{ij}\varphi_{i,j}\, dV + \int_{S_T} \sigma_{ij}\varphi_i n_i\, dS + \int_{S_u} \sigma_{ij}\varphi_i n_i\, dS + \int_V f_i\varphi_i\, dV - \int_V \rho\ddot{u}_i\varphi_i\, dV = 0 \quad (5.22)$$

Remembering the following conditions,

$$\sigma_{ij}n_i = T_i \ on \ S_T \ and \qquad (5.23)$$

$$\varphi_i = 0 \ and \ S_u, \qquad (5.24)$$

the equation becomes,

$$- \int_V \sigma_{ij}\varphi_{i,j}\, dV + \int_{S_T} T_i\varphi_i\, dS + \int_V f_i\varphi_i\, dV - \int_V \rho\ddot{u}_i\varphi_i\, dV = 0 \qquad (5.25)$$

As a result, the trial solution and weighting function as linear combinations of basis functions,

$$u_i = \textstyle\sum_m a_i^m N^m \tag{5.26}$$

$$\varphi_i = \textstyle\sum_n C_i^n N^n \tag{5.27}$$

Due to the Dirichlect boundary conditions and $m > n$, the number of basis functions for u is greater than the one for φ. Substituting equations 5.26 and 5.27 into the equation 5.25,

$$- \int_V \sigma_{ij} \textstyle\sum_n c_i^n N^n{}_{,j} \, dV + \int_{S_T} T_i \textstyle\sum_n c_i^n N^n \, dS + \int_V f_i \textstyle\sum_n c_i^n N^n \, dV -$$
$$\int_V \rho \textstyle\sum_m \ddot{a}_i^m N^m \textstyle\sum_n c_i^n N^n \, dV = 0 \; or \tag{5.28}$$

$$\textstyle\sum_n c_i^n \left(- \int_V \sigma_{ij} N^n{}_{,j} + \int_{S_T} T_i N^n dS + \int_V f_i N^n dV - \int_V \rho \textstyle\sum_m \ddot{a}_i^m N^m N^n dV \right) = 0 \tag{5.29}$$

Since the weighting function is arbitrary, equations 5.28 and 5.29 are valid for all c_i^n. Thus, the quantity in the brackets in equation 5.29 equals zero for each c_i^n

$$- \int_V \sigma_{ij} N^n{}_{,j} dV + \int_{S_T} T_i N^n dS + \int_V f_i N^n dV - \int_V \rho \textstyle\sum_m \ddot{a}_i^m N^m N^n dV = \vec{0} \tag{5.30}$$

This equation should be solved for the unknown coefficients a_i^m depending on,

$$u_i = u_i^0 \; on \; S_u, \; and \tag{5.31}$$

$$R_{ki}(u_i^+ - u_i^-) = d_k \; on \; S_f, \tag{5.32}$$

5.1.3. Solution Method for Dynamic Problems

In the dynamic problems, time dependence enters to the equations via the constitutive relationships, loading conditions, and inertial terms. The time dependency strongly amplifies the problem because calculations are done at each discretized area for each time step considering the previous time steps. In this method, deformation is considered at time t,

$$-\int_V \sigma_{ij}(t)N^n_{,j}dV + \int_{S_T} T_i N^n dS + \int_V f_i(t)N^n dV - \int_V \rho \sum_m \ddot{a}^m_i(t) N^M N^n dV = \vec{0} \quad (5.33)$$

The equation 5.33 is solved via formulation of a linear algebraic system of equations $(Au = b)$, including the Jacobian (A) and residual $(r = b - Au)$. The residual is,

$$r^n_i = -\int_V \sigma_{ij}(t)N^n_{,j}dV + \int_{S_T} T_i(t)N^n dS + \int_V f_i(t)N^n dV - \int_V \rho \sum_m \ddot{a}^m_i(t) N^m N^n dV$$
(5.34)

Next, the integrals with sums over the cells and quadrature points are replaced, and the numerical quadrature in the finite-element discretization is substituted,

$$r^n_i = -\sum_{vol\ cells} \sum_{quad\ pts} \sigma_{ij}(x_q, t)N^n(x_q)w_q |J_{cell}(x_q)| +$$
$$\sum_{vol\ cells} \sum_{quad\ pts} f_i(x_q, t)N^n(x_q)w_q |J_{cell}(x_q)| +$$
$$\sum_{tract\ cells} \sum_{quad\ pts} T_i(x_q, t)N^n(x_q)w_q |J_{cell}(x_q)| -$$
$$\sum_{vol\ cells} \sum_{quad\ pts} \rho \sum_m \ddot{a}^m_i(t)N^m N^n w_{q|J_{cell}(x_q)|} \qquad (5.35)$$

The quadrature points, the weights of the quadrature points and the kernel (Jacobian) matrix at those points related to the reference cell to the real cell are presented by x_q, w_q and $|J_{cell}(x_q)|$, respectively. The integration dimension of tractions is one level lower than the one of volume cells.

The kernel matrix is calculated through the temporary discretization and the isolation of the term considering the increment of the special field at time t. The central difference method is used to apply the acceleration and velocity, and the displacement at time $t + \Delta t$ is obtained using the displacement at time t.

$$u_i(t + \Delta t) = u_i(t) + du_i(t) \qquad (5.36)$$

$$\ddot{u}_i(t) = \frac{1}{\Delta t^2}\left(du_i(t) - u_i(t) + u_i(t - \Delta t)\right) \qquad (5.37)$$

$$\dot{u}_i(t) = \frac{1}{2\Delta t}\left(du_i(t) + u_i(t) - u_i(t - \Delta t)\right) \qquad (5.38)$$

Substituting into equation (5.33) yields,

$$\frac{1}{\Delta t^2} \int_V \rho \sum_m da_i^m(t) N^m N^n dV = - \int_V \sigma_{ij} N_{,j}^n dV + \int_{S_T} T_i N^n dS + \int_V f_i N^n dV -$$

$$\frac{1}{\Delta t^2} \int_V \rho \sum_m \left(a_i^m(t) - a_i^m(t - \Delta t) \right) N^m N^n dV \tag{5.39}$$

Thus, the system kernel (Jacobian) is as following,

$$A_{ij}^{nm} = \delta_{ij} \frac{1}{\Delta t^2} \int_V \rho N^m N^n dV \tag{5.40}$$

Finally, the numerical quadrature in the finite-element discretization is used to remove the integrals. As a result of the substitution of the summations over the cells and quadrature points, the Jacobian of the system is,

$$A_{ij}^{nm} = \delta_{ij} \frac{1}{\Delta t^2} \sum_{vol\ cells} \sum_{quad\ pts} \rho(x_q) N^m(x_q) N^n(x_q) \tag{5.41}$$

Here A_{ij}^{nm} is a nd by md matrix. Also, m and n are basis functions and i and j are components of the vector space, while d is the dimension of the vector space.

In dynamic simulations, an artificial viscosity is added to the numerical damping in order to decrease high frequency oscillations. Thus, the adjusted displacement at time t is $u_i^{adj}(t)$, the original displacement at time t is $u_i(t)$, the normalized artificial viscosity is n^*, the time step is Δt, and the velocity at time t is $du_i(t)$. Although the default value of the artificial viscosity is 0.1, it can be between 0.1 and 0.4 as it does not significantly decrease the peak velocity.

$$u_i^{adj}(t) = u_i(t) + n^* \Delta t\ du_i(t) \tag{5.42}$$

5.2. The Friction Model

A fault constitutive friction model is used in order to derive final traction and slip distributions on the fault surface. Therefore, a linear slip-weakening friction model is used in our study. There is a threshold at the static friction level, so slip is zero and the fault is locked when the driving force is lower than the threshold. The slip starts to occur via the reduced Lagrange multipliers when the driving force exceeds the rupture threshold.

T_y is the yield shear traction, T_o is the initial shear traction, T_f is final shear traction, T_n is normal traction, T_c is cohesion, d is slip, d_0 is critical slip distance, μ_s is static friction coefficient and μ_d is dynamic friction coefficient. The difference between the yield stress and the initial stress is called the strength excess, and the difference between the initial stress and the final stress is stress drop (Fig. 5.1).
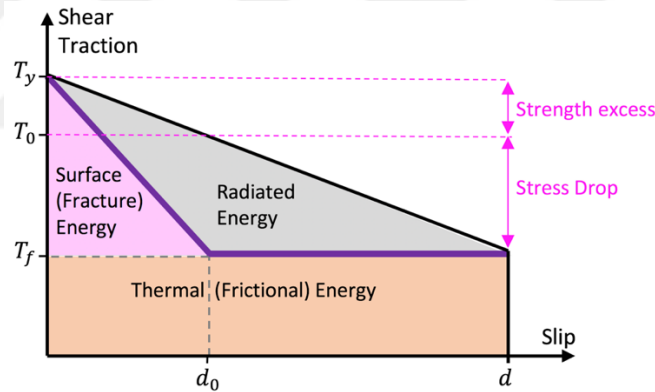
Figure 5.1. The slip-weakening friction model.

Note that σ_n (normal stress) and σ_s (shear stress) can be derived from the following equations coming from the Cauchy's Law,

$$t = \sigma n \qquad (5.43)$$

$$\sigma_n = n.t \qquad (5.44)$$

$$\sigma_s = \sqrt{|t^{(n)}|^2 - \sigma_n{}^2} \qquad (5.45)$$

The fracture criterion is,

$$T_f = \begin{cases} T_c - \left(\mu_s - (\mu_s - \mu_d)\frac{d}{d_0}\right)T_n & d \le d_0 \ and \ T_n \le 0 \\ T_c - \mu_d T_n & d > d_0 \ and \ T_n \le 0 \\ 0 & T_n > 0 \end{cases} \tag{5.46}$$

In our model, cohesion is zero and static and dynamic friction coefficients are fixed as constants, while some external iterations are done for changing static friction coefficients to see its effects.

Moreover, the characteristic length (L_c), critical half-length of a Griffith crack, is the ratio between the surface and strain energies for a unit volume (Andrews, 1976). The dimension of the nucleation patch is scaled with L_c and not with d_0. Therefore, adopted constitutive parameters (a, b, and L from the rate-and-state friction law), having a relation with L_c, control the slip weakening behavior and the absorbed fracture energy (Bizzarri and Cocco, 2003). The equation of the characteristic length and the effective fracture surface energy are defined as following (Andrews, 1976; Aki and Richards, 1980),

$$L_c = \frac{8\mu(\lambda+\mu)}{\pi(\lambda+2\mu)}\frac{G}{(\tau_{0-}\tau_f)^2} \tag{5.47}$$

$$G = \frac{1}{4}(\tau_y - \tau_f)d_c \tag{5.48}$$

Here λ and μ are Lame parameters, and by substituting equation 5.2.6 into equation 5.47, we obtain,

$$L_c = \frac{4}{3}\frac{\mu}{\pi}\frac{(\tau_y - \tau_f)}{(\tau_{0-}\tau_f)^2}d_c \tag{5.49}$$

L_c should be resolved by at least 3-5 grids for the rupture propagation from static to dynamic friction level (Aagaard, et al., 2012). In our study, L_c is solved by 5 and 9 grids for KB and PI initiation of ruptures, respectively.

5.3. Estimation of Initial Normal Stresses from the Regional Stress Loading

Due to the fact that the calculation of the direct stress measurements is not possible within the earth crust, the radiation patterns of seismic waves are used to achieve earthquake characteristics and stress deformations (Kostrov and Das, 2005). Exceptionally, direct stress analysis before and after an earthquake can be done in a borehole in Parkfield, so change in stress and absolute stress can be identified (Seeber, L., discussion). In this study, we focus on along-strike shear stress and normal stress because our fault has right lateral strike-slip behavior. Thus, the up-dip stress is defined as zero for the MMF. Since we are not able to measure absolute values of stress components, it is common to use globally assumed stress values derived from deep borehole and laboratory experiments (Hergert and Heidbach, 2011).

In order to constrain initial normal stress values for each segment, we start by gathering stress axes orientation results from recent seismicity studies including the work presented in previous chapter (Korkusuz Öztürk et al., 2015; Korkusuz Öztürk and Meral Özel, 2018; Pınar et al., 2016; and MarDiM Project). We assume that orientations of normal stress axes are horizontal as it is expected for a strike slip fault (Table 5.1). Namely, we do not consider plunge angles because they are mostly larger than even 45º as a result of usage of small earthquakes which have mainly normal faulting mechanisms. Next, focus on that the segment with the highest stress load is the most possible to be the rupture initiation region. Thus, we assume that the KB Segment (F) is ready to rupture, and the regional normal stress is calculated regarding this criterion (using calculated shear stress and static friction coefficient for this segment). The magnitude of the normal stress on the rest of the segments are calculated using the regional normal stress derived from the KB segment (F). Selections of orientations of normal stresses (slip deficit rate) are done regarding that the shear stress can't be larger than the fracture criterion. Otherwise, the energy must have been already released by an earthquake for the relevant segment.
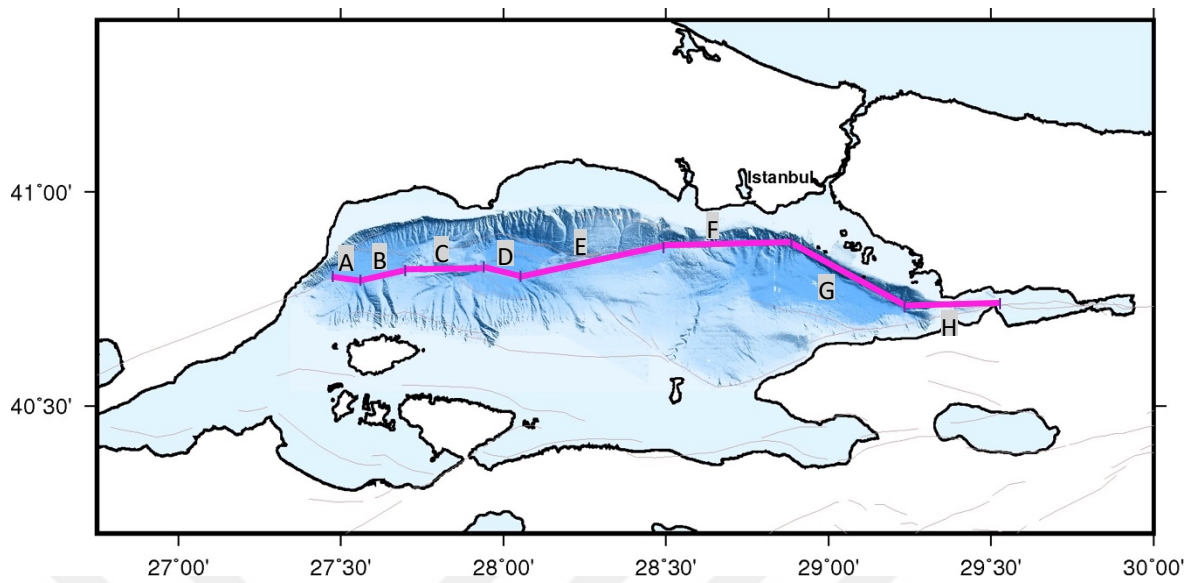
Figure 5.2. Segments of the Main Marmara Fault in our model. Segment A is in Ganos Offshore, B is in Tekirdağ Basin, C is in the Central High, D and E are in the Central Basin, F includes Kumburgaz Basin, G is the Prince's Island segment and H is the İzmit segment.
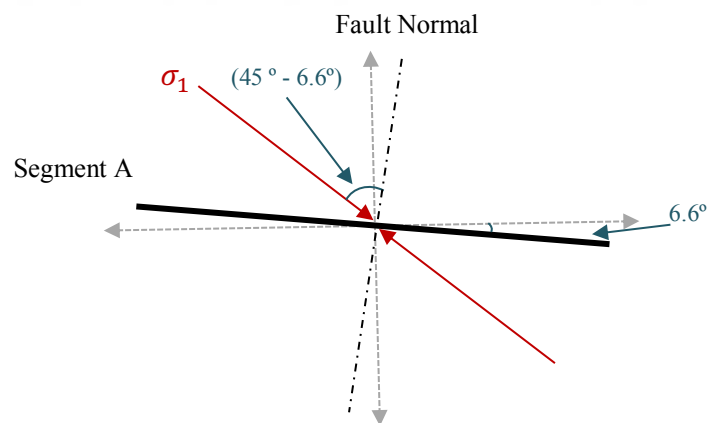
Figure 5.3. The orientation of segment A (black bold line) with its 96.6° strike angle and regional stress with σ_1 axis with its 135° strike angle (red line) are shown. The angle between the fault normal direction and the orientation of σ_1 axis is 38.4°.

Table 5.1. The strike angle and length of each segment are in the second and third columns. Local strike angle findings for the maximum compressive stress axes from recent investigations are in the fourth, fifth, sixth and seventh columns, respectively (Korkusuz Öztürk et al., 2015; Korkusuz Öztürk and Meral Özel, 2018; Pınar et al., 2016; and MarDiM Project). Selected values are highlighted. Calculated normal tractions are presented in the last column.

Segment	Strike (º)	Length (km)	Study-1 (º)	Study-2 (º)	Study-3 (º)	Study-4 (º)	Traction (MPa)
A (GS)	96.6	6.5	315	-	-	312	131.706226
B (TB)	79.4	13.0	293	-	-	321	117.339408
C (WH)	88.0	19.1	293	-	-	321	89.610650
D (CB left)	105.0	9.0	-	90	-	172	195.180961
E (CB right)	77.8	39.8	-	-	-	172	211.467432
F (KB)	90.0	38.28	-	-	-	172	209.973334
G (PI)	119.0	33.6	123	-	154	-	121.619348
H (IS)	90.0	27.5	-	-	296	-	92.950842

5.4. Estimation of Initial Shear (Along-Strike) Tractions from Inter-seismic and Historical Data

Since slip-rate gives significant information about seismic potential of a region and controls accumulated strain on the fault which releases during an earthquake, we calculate initial shear stress amounts by choosing slip-rates from recent geodetic studies (Klein et al., 2017; Ergintav et al., 2014; Hergert and Heidbach, 2010). Therefore, shear traction is calculated via below assumptions using recent slip deficit rate results,

$$T_{shear} = \mu . \varepsilon_{shear} . Time \qquad (5.50)$$

T_{shear}, μ, and ε_{shear} are shear traction, rigidity and shear strain, respectively. Shear traction is calculated by multiplying rigidity, annual shear strain rate and elapsed time since the last $M \geq 7.0$ event;

$$T_{shear} = \mu(Pa) \frac{Slip\ Deficit\ Rate\ (m/yr)}{Unit\ Length\ (m)}\ passed\ time\ (yr) \tag{5.51}$$

This calculation is done for every segment. For example, shear traction for Kumburgaz Basin (Segment F) is calculated as following;

μ = 32 GPa

Slip deficit rate = 15.49 mm/yr

Passed time = 2020 - 1766 = 254 yr

Unit length = 1 km = 1000000 mm

Shear traction = 125.90272 MPa

Because slip deficits are determined parallel to the fault segments (in the along strike directions), they are directly used to calculate shear tractions.

Since we assume that the KB segment is ready to rupture by completing its period, the calculated shear traction almost equals to the yield traction. Namely, T_o = 125.90272 MPa and T_y = 126.102720 MPa. Therefore, strength excess is 0.2 MPa. As a result, by the assumption of μ_s = 0.6 (static friction coefficient), the normal traction (T_n) must be 209.973334 MPa (Table 5.2), as the static friction threshold equals to the multiplication of the normal stress and the static friction coefficient (the rupture criterion).

Another issue when determining the crustal stress for the earthquake rupture simulation is to characterize the depth dependence of stress. Although it is known that stress increases with depth (Aochi and Ulrich, 2015) it is not clear how it should be modified with depth. Essentially, not only the amplitude of stress increases but also the direction of the stress changes with depth (Leonardo Seeber, discussion, 16 March 2018). Since our fault geometry is vertical with 90° dip angle, except for the PI segment, the directional change in stress may be ignored. In addition, some laboratory experiments present a constant fault strength on over pressured areas (Suppe, 2014) which we assume in this study. Assuming that the Main Marmara Fault is ready to rupture as its period is completed, and shear stress can be assumed constant for strike slip faults within the seismogenic zones, we assume that stress is not changing with depth (Prof. Dr. Peter Molnar from University of Colorado and Prof. Dr. Leonardo Seeber from Columbia University, discussions in January and March

2018, respectively; Suppe, 2014). Therefore, the shear stress is calculated via given one dimensional relation (eq. 5.51).

Table 5.2. The duration (year) since the last destructive event is shown in the second column. Annual slip-rates of each segment are from Hergert and Heidbach (2010; study-1), Ergintav et al. (2014; study-2), and Klein et al. (2017; study-3). Selected slip deficit rates (highlighted) are in the sixth column and calculated along strike shear tractions are in the last column.

Segment	Year Passed (yr)	Study-1 (mm/yr)	Study-2 (mm/yr)	Study3 (mm/yr)	Slip-Deficit Rate (mm/yr)	Traction (MPa)
A (GS)	2020 - 1912 = 108	14-16	18-23	<10	20.0	69.120000
B (TB)	2020 - 1912 = 108	15-16	-	20-25	20.0	69.120000
C (WH)	2020 - 1912 = 108	16-18	2-4	20-30	15.5	53.568000
D (CB west)	2020 - 1766 = 254	15-16	2-4	20-30	14.4	117.043200
E (CB east)	2020 - 1766 = 254	15-17	2-4	15-20	15.6	126.796800
F (KB)	2020 - 1766 = 254	14-16	-	15-20	15.49	125.90272
G (PI)	2020 - 1766 = 254 or 2020 – 1894 = 126	12-14	8-15	12-18	8.95 or 14.0	72.745600 56.448000
H (IS)	2020 - 1999 = 21	14-15	26-30	<10	15.0	10.080000

5.5. Seismic Moment, Moment Magnitude and Rupture Velocity Calculations

One macroscopic parameter from the rupture scenarios is the seismic moment. Total seismic moment is calculated by the summation of seismic moment for each sub-fault (200 m sided equilateral triangles) which is the multiplication of rigidity, average slip and surface area. The unit of seismic moment, M_o, can be defined by N.m or dyne.cm. In the following equation average slip is defined by D and surface area is shown by symbol A where μ is rigidity,

$$M_0 = \mu\, D\, A \tag{5.52}$$

Moment magnitude, M_w, is calculated via below equation (Kanamori, 1977),

$$M_w = 2/3(logM_0 - 9.1) \tag{5.53}$$

Slip is the discontinuity of displacement on the fault surface while displacement is the change in the location due to slip on the fault and can be calculated at an arbitrary location. Hence, slip-rate (slip velocity) is measured on the fault surface, while ground velocity is measured on the ground surface. The slip-rate (V_{peak}) is linearly related to the velocity on the ground surface via the representation theorem (Aki and Richards, 2002), while the rupture velocity (V_r) manages the frequency context of the particle velocity (Bizzarri, 2012; Bizzarri et al., 2010). The peak slip velocity is also important to deduce the characteristic length (L_c) that is the distance needed for the finalization of stress release (Mikumo et al., 2003; Tinti et al., 2004). V_{peak} quadratically increase with arising rupture velocity (Bizzarri, 2012). Therefore, the rupture energy, the stress drop, cumulative slip, the peak slip velocity and the rupture velocity are very significant for spontaneous dynamic earthquake fracture simulations (Bizzarri et al., 2012). V_{peak} arises with the magnitude of the earthquake and it saturates for $M_w > 7.0$ which is valid for most of our simulation results, as well (Abrahamson and Silva, 2008; Boore and Atkinson, 2008). As a result, rupture velocity is calculated using peak slip velocity equation from Bizzarri (2012),

$$\langle V_{peak} \rangle = A e^{B\frac{\langle V_r \rangle}{V_s}} \tag{5.54}$$

$$\langle V_r \rangle = \frac{V_s \, In(\frac{\langle V_{peak} \rangle}{A})}{B} \tag{5.55}$$

5.7. Nondimensionality and Stability Conditions

Nondimensionality is a requirement for numerical problems in order not to lose important digits during long calculations. For example, rigidity is in the order of GPa, so when it is multiplied by other parameters, important digits can be ignored easily or the computation time increases. Therefore, normalization of variables is a need for numerical problems. Normalizations in PyLith are done via below equations;

length scale	= shear wave speed * period	(5.56)
time scale	= period	(5.57)
density scale	= mass density	(5.58)
pressure	= density scale * velocity scale * velocity scale	(5.59)

So we only adjust the mass density, shear wave speed and wave period as following;

wave period   = 1.0 s

mass density   = 2.67e+3 kg/m^3

shear wave speed = 3.5e+3 m/s

The CFL stability condition is used for the numerical calculations. The stability coefficient, C, (eqn. 5.60) should be smaller than '1' for stability. Sensitivity of our simulations are very high as shown by the stability coefficient which is C < 0.2. Our parameters as following;

$$C = \frac{v.dt}{dx} = \frac{3500\frac{m}{s} \, 0.01 \, s}{200 \, m} = 0.175 \qquad (5.60)$$

Dx is the grid size of each sub-fault and dt is the time interval between each calculation step. Even though good results are obtained with 300 m grid size and 0.015 s time step, considering our complex geometry, dx = 200 m and dt = 0.01s are chosen.
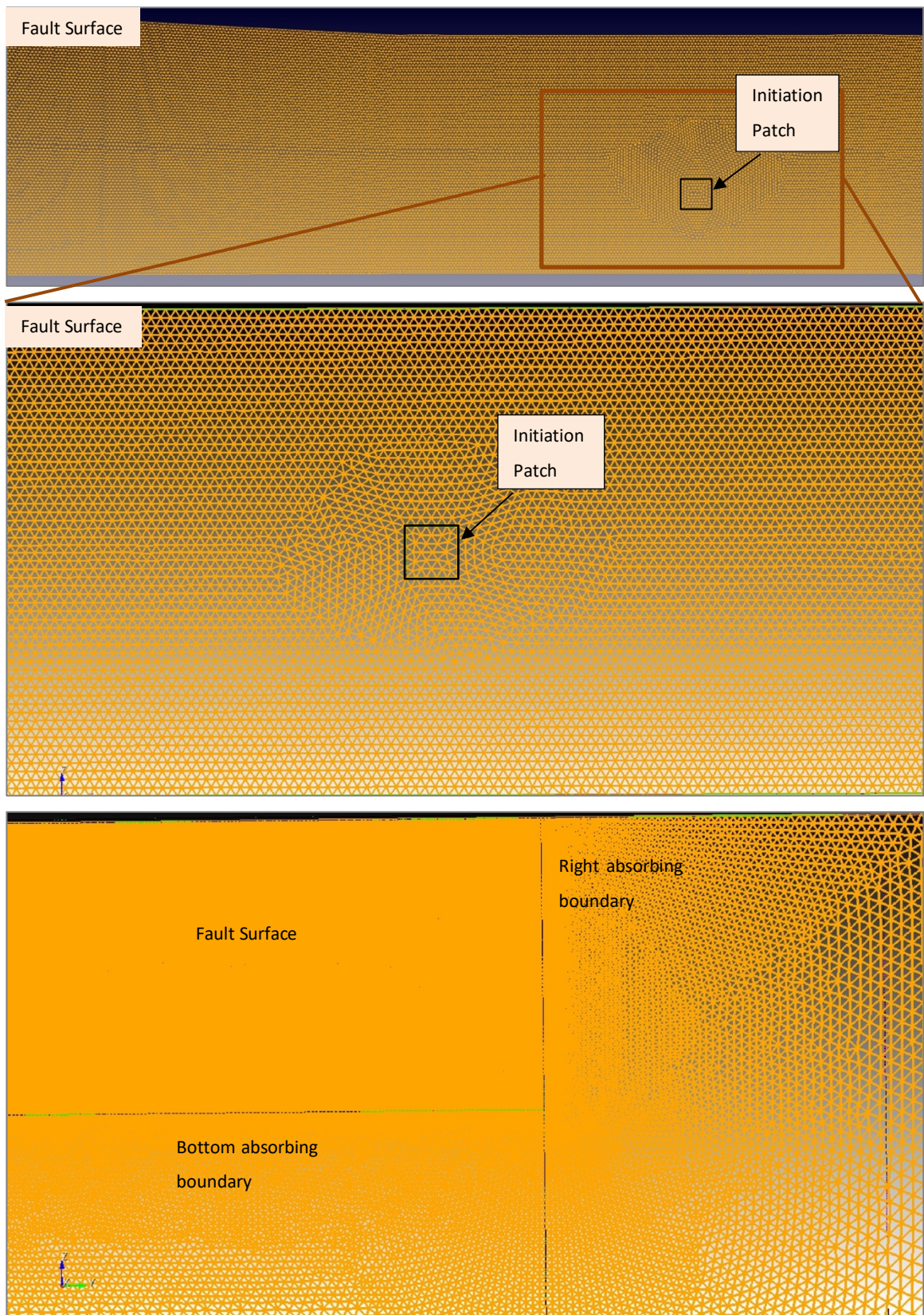
Figure 5.4. Triangular mesh on the fault surface (top and middle) and absorbing boundaries (bottom).
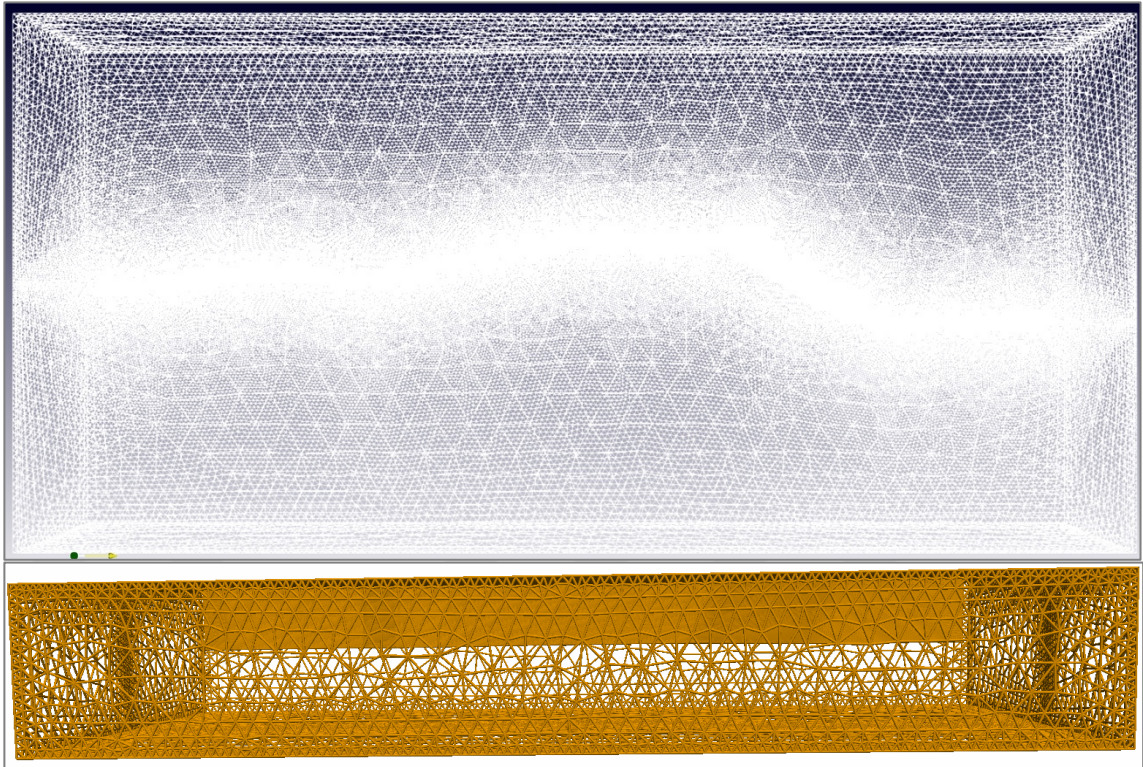
Figure 5.5. Top (top) and side (bottom) views of the gridded 3D medium.
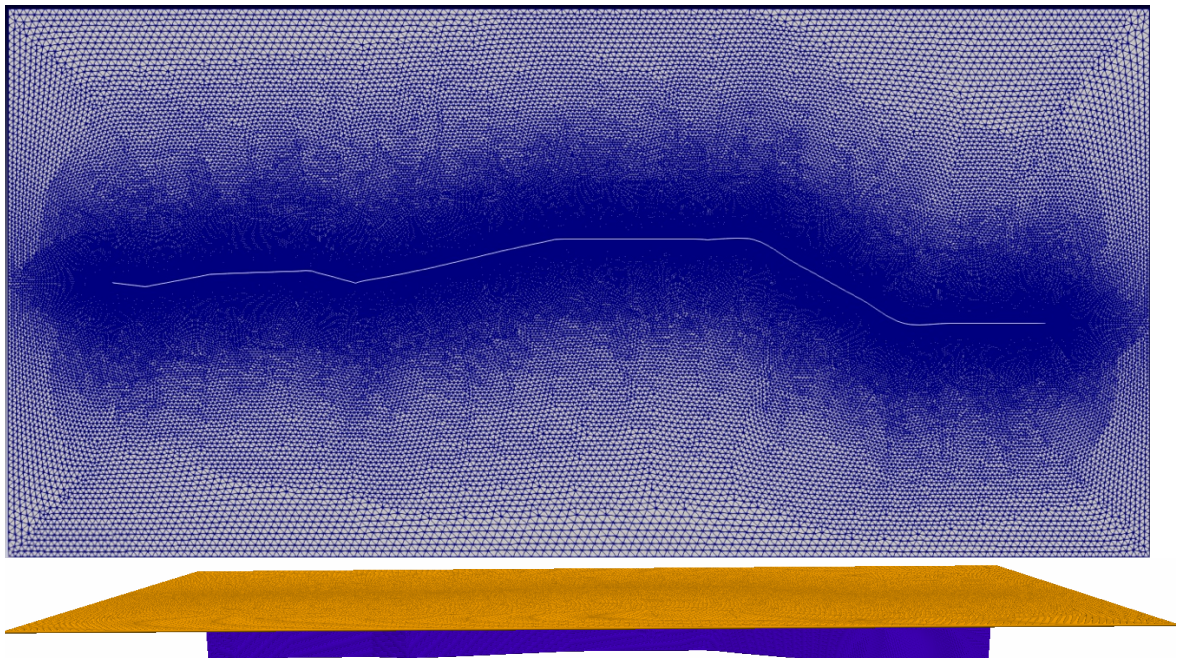
Figure 5.6. Triangular mesh on the ground surface is given at the top figure. Ground (orange) and fault (purple) surfaces are shown at the top figure.

5.8. Identifications of Dynamic Rupture Parameters

Seismologists in general debate on faults are weak or strong. For instance, Aochi and Ulrich (2015) use static friction coefficient as 0.3 implying a weak fault model, while Oglesby and Mai (2012) use static friction coefficient as 0.6 indicating a strong fault model. In our study, since we put constraints on initial shear and normal stress values, the static friction coefficient is not optional. Since multiplication of normal stress and static friction coefficient must not be smaller than the shear stress, the static friction coefficient is selected as 0.6. Dynamic friction coefficient is identified depending on stress drop and maximum final slip amounts. When a weak fault model is used in our model, normal stress values must be selected twice larger. Our trial simulations using a weak fault model ends up with similar rupture scenarios since the stress drop is roughly the same. In this study, we opted for a strong fault model so that we don't have to modify shear stresses calculated from loading rates and use normal stress in the order of ~100 MPa.

We use tetragonal mesh within the finite element discretization for all simulations in order to obtain a better smoothness at the fault bends. For a better understanding of the PyLith simulation code, planar one segment and piecewise planar two segments models are created. We tried using several grid sizes and time steps in order to test the stability of our code using the results from the same rupture scenario from Kaneko (SCEC web page). These tests show that changes in rupture dynamics are insignificant for both models for 100 m, 200 m and 300 m grid sizes and for 0.01 s, 0.0125 s and 0.0175 s time steps, respectively. Minor delay times (<0.5 s) observed when the results for 300 m grid size compared with Kaneko's slip, slip-rate and traction changes time dependently. On the other hand, we observe that delay times in the waveforms at the observation points may increase depending on the shape of the geometry.

Moreover, mesh refinement is done for the MMF in order to be able to make iterations for smaller grid sizes (<200m). During this process, we pretend that the program will solve the problem for 400 m grid size in the beginning, but during the run of the PyLith simulation code, the program divides each equally sided tetragonal cell into 8 equally sided tetragonal cells. As a result, our findings are exactly the same comparing with the results from 200 m

grid size. Hence, 200 m grid size is selected considering long time consuming of the mesh refined case, and all surfaces are divided into thousands of equally sided unstructured triangular meshes. Time step is selected as 0.01 s to decrease the CFL stability condition to 0.175 in order to decrease numerical errors. Since we model first 35 seconds to observe the termination of the rupture, calculations of the kernels of the finite element solution are done dynamically 3500 times for each cell. The number of cells on the fault and ground surfaces are 161.000 and 182.000, respectively. The total number of finite element cells is ~18 million in the elastic medium.

Since a FEM code is used, we are not able to define boundaries of the rupture propagation considering travel times of body waves. Therefore, identification of the size of the absorbing boundaries at the bottom, left and right side of the fault surface is also another significant issue to prevent backward slip. The length of the absorbing boundaries should be long enough to allow termination of the rupture to prevent backward slip, but it should be the shortest in order not to hinder applicability of the model. In this study, 20.0 km length absorbing boundaries are used as a result of iterations. Moreover, free surface conditions are used for the ground surface and ground surface is modelled ~ 53 km from both sides of the fault.

In order to adapt nonplanar fault geometries to the PyLith, nonlinear solver parameters, zero tolerance and zero tolerance normal coefficients must be defined to detect slip. They must become larger than linear solver parameters. Zero tolerance coefficient is used to detect zero values, while zero tolerance normal coefficient is used for repressing near zero values. Their default value for planar fault geometries is 1.0e-10 and they can be 1.0e-5 for nonplanar geometries. As a result of a number of iterations for dynamic physical and numerical parameters, zero tolerance and zero tolerance normal coefficients are identified as 1.0e-10 and 1.0e-7 in this study, respectively. This feature has been recently added into PyLith 2.2.1, so zero tolerance values can't be modified in previous versions which means that previous versions of the code are inadequate non-planar geometries.

Table 5.3. Selected parameters for the entire fault geometry.

Parameter	Value	Resource
Fault Length	221 km	Armijo et al. (2015)
Fault Width (Depth)	15 km	Schmittbuhl et al. (2015)
Dc = Do	0.4 m	From iterations for 0.1 m between 0.1 m and 2.0 m
Vp	6.1 km/s	Karabulut et al. (2011)
Vs	3.5 km/s	Karabulut et al. (2011)
Vp/Vs	1.74	Karabulut et al. (2011)
Density	2670.0 kg/m^3	Global Value
Rigidity	32 Gpa	Global Value
Viscosity	0.1	From iterations for 0.1 between 0.1 and 0.4
CFL Condition Number	0.175	Dt.Vs/Dx=(0.01s.3500m/s)/200m
Static Friction Coefficient	0.6	From calculations
Dynamic Friction Coefficient	0.5714	From calculations

Table 5.4. Selected parameters at the rupture initiation patches as a result of iterations and calculations for rupture initiations at segments KB and PI.

Property	KB Initiations	PI Initiation
Hypocentral Depth	10 km	7.5 km
Characteristic Length (Lc)	0.950 km	1.810 km
Initiation Patch (square)	1.915 km x 1.915 km	3.8 km x 3.8 km
Stress Drop at initiation segment	6.005 MPa	3.478 MPa
Strength Excess	0.2 Mpa	0.46 MPa

5.9. Simulation Models for the MMF

The main focus of this study is to perform realistic dynamic rupture simulations for the Main Marmara Fault, considering both past earthquakes, slip-rates on fault and heterogeneity in coupling on the fault. As discussed previously, recent studies of paleoseismology, geodesy and seismology put some constraint on these parameters but none of them are well-determined. Therefore, we need to perform multiple dynamic rupture scenarios considering uncertainties of the information related to the state of stress on the fault. Below, we review some studies that reveal some information about the interseismic

behavior of various segments of the MMF and explain how we built scenarios in consideration of the information.

On the Main Marmara Fault, very moderate, less than 6 mm/yr, surface creep exists in the Eastern High region (Sakıç et al., 2016) which is located at the eastern part of the Kumburgaz Basin segment in our fault model. On the other hand, no clear information is gathered on the Kumburgaz Basin up until now. Thus, KB segment is assumed to be totally locked. In the current study, partial creeping behavior of Western High and Central Marmara Basin segments is considered. A recent geodetic study presents ~2mm/yr slip-rate in the Central Marmara Sea (Ergintav et al. 2014) implying that the region is creeping. Hence, seismic studies recently focused on repeating earthquake analyzes as asperities should exist in the partially creeping regions and they may be investigated by earthquakes occurring with some intervals with similar characteristics (Yamamoto et al. 2019; Uchida et al. 2018; Bohnhoff et al. 2017; Schmittbuhl et al. 2016; Schmittbuhl et al. 2015). Occurrence intervals and magnitudes of such earthquakes can give significant information about properties of locked layers of the segments (asperities).

Yamamoto et al., (2019) suggest a tempering structure that is fifty percent locked at the top and fully locked between 8-11 km depths at the WH segment (Fig. 5.7, Fig. 5.9 and Fig. 5.10). Our simulation cases for 74% locking (in total) at segment C (tempering) corresponds to the suggestion of this study. Uchida et al., (2019) define two repeater earthquakes between 6-12 km depths at segment C (Western High), two repeater events between 5-14 km depths at segment D (West Central Basin) and three repeater events between 9-14 km depths at segment E (East Central Basin). On the other hand, we define different locking layers in our models for segments C, D and E, as a result of discussions with Prof. Dr. Hayrullah Karabulut. Hence, the seismogenic zone is assumed to be 12 km deep for those creeping segments (Figures 5.8 to Fig. 5.11). In terms of a recent seismicity study, KB segment (F) is fully locked above ~10 km depth, while TB and CB segments (C, D and E) are partially creeping (Schmittbuhl et al. 2016). Hence, segment F is fully locked above 13 km depth in our simulations and estimated to be the most probable starting point of an earthquake rupture (Figures 5.8 to Fig. 5.11). Bohnhoff et al. (2017) represented that WH is 75% locked, while CB is 25% locked, so some of our cases are based on this assumption (Fig. 5.8).

As a result, although there is convincing evidence about the existence of the significant amount of creep at the segments D and E (CB), even though their creep rates are not clear (Fig. 5.7). Also, the partial creep at the segment C (TB) is known to be around 75%. Therefore, in this thesis study, we aim to investigate the effect of this partial creep at WH and CB by changing partially creep amounts and locations of locked layers regarding to abovementioned recent studies and our remarks.

We define three different possible initiation points on KB and PI faults for the expected earthquake on the MMF because these segments are totally locked in terms of recent studies while others are partially creeping or do not have adequate stress to create a large earthquake. One of the hypocenter points is located at the eastern boundary of the KB (KBeast in) at 10 km depth regarding that it is probable to initiate an earthquake at the boundary between seismically active and inactive areas. The region also corresponds to a transition zone between low and high P wave velocities (Barış et al., 2005). The second possible hypocenter point is in the mid of the KB (KB in) at 10 km depth, and the third one is in the mid of the PI (PI in) fault at 7.5 km depth. Namely, it has been accepted that earthquakes initiate at the bottom of the locked zones Actually, rupture can initiate at both ends of the segments, but we selected these three possible points considering that no important difference is observed in slip amounts when we compared results for central and eastern KB initiations. All three initiation points are analyzed for the assumption that PI last ruptured at 1766, whether only two KB initiation cases are modelled for PI last ruptured at 1894 because the loaded energy in segment PI is not sufficient to start a rupture on segment PI for the 1894 rupture. Models are created for 5 different cases in WH and for 10 different cases in CB. As a result of our selections, 16 models are simulated for each initiation point and for the assumptions; PI fault might have broken during 1766 earthquake or 1894 earthquake (Table 6.1).

Our fault geometry is very similar with the geometry of Oglesby and Mai (2012). On the other hand, we remove a 2.4 km long questionable segment between segments E and F (Fig. 5.7). Thus, strike angles of segment F and H are 1.4° rotated in the clockwise direction (Table 5.5). The complexity of the fault geometry significantly effects applicability of dynamic simulations, so generally smoothing (e.g. 500 m, 1000 m, …) is done at segment edges as it has been done in previous studies in the Sea of Marmara (Aochi and Ulrich, 2015; and Oglesby and Mai, 2012). Contrary to previous studies (Aochi and Ulrich, 2015; Oglesby

and Mai, 2012), no smoothing is done at the fault edges, so a purely sharp geometry is used, except for the PI segment. For PI fault, 7.6 km long slightly curvilinear areas are created at the both edges of the segment, but the location of the edge points are not changed. Otherwise, Trelis software does not let us to divide the 3D medium into two parts using the fault surface. Both sides (blocks) of the fault surface can be defined only with this assumption. Furthermore, the locking depth of each segment is determined considering cross sections of the seismicity map of the Marmara Sea (Schmittbuhl et al., 2015).

Table 5.5. Selected segment parameters for the MMF.

Segment	Length (km)	Strike (°)	Dip (°)	Seismogenic Depth (km)	Last Ruptured (yr)
A (GS)	6.5	96.6	90	13.0	1912
B (TB east)	13.0	79.4	90	13.0	1912
C (WH)	19.1	88.0	90	12.0	1912
D (CB west)	9.0	105.0	90	12.0	1766
E (CB east)	39.8	77.8	90	12.0	1766
F (KB)	38.28	90.0	90	13.0	1766
G (PI)	33.6	119.0	70	10.0	1766 or 1894
H (IS)	27.5	90.0	90	13.0	1999

Within the label 'Cx-y', 'x' presents the case details for the WH segment (C) and 'y' represents details for the Central Basin segments (D and E). For example, for cases C1-y, WH segment is 75% locked at different depths, and CB segments (D and E) are 25% locked at different locking depths by changing 'y'. For cases C2-y and C3-y, WH segment is %74 locked (tempering). CB segments (D and E) are 25% and 50% locked for cases C2-y and C3-y, respectively. Thus, depths of locking layers for the CB segments are changing by 'y'.

Figure 5.7. The Main Marmara Fault and names of the segments. Selected possible initiation points are shown by red stars and their code names.
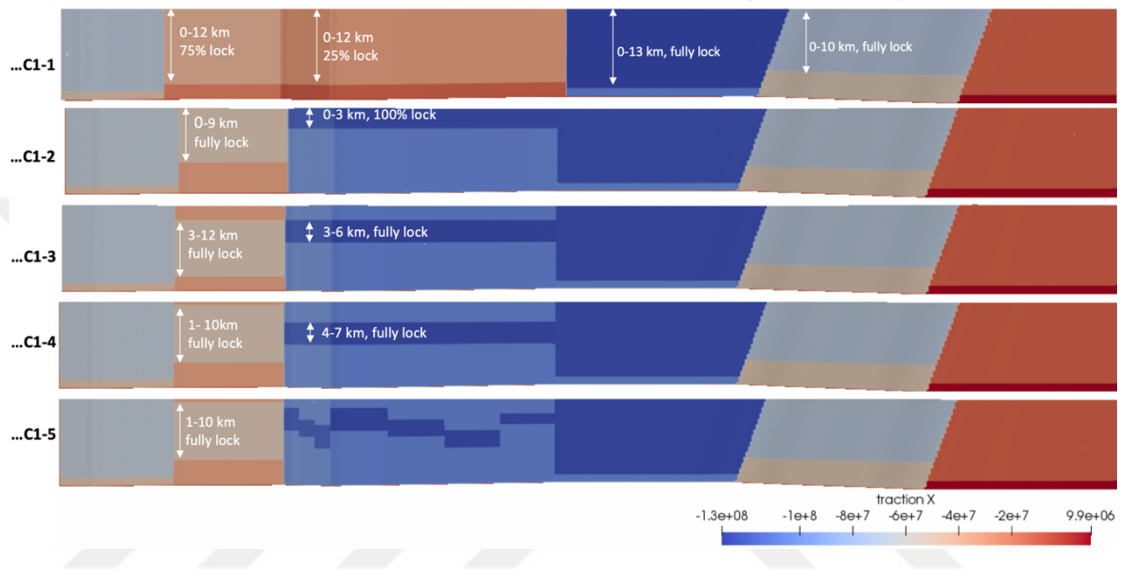
Figure 5.8. Initial shear (along strike) tractions on the fault surface. Figures from top to bottom are for cases; '…C1-1', '…C1-2', '…C1-3', '…C1-4', and '…C1-5', respectively.
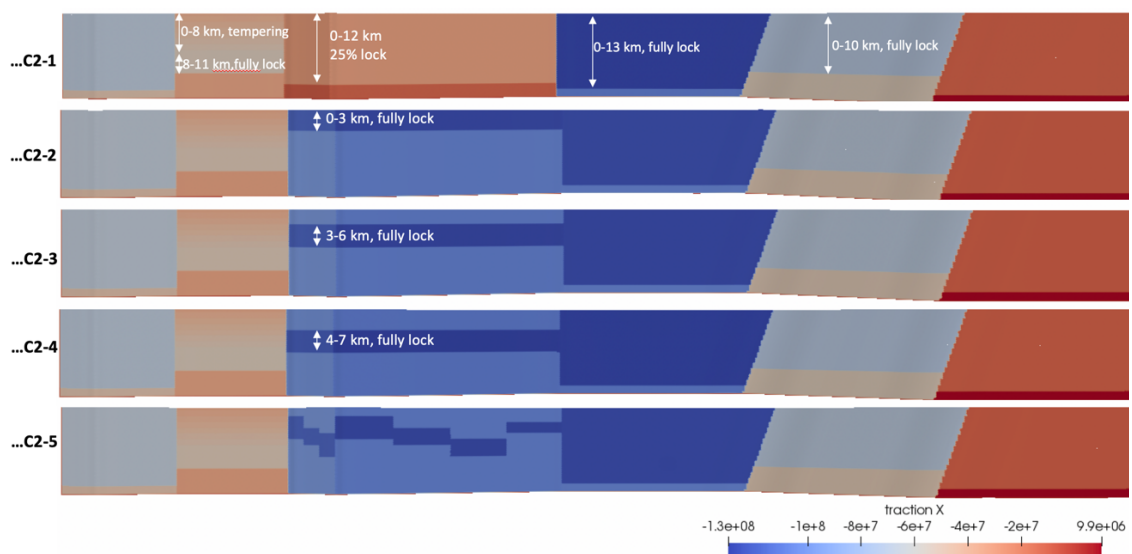
Figure 5.9. Initial shear (along strike) tractions on the fault surface. Figures from top to bottom are for cases; '…C2-1', '…C2-2', '…C2-3', '…C2-4', and '…C2-5', respectively.
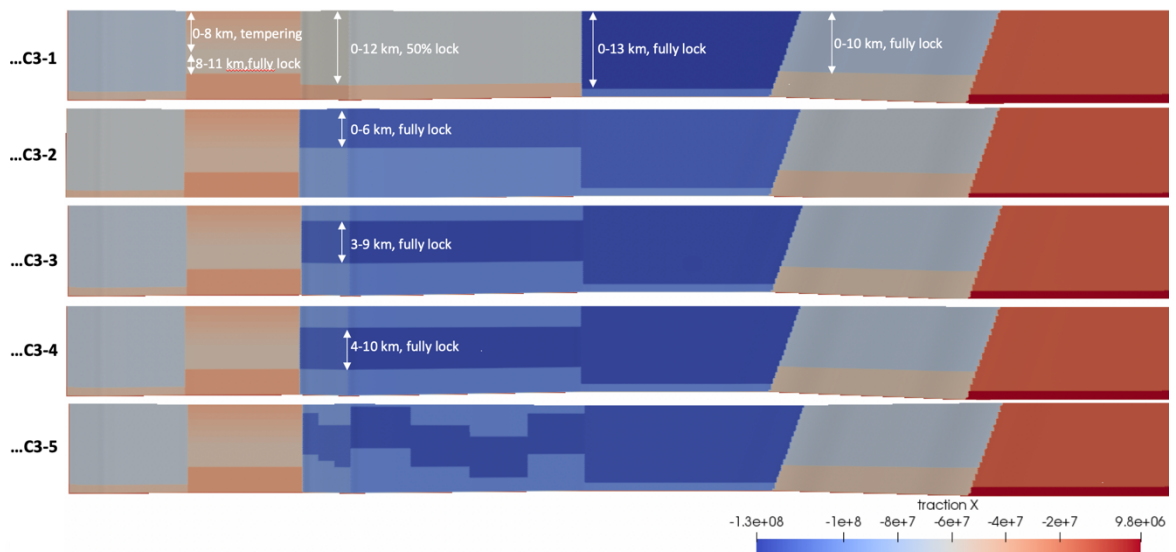
Figure 5.10. Initial shear (along strike) tractions on the fault surface. Figures from top to bottom are for cases; '…C3-1', '…C3-2', '…C3-3', '…C3-4', and '…C3-5', respectively.

Figure 5.11. Initial shear (along strike) tractions on the fault surface for a fully locked model; '…C4'.

For models '…C1-1', WH and CB segments are partially locked homogenously (no asperity embedded), and locking percentages are 75% and 25%, respectively (Fig. 5.8) (Bohnhoff et al., 2017; and Schmittbuhl et al. 2016). For cases '…C1-2', '…C1-3', '…C1-4' and '…C1-5', WH and CB segments have locked layers between 0-9 km and 0-3 km, 3-12 km and 3-6 km, 1-10 km and 4-7 km depth intervals, respectively (Fig. 5.8). The rest of segments are supposed to be fully creeping. For models '…C2-y' and '…C3-y', WH segment is partially locked up to 8 km depth by tempering with the increasing depth, and the segment is totally locked between 8 km and 11 km depths (Yamamoto et al., 2019) (Fig. 5.9 and 5.10). Also, a fully locked fault model ('…C4') is analyzed for each rupture initiation point considering that the PI segment last ruptured at 1766 or 1894 (Fig. 5.11).

5.10. Difficulties during Rupture Simulations

Singularities, due to incompatibility of physical and numerical parameters, are primary problems in numerical simulations. Removing unstable points is a challenge both in BIEM and FEM analyzes. In our FEM analyzes final stress becomes zero at singular points and stress drop becomes very high. On the other hand, these singular points do not affect other (neighboring) points, as we verified, but in our BIEM analyzes such points may affect all points. Fortunately, as a result of a number of iterations and finding the best numerical values (fault opening permission coefficients), all unstable points could be removed from the used FEM (Pylith) based simulation code.

One of the main problems during dynamic simulations is the requirement parallel programming. The memory used during our dynamic earthquake fracture simulations for the MMF is 256 GB (for FEM), and each iteration ends up in ~12 hours for '.xdmf' (HDF5) outputs and ~36 hours for '.VTK' (ASCII) outputs for 35 seconds long simulations (dx = 200 m and dt = 0.01 s).

Another problem for numerical simulations using FEM is the creation of the complex fault geometry and unstructured mesh within the three dimensional medium. Such a problem is not seen for BIEM case because only the generation of the fault and ground surface are enough as boundaries of the seismic waves are already defined by their travel times. Our problem for FEM case originates from the Trelis code (to define the geometry and generate mesh). Our real fault geometry is complex, the 3D medium is needed to be divided into two blocks, and absorbing boundaries must be defined at fault edges, as boundary conditions are not defined in the finite element approach. Therefore, creation of such a complex and large geometry, and generation of tetragonal mesh lead important problems. As a result, a 2.4 km segment is removed between segments between segments E and F, and curvilinear bends are created at both edges of the segment G (PI).

Moreover, every numerical and physical parameter strongly depends on each other (e.g. the stability condition, fault opening, frictional parameters). Especially, considering rupture initiation and extension criteria, which can chance depending on the complexity of

the geometry, need to be changed against minor changes in the other parameters or rupture criteria.

Furthermore, constraining the regional normal stress is also a problem. When local normal stress components are calculated from recent stress tensor orientation alignment results, the magnitude of local normal stress may not enough to keep the segment unruptured. Therefore, the selection of realistic slip deficit rates solved the problem (Table 5.2).

Finally, estimation of the date and extension of last devastating earthquakes of each segment is also very difficult due to in sufficient historical records and turbidity studies. As a result of combination of these studies, this problem is tried to be fixed.

6. RESULTS AND DISCUSSION

6.1. SCEC TPV205 Test Case

In order to understand the working logic of Trelis and PyLith programs and identify the most useful discretization parameters (dx and dt) for the CFL (Courant- Friedrichs-Lewy) stability condition, SCEC TPV205 test case is analyzed. Thus, accuracy of our simulations can be verified. Besides, TPV205 case is the same with TPV5, having stress heterogeneities, and the only difference is in the differential mesh.

Since 3D rupture simulation processes require high computing demand, determination of the largest discretization parameters and giving stable results at the same time, are significant. Details of the fault model are shown below:

Length = 30 km, Width = 15 km, Mesh type= Tetragon

Critical slip distance (dc)=0.4 m

Initiation patch = 3kmx3km, hypocenter is at the center (at 7.5 km depth)

Higher stress patch = At the left side of the fault

Lower stress patch = At the right side of the fault

Absorbing boundary conditions are used instead of strong boundaries (with a high static friction coefficient) exist at the outside of the fault area.
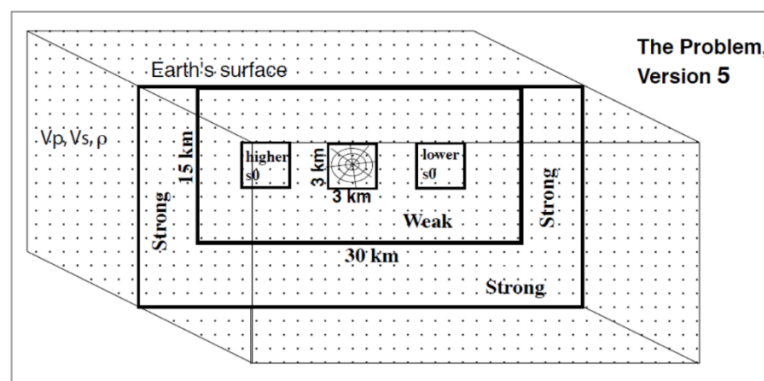
Figure 6.1. Definition of SCEC TPV5 and TPV205 geometry.
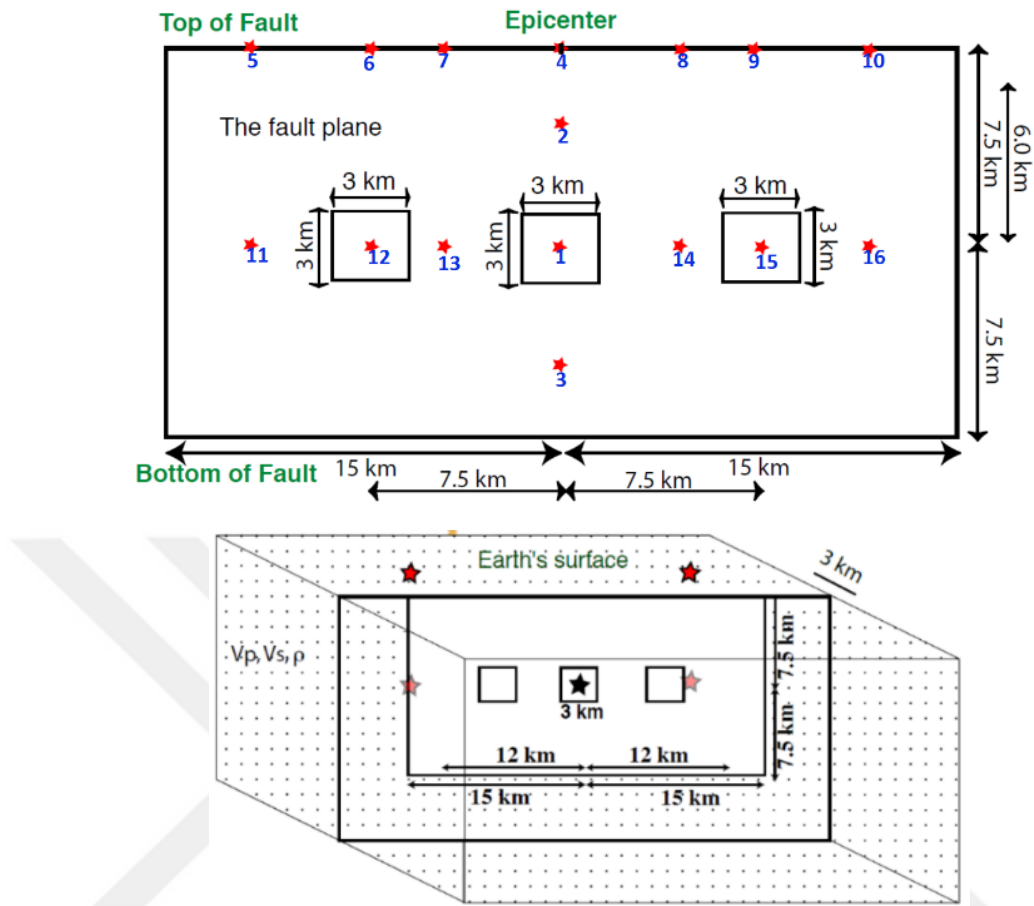
Figure 6.2. Positions of on-fault (top) and off-fault (bottom) observation points.

For the purpose of the determination of the largest dx and dt values, a number of runs are processed. As a result;

if dx>300m, large delay times occur in time dependent slip, slip-rate and traction outputs.
If dx=300m, dt can not be larger than 0.0225s.
If dx=200m, dt can not be larger than 0.015s.

Therefore, 200m or 300m mesh size on the fault surface can give us reliable results for the whole rupture area. On the other hand, especially the determination of dt values for a specific value of dx still requires attention because our real geometry will not have a structured mesh on the fault surface. Namely, some grid sizes may become smaller or larger than the average dx distance, so the range for suitable dt values can be shorter than the SCEC case. Considering CFL stability condition, **$v.dt \le dx$** must be satisfied (*v* is velocity).
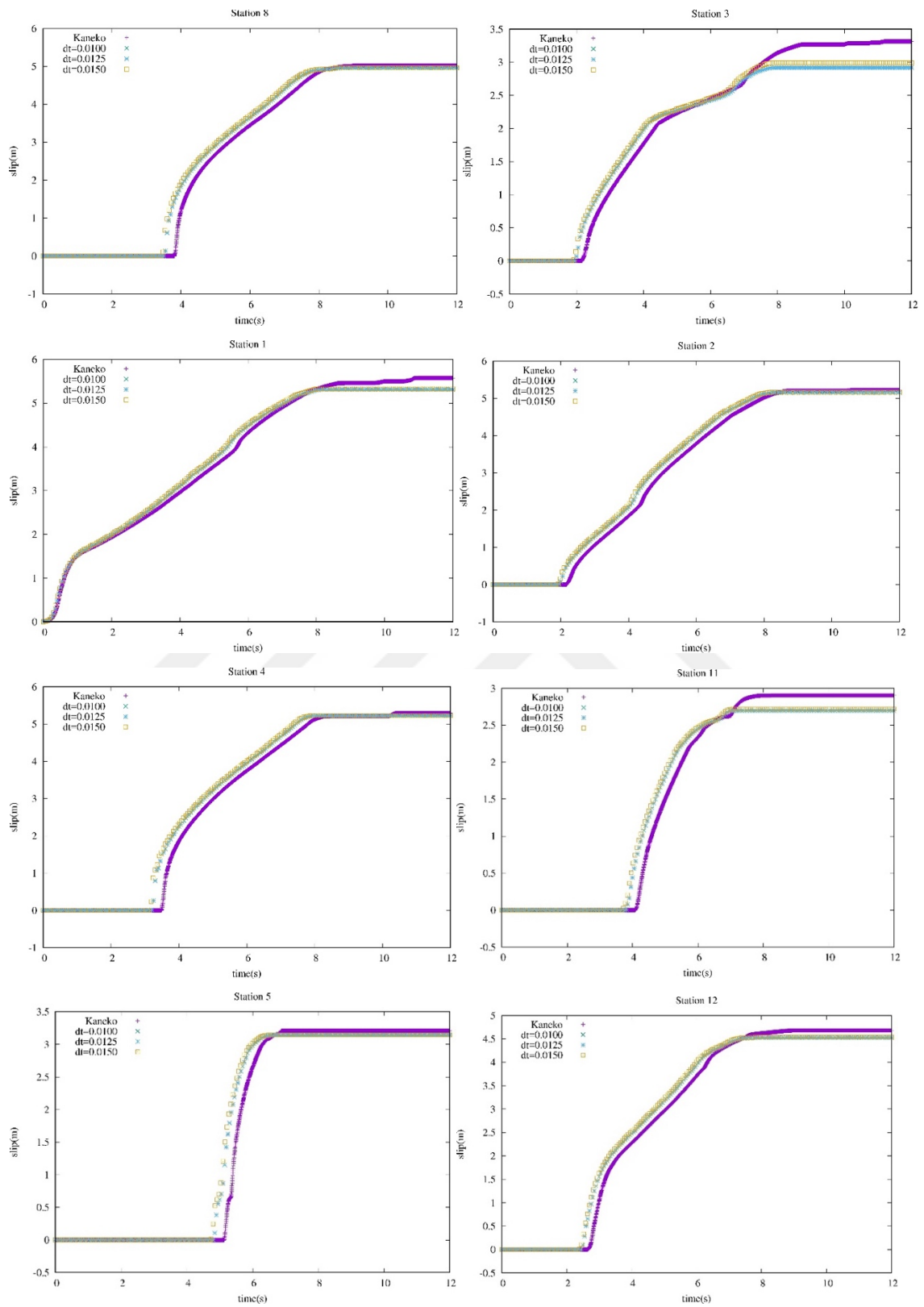
Figure 6.3. Slip-Time Graphics at observation points on the fault surface. Green color is for dt=0.01s, blue is for 0.0125s, and brown is for 0.015s. Purple color represents results of Kaneko for the same test model.
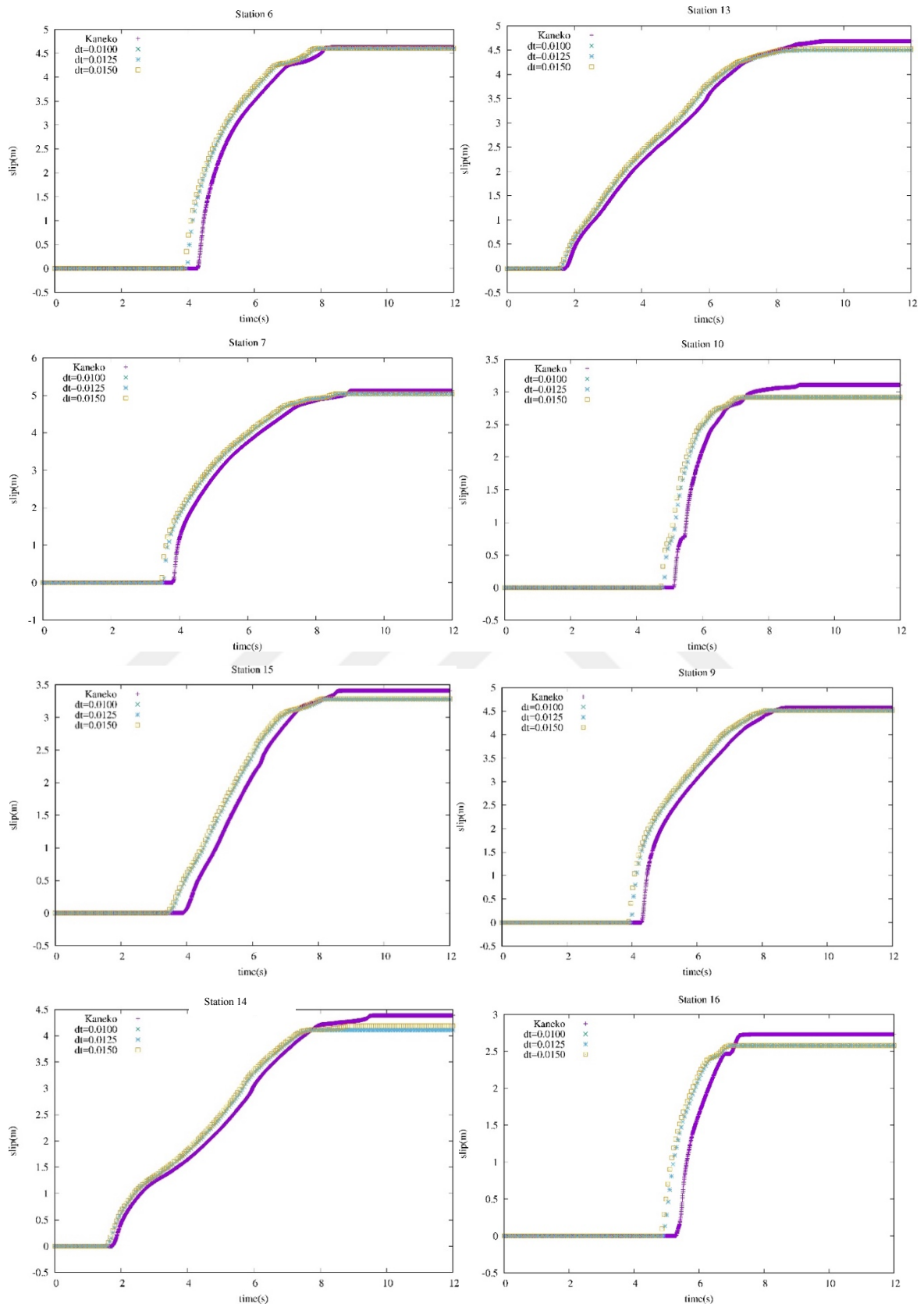
Figure 6.4. Slip-Time Graphics at observation points on the fault surface. Green color is for dt=0.01s, blue is for 0.0125s, and brown is for 0.015s.
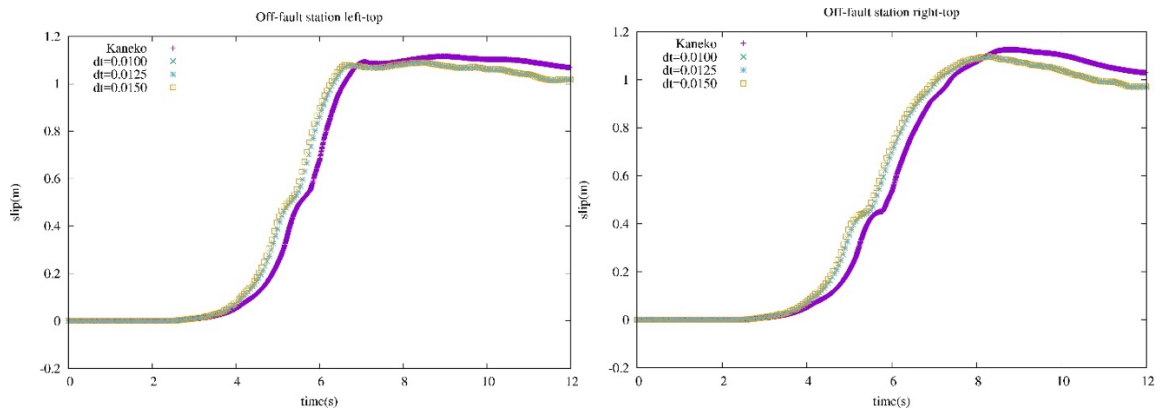
Figure 6.5. Slip-Time Graphics for off-fault observation points at the ground surface. Green color is for dt=0.01s, blue is for 0.0125s, and brown is for 0.015s. Purple color represents results of Kaneko for the same test model.
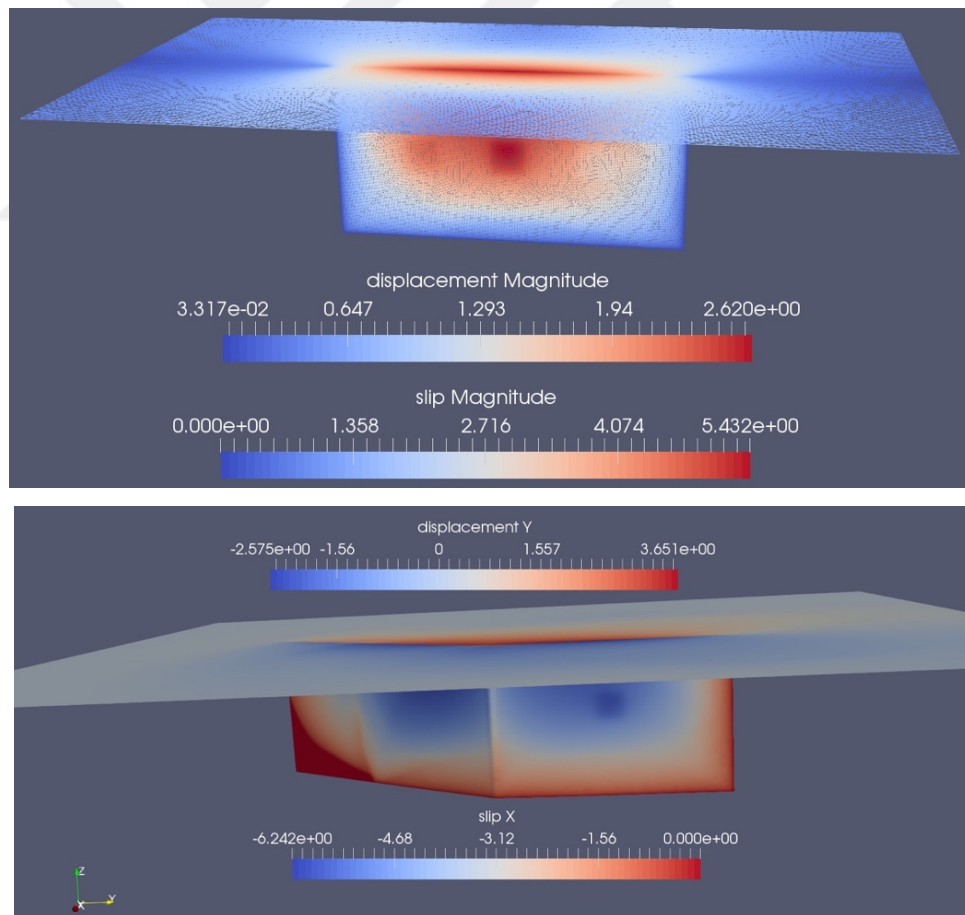
Figure 6.6. Slip and displacement distributions for one (top, SCEC TPV205 case) and two (bottom) segment models.

Comparison of our SCEC TPV205 results for different dt values with the results of Yoshihiro Kaneko, who uses SPECFEM3D for the same test case, are given above. Purple color is for Kaneko's results, while other are results from our tests for different dt values (Fig.6.3).

Due to limitations, slip-rate and tractions results for 200 m grid size are not presented in here. Also, results for 300 m grid size are not given. As a result of time dependent the slip graphics, delay times between our results and Kaneko's results are minimum when dx=300m, but the total slip amounts coincides better when dx=200m. Also, the amount of total slip is increasing with decreasing dt, while delay time is decreasing with increasing dt. Moreover, if dx=300 is selected, dt=0.015s, 0.0175s, 0.02s, 0.0225s gives the best values. On the other hand, since dt=0.0225 does not satisfy the stability condition for the fault model, dt=0.0175 can be used. On the other side, for dx=200m, dt=0.01s should be selected for much complex geometries, as higher values may not coincide with the stability conditions of our complex fault geometry owing to the unstructured meshing (as those values are currently tested).

As a result, the SCEC TPV205 test case was appropriately applied and a two segments model is also simulated before moving on to more complex geometry of MMF. This two segments model include the most complex part of the MMF. Namely, Prince's Island and İzmit segments are modelled. On the other hand, the dip angle is taken 90° for both segments (Fig. 6.4). Therefore, the Main Marmara Fault is started to be modelled after we confirm that PyLith code is used in dynamic rupture simulations in the most correct way.

6.2. The Results of the Dynamic Rupture Simulations along the Main Marmara Fault

In this section, results are interpreted considering our 80 dynamic rupture scenarios for the Sea of Marmara (Table 6.1). Even though many assumptions are done due to unknows about physical and numerical parameters, most of the heterogeneities are well constrained with seismic, geodetic and historical data.

Despite the limitations and uncertainties, remarkably, and abundant number of scenarios, the simulations show that the moment magnitude of a potential earthquake in the MMF can be constrained quite well (Figure 6.7). Among all the scenarios, the largest one is where all locking is homogeneous (C4) and still the moment magnitude of the resulting scenario is < 7.2.

The maximum amount of slip on the fault surface seems to be 0.1 m larger only for homogenously partially locked cases ('…C1-1'; Fig. 5.8, top figure) and its value is the same for heterogeneously partially locked (with different depths of the locking layers) segments (Fig. 5.8, 4 bottom figures; Table 6.1). The amount of ground surface displacement changes only with the location of the initiation point and with the elapsed time since occurrence of the last destructive earthquake in the PI segment. Furthermore, the magnitude of the expected MMF earthquake increases if partially locking segments are homogenously stressed ('…Cx-1'; Fig. 5.8, Fig. 5.9 and Fig. 5.10) or locked layers are continuously run along a whole segment at shallower depths ('…Cx-2', '…Cx-3' and '…Cx-4'; Fig. 5.8, Fig. 5.9 and Fig. 5.10, 4 bottom figures) (Fig. 6.7). Namely, if the number of asperities in the partially locked segment is less, but larger, moment magnitude becomes higher. If the PI segment last ruptured at 1766 earthquake, the change in the size of moment magnitude of the event differs between 0.046 and 0.092 for the homogenously partially locked models ('…Cx-1'; Fig. 5.8, Fig. 5.9 and Fig. 5.10, top figures) and locked layers models at zero depth ('…Cx-2'; Fig. 5.8, Fig. 5.9 and Fig. 5.10, second top figures), respectively. The change in the moment magnitude for deeper locked layers is changing between 0.081 and 0.095. On the other hand, the difference in the magnitude is between 0.1 and 0.135 if the PI fault last ruptured at 1894. As a result, if PI segment last ruptured at 1766, average moment magnitude can be ~ 7.1 ± 0.05, while if it last ruptured at 1894, it can be ~ 7.0 ± 0.08.

Table 6.1. Results from 80 dynamic rupture simulation cases. Names of initiation segments with the number of related cases are given in the first column. Depth dependent locked zones at segments C and D-E are indicated in the second and third columns. Stress drop at initiation segment, maximum slip (in the along strike direction), maximum displacement (in the along strike -X-, fault perpendicular -Y- and up-dip -Z- directions) amounts, peak slip velocity, rupture velocity, seismic moment and moment magnitude values are shown within the rest of the columns, respectively. First 48 cases are for the assumption of PI last ruptured at 1766, while last 32 cases are for PI last ruptured at 1894. The symbol, *, indicates selected master events to plot detailed results.

Case Num	Case Title	C Segment (WH)	D-E Segment (CB) (km)	$\Delta\sigma$ (Mpa)	Slip (m)	V_{peak} (km/s)	V_r (km/s)	DX (m)	DY (m)	DZ (m)	M_0 (Nm)	M_w
1*	KB-in_PI-1766_C1-1	%75 partial lock	%25 partial lock	6.005237	5.0	3.3	*1,931*	2.9	1.6	0.16	63.012503 e+18	7.13295
2	KB-in_PI-1766_C1-2	0-9 km (%75 lock)	0-3 km (%25 lock)	6.005237	5.0	4.2	2,223	2.9	1.6	0.18	50.073033 e+18	7.0664
3	KB-in_PI-1766_C1-3	3-12 km (%75 lock)	3-6 km (%25 lock)	6.005237	5.0	3.3	1,931	2.9	1.5	0.17	46.667688 e+18	7.04601
4	KB-in_PI-1766_C1-4	1-10 km (%75 lock)	4-7 km (%25 lock)	6.005237	5.0	3.3	1,931	2.9	1.5	0.18	47.040644 e+18	7.04832
5	KB-in_PI-1766_C1-5	1-10 km (%75 lock)	7 asperities (%25 lock)	6.005237	4.9	2.9	1,774	2.9	1.5	0.18	45.369098 e+18	7.03784
6	KB-in_PI-1766_C2-1	Tempering (%74 lock)	%25 partial lock	6.005237	5.0	3.3	1,931	2.9	1.6	0.16	62.500231 e+18	7.13059
7	KB-in_PI-1766_C2-2	Tempering (%74 lock)	0-3 km (%25 lock)	6.005237	5.0	4.2	2,223	2.9	1.6	0.80	50.401737 e+18	7.0683
8	KB-in_PI-1766_C2-3	Tempering (%74 lock)	3-6 km (%25 lock)	6.005237	5.0	3.3	1,931	2.9	1.5	0.17	48.552250 e+18	7.05747
9	KB-in_PI-1766_C2-4	Tempering (%74 lock)	4-7 km (%25 lock)	6.005237	5.0	3.3	1,931	2.9	1.5	0.18	48.164970 e+18	7.05515
10*	KB-in_PI-1766_C2-5	Tempering (%74 lock)	7 asperities (%25 lock)	6.005237	4.9	2.9	1,774	2.9	1.5	0.18	46.583612 e+18	7.04549
11	KB-in_PI-1766_C3-1	Tempering (%74 lock)	%50 partial lock	6.005237	5.1	3.3	1,894	2.9	1.6	0.16	71.769222 e+18	7.17063
12	KB-in_PI-1766_C3-2	Tempering (%74 lock)	0-6 km (%50 lock)	6.005237	5.0	5.2	2,482	2.9	1.6	0.15	61.223142 e+18	7.12461
13	KB-in_PI-1766_C3-3	Tempering (%74 lock)	3-9 km (%50 lock)	6.005237	5.0	4.4	2,279	2.9	1.6	0.17	55.045489 e+18	7.09381
14	KB-in_PI-1766_C3-4	Tempering (%74 lock)	4-10 km (%50 lock)	6.005237	5.0	4.4	2,279	2.9	1.6	0.18	54.375708 e+18	7.09027
15	KB-in_PI-1766_C3-5	Tempering (%74 lock)	7 asperities (%50 lock)	6.005237	5.0	3.7	2,069	2.9	1.6	0.15	54.084994 e+18	7.08872
16	KB-in_PI-1766_C4	Fully locked	Fully locked	6.005237	5.5	5.8	2,614	3.2	1.7	0.18	94.105638 e+18	7.24908

Case Num	Case Title	C Segment (WH)	D-E Segment (CB) (km)	$\Delta\sigma$ (Mpa)	Slip (m)	V_{peak} (km/s)	V_r (km/s)	DX (m)	DY (m)	DZ (m)	M_0 (Nm)	M_w
17*	KBeast-in_PI-1766_C1-1	%75 partial lock	%25 partial lock	6.005237	5.0	3.7	2,069	2.8	1.5	0.18	63.533393 e+18	7.13533
18	KBeast-in_PI-1766_C1-2	0-9 km (%75 lock)	0-3 km (%25 lock)	6.005237	5.0	4.5	2,307	2.8	1.5	0.19	50.557237 e+18	7.06919
19	KBeast-in_PI-1766_C1-3	3-12 km (%75 lock)	3-6 km (%25 lock)	6.005237	5.0	3.6	2,036	2.8	1.5	0.19	46.806257 e+18	7.04687
20	KBeast-in_PI-1766_C1-4	1-10 km (%75 lock)	4-7 km (%25 lock)	6.005237	5.0	3.7	2,069	2.8	1.5	0.20	47.504093 e+18	7.05115
21	KBeast-in_PI-1766_C1-5	1-10 km (%75 lock)	7 asperities (%25 lock)	6.005237	5.0	3.7	2,069	2.8	1.5	0.19	45.682577 e+18	7.03983
22	KBeast-in_PI-1766_C2-1	Tempering (%74 lock)	%25 partial lock	6.005237	5.0	3.7	2,069	2.8	1.5	0.18	63.046283 e+18	7.13311
23	KBeast-in_PI-1766_C2-2	Tempering (%74 lock)	0-3 km (%25 lock)	6.005237	5.0	4.5	2,307	2.8	1.5	0.19	50.877865 e+18	7.07102
24	KBeast-in_PI-1766_C2-3	Tempering (%74 lock)	3-6 km (%25 lock)	6.005237	5.0	3.7	2,069	2.8	1.5	0.19	48.963078 e+18	7.05991
25	KBeast-in_PI-1766_C2-4	Tempering (%74 lock)	4-7 km (%25 lock)	6.005237	5.0	3.7	2,069	2.8	1.5	0.20	48.628065 e+18	7.05792
26*	KBeast-in_PI-1766_C2-5	Tempering (%74 lock)	7 asperities (%25 lock)	6.005237	5.0	3.6	2,036	2.8	1.5	0.19	46.926452 e+18	7.04761
27	KBeast-in_PI-1766_C3-1	Tempering (%74 lock)	%50 partial lock	6.005237	5.0	3.7	2,069	2.8	1.5	0.18	72.755929 e+18	7.17458
28	KBeast-in_PI-1766_C3-2	Tempering (%74 lock)	0-6 km (%50 lock)	6.005237	5.0	5.4	2,527	2.8	1.5	0.17	61.961329 e+18	7.12808
29	KBeast-in_PI-1766_C3-3	Tempering (%74 lock)	3-9 km (%50 lock)	6.005237	5.0	4.8	2,385	2.8	1.5	0.17	55.552402 e+18	7.09647
30	KBeast-in_PI-1766_C3-4	Tempering (%74 lock)	4-10 km (%50 lock)	6.005237	5.0	4.6	2,333	2.8	1.5	0.19	54.818796 e+18	7.09262
31	KBeast-in_PI-1766_C3-5	Tempering (%74 lock)	7 asperities (%50 lock)	6.005237	5.0	4.0	2,164	2.8	1.5	0.17	54.511070 e+18	7.09099
32	KBeast-in_PI-1766_C4	Fully locked	Fully locked	6.005237	5.5	6.1	2,675	3.2	1.6	0.2	95.992288 e+18	7.25482
33	PI-in_PI-1766_C1-1	%75 partial lock	%25 partial lock	3.478313	5.1	4.0	2,164	2.7	1.4	0.16	60.763643 e+18	7.12243
34	PI-in_PI-1766_C1-2	0-9 km (%75 lock)	0-3 km (%25 lock)	3.478313	5.0	4.8	2,385	2.7	1.4	0.14	48.144568 e+18	7.05503
35	PI-in_PI-1766_C1-3	3-12 km (%75 lock)	3-6 km (%25 lock)	3.478313	5.0	4.0	2,164	2.7	1.4	0.17	44.790069 e+18	7.03412
36	PI-in_PI-1766_C1-4	1-10 km (%75 lock)	4-7 km (%25 lock)	3.478313	5.0	4.0	2,164	2.7	1.4	0.18	45.098982 e+18	7.03611
37	PI-in_PI-1766_C1-5	1-10 km (%75 lock)	7 asperities (%25 lock)	3.478313	5.0	4.0	2,164	2.7	1.4	0.18	43.605465 e+18	7.02636
38	PI-in_PI-1766_C2-1	Tempering (%74 lock)	%25 partial lock	3.478313	5.1	4.0	2,164	2.7	1.4	0.16	60.098583 e+18	7.11924
39	PI-in_PI-1766_C2-2	Tempering (%74 lock)	0-3 km (%25 lock)	3.478313	5.0	4.7	2,359	2.7	1.4	0.18	48.477966 e+18	7.05703
40	PI-in_PI-1766_C2-3	Tempering (%74 lock)	3-6 km (%25 lock)	3.478313	5.0	4.1	2,194	2.7	1.4	0.17	46.646953 e+18	7.04588
41	PI-in_PI-1766_C2-4	Tempering (%74 lock)	4-7 km (%25 lock)	3.478313	5.0	4.0	2,164	2.7	1.4	0.18	46.228261 e+18	7.04327

Case Num	Case Title	C Segment (WH)	D-E Segment (CB) (km)	$\Delta\sigma$ (Mpa)	Slip (m)	V_{peak} (km/s)	V_r (km/s)	DX (m)	DY (m)	DZ (m)	M_0 (Nm)	M_w
42	PI-in_PI-1766_C2-5	Tempering (%74 lock)	7 asperities (%25 lock)	3.478313	5.0	4.1	2,194	2.7	1.4	0.18	44.825488 e+18	7.03435
43	PI-in_PI-1766_C3-1	Tempering (%74 lock)	%50 partial lock	3.478313	5.1	4.0	2,164	2.7	1.4	0.18	69.131749 e+18	7.15979
44	PI-in_PI-1766_C3-2	Tempering (%74 lock)	0-6 km (%50 lock)	3.478313	5.1	5.6	2,571	2.7	1.4	0.16	59.046892 e+18	7.11413
45	PI-in_PI-1766_C3-3	Tempering (%74 lock)	3-9 km (%50 lock)	3.478313	5.0	5.0	2,434	2.7	1.4	0.17	52.944861 e+18	7.08255
46	PI-in_PI-1766_C3-4	Tempering (%74 lock)	4-10 km (%50 lock)	3.478313	5.0	4.9	2,410	2.7	1.4	0.18	52.266801 e+18	7.07882
47	PI-in_PI-1766_C3-5	Tempering (%74 lock)	7 asperities (%50 lock)	3.478313	5.0	4.3	2,251	2.7	1.4	0.16	52.198503 e+18	7.07844
48	PI-in_PI-1766_C4	Fully locked	Fully locked	3.478313	5.4	6.0	2,655	3.1	1.4	0.22	90.796772 e+18	7.23871
49	KB-in_PI-1894_C1-1	%75 partial lock	%25 partial lock	6.005237	5.0	3.3	1,931	2.7	1.4	0.15	45.475754 e+18	7.03852
50	KB-in_PI-1894_C1-2	0-9 km locked	0-3 km (%25 lock)	6.005237	4.9	4.2	2,223	2.7	1.4	0.17	33.030498 e+18	6.94594
51	KB-in_PI-1894_C1-3	3-12 km (%75 lock)	3-6 km (%25 lock)	6.005237	4.9	3.3	1,931	2.7	1.4	0.17	29.611102 e+18	6.9143
52	KB-in_PI-1894_C1-4	1-10 km (%75 lock)	4-7 km (%25 lock)	6.005237	4.9	3.3	1,931	2.7	1.4	0.18	30.022893 e+18	6.9183
53	KB-in_PI-1894_C1-5	1-10 km (%75 lock)	7 asperities (%25 lock)	6.005237	4.9	2.9	1,774	2.7	1.4	0.17	28.455183 e+18	6.90277
54	KB-in_PI-1894_C2-1	Tempering (%74 lock)	%25 partial lock	6.005237	4.7	3.3	1,931	2.4	0.75	0.17	44.982961 e+18	7.03537
55	KB-in_PI-1894_C2-2	Tempering (%74 lock)	0-3 km (%25 lock)	6.005237	4.7	4.2	2,223	2.4	0.72	0.16	33.360937 e+18	6.94883
56	KB-in_PI-1894_C2-3	Tempering (%74 lock)	3-6 km (%25 lock)	6.005237	4.7	3.2	1,894	2.4	0.71	0.16	31.532398 e+18	6.9325
57	KB-in_PI-1894_C2-4	Tempering (%74 lock)	4-7 km (%25 lock)	6.005237	4.7	3.3	1,931	2.4	0.71	0.16	31.164229 e+18	6.9291
58	KB-in_PI-1894_C2-5	Tempering (%74 lock)	7 asperities (%25 lock)	6.005237	4.6	2.8	1,732	2.3	0.70	0.17	29.670786 e+18	6.91489
59	KB-in_PI-1894_C3-1	Tempering (%74 lock)	%50 partial lock	6.005237	4.8	3.3	1,931	2.5	0.78	0.18	54.003593 e+18	7.08828
60	KB-in_PI-1894_C3-2	Tempering (%74 lock)	0-6 km (%50 lock)	6.005237	4.7	5.2	2,482	2.4	0.75	0.17	43.902293 e+18	7.02832
61	KB-in_PI-1894_C3-3	Tempering (%74 lock)	3-9 km (%50 lock)	6.005237	4.7	4.4	2,279	2.4	0.73	0.16	37.885387 e+18	6.98565
62	KB-in_PI-1894_C3-4	Tempering (%74 lock)	4-10 km (%50 lock)	6.005237	4.7	4.4	2,279	2.4	0.73	0.16	37.265834 e+18	6.98087
63	KB-in_PI-1894_C3-5	Tempering (%74 lock)	7 asperities (%50 lock)	6.005237	4.7	3.7	2,069	2.4	0.73	0.17	36.958699 e+18	6.97848
64	KB-in_PI-1894_C4	Fully locked	Fully locked	6.005237	4.9	5.8	2,613	2.7	0.83	0.22	75.925391 e+18	7.18692

Case Num	Case Title	C Segment (WH)	D-E Segment (CB) (km)	$\Delta\sigma$ (Mpa)	Slip (m)	V_{peak} (km/s)	V_r (km/s)	DX (m)	DY (m)	DZ (m)	M_0 (Nm)	M_w
65	KBeast-in_PI-1894_C1-1	%75 partial lock	%25 partial lock	6.005237	4.7	3.7	2,069	2.4	0.70	0.16	60.072608 e+18	7.11912
66	KBeast-in_PI-1894_C1-2	0-9 km locked	0-3 km (%25 lock)	6.005237	4.6	4.6	2,333	2.3	0.66	0.16	47.132441 e+18	7.04888
67	KBeast-in_PI-1894_C1-3	3-12 km (%75 lock)	3-6 km (%25 lock)	6.005237	4.6	3.6	2,036	2.3	0.66	0.16	43.405006 e+18	7.02503
68	KBeast-in_PI-1894_C1-4	1-10 km (%75 lock)	4-7 km (%25 lock)	6.005237	4.6	3.6	2,036	2.3	0.66	0.17	44.093949 e+18	7.02959
69	KBeast-in_PI-1894_C1-5	1-10 km (%75 lock)	7 asperities (%25 lock)	6.005237	4.6	3.6	2,036	2.3	0.65	0.17	42.290593 e+18	7.0175
70	KBeast-in_PI-1894_C2-1	Tempering (%74 lock)	%25 partial lock	6.005237	4.7	3.7	2,069	2.4	0.70	0.16	45.803729 e+18	7.0406
71	KBeast-in_PI-1894_C2-2	Tempering (%74 lock)	0-3 km (%25 lock)	6.005237	4.6	4.6	2,333	2.3	0.66	0.16	33.880718 e+18	6.9533
72	KBeast-in_PI-1894_C2-3	Tempering (%74 lock)	3-6 km (%25 lock)	6.005237	4.6	3.7	2,069	2.3	0.66	0.16	31.984057 e+18	6.93662
73	KBeast-in_PI-1894_C2-4	Tempering (%74 lock)	4-7 km (%25 lock)	6.005237	4.6	3.6	2,036	2.3	0.66	0.17	31.671909 e+18	6.93378
74	KBeast-in_PI-1894_C2-5	Tempering (%74 lock)	7 asperities (%25 lock)	6.005237	4.6	3.6	2,036	2.3	0.65	0.17	30.092524 e+18	6.91897
75	KBeast-in_PI-1894_C3-1	Tempering (%74 lock)	%50 partial lock	6.005237	4.7	3.6	2,036	2.5	0.72	0.17	55.339250 e+18	7.09536
76	KBeast-in_PI-1894_C3-2	Tempering (%74 lock)	0-6 km (%50 lock)	6.005237	4.7	5.5	2,550	2.4	0.69	0.16	44.764180 e+18	7.03395
77	KBeast-in_PI-1894_C3-3	Tempering (%74 lock)	3-9 km (%50 lock)	6.005237	4.6	4.8	2,385	2.4	0.68	0.16	38.452490 e+18	6.98995
78	KBeast-in_PI-1894_C3-4	Tempering (%74 lock)	4-10 km (%50 lock)	6.005237	4.6	4.6	2,333	2.4	0.68	0.16	37.748127 e+18	6.9846
79	KBeast-in_PI-1894_C3-5	Tempering (%74 lock)	7 asperities (%50 lock)	6.005237	4.6	4.0	2,164	2.4	0.68	0.15	37.452770 e+18	6.98232
80	KBeast-in_PI-1894_C4	Fully locked	Fully locked	6.005237	5.3	6.2	2,695	3.0	077	0.2	78.069382 e+18	7.19499
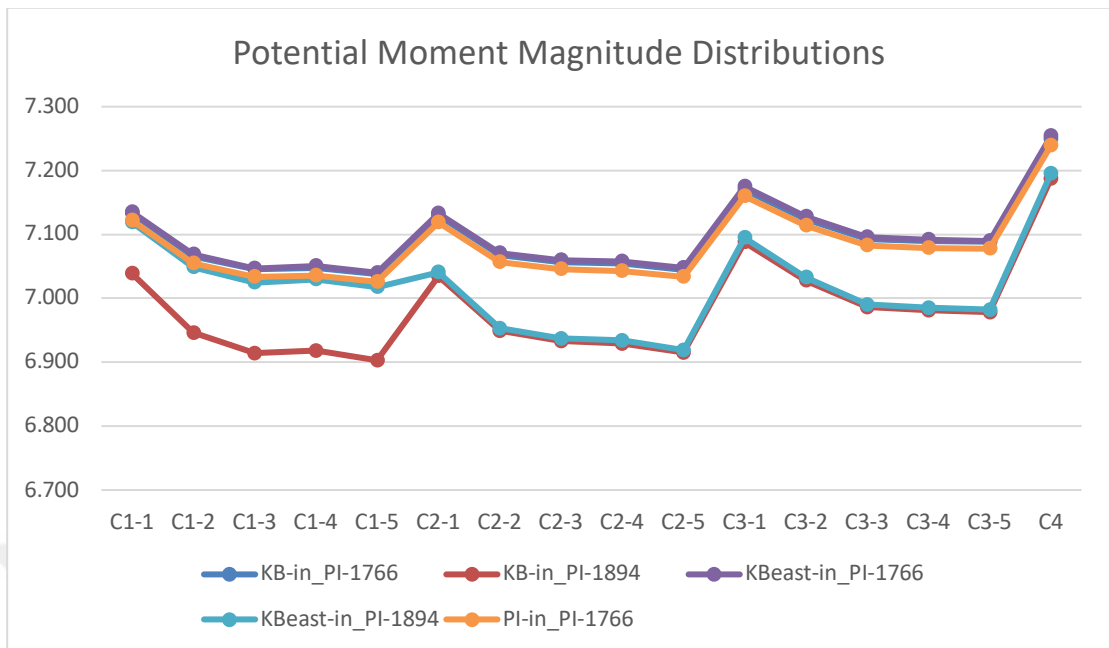
Figure 6.7. Moment magnitude results for selected 80 simulations. KB-in_PI-1766 (dark blue) totally overlaps with KBeast-in_PI-1766 (purple), so it is not clearly visible. Horizontal axis is the case name.
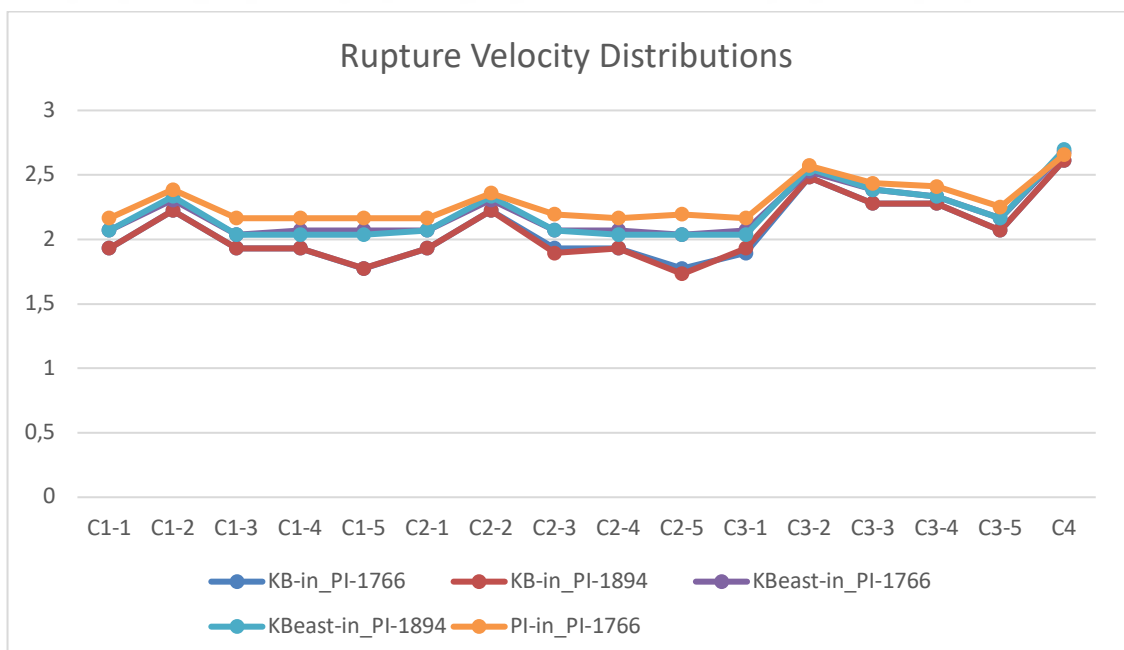
Figure 6.8. Rupture velocity distributions for selected 80 simulations. KB-in_PI-1766 (dark blue) overlaps with KB-in_PI-1894 (red). Also, KBeast-in_PI1766 (purple) matches with KBeast-in_PI-1894 (light blue). Rupture velocity is in meter/second.

As a result, simulations C1-1, C2-1 and C3-1 (Fig. 5.8, Fig. 5.9 and Fig. 5.10, top figures) where partially creep is homogeneous and no asperity is embedded cause larger earthquake magnitudes among all partially locked models. Cases C2-y and C3-y (Fig. 5.9 and Fig. 5.10, all figures) for PI rupture at 1894 present relatively lower magnitudes for central KB and eastern KB initiations. It is also valid for the case C1-y (Fig. 5.8), for central KB initiation, but not for eastern KB initiation (Fig 6.7).
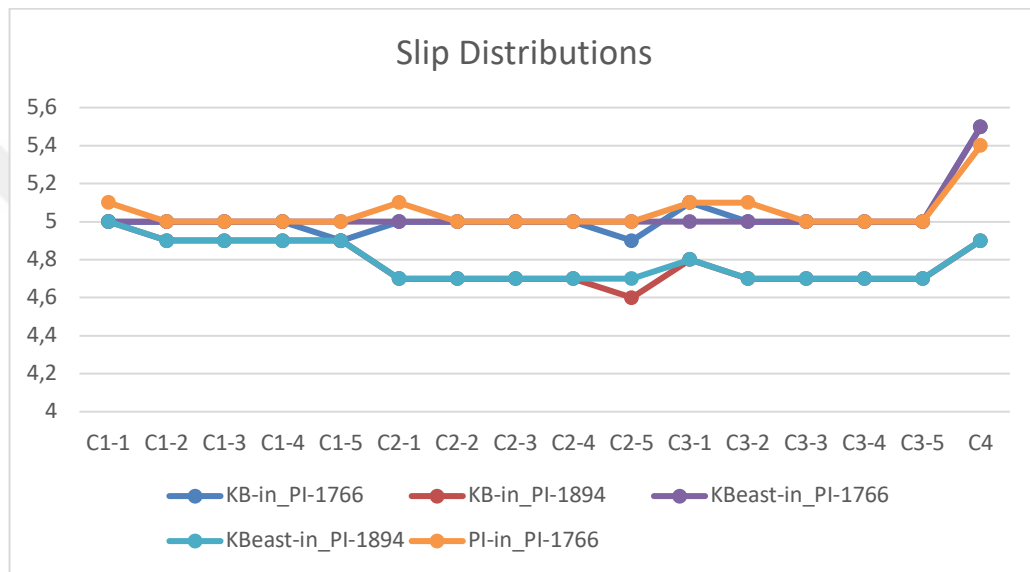
Figure 6.9. Slip distributions for selected 80 simulations. Slip is in meters.
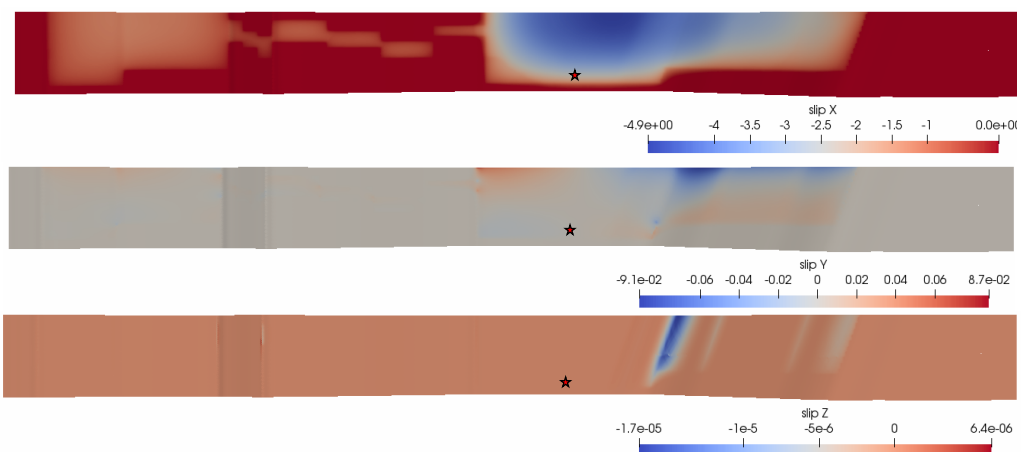
Figure 6.10. Final slip distributions in the along strike (top), fault perpendicular (normal to the fault surface) (middle) and up-dip (bottom) directions for case 10 (KB-in_PI-1766_C2-5) (Table 6.1). PI segment last ruptured at 1766 earthquake. Units are in meters. Red stars are initiation points.

Figure 6.11. Final slip distributions in the along strike (top), fault perpendicular (normal to the fault surface) (middle) and up-dip (bottom) directions for case 58 (KB-in_PI-1894_C2-5) (Table 6.1). PI segment last ruptured at 1894 earthquake. Units are in meters.
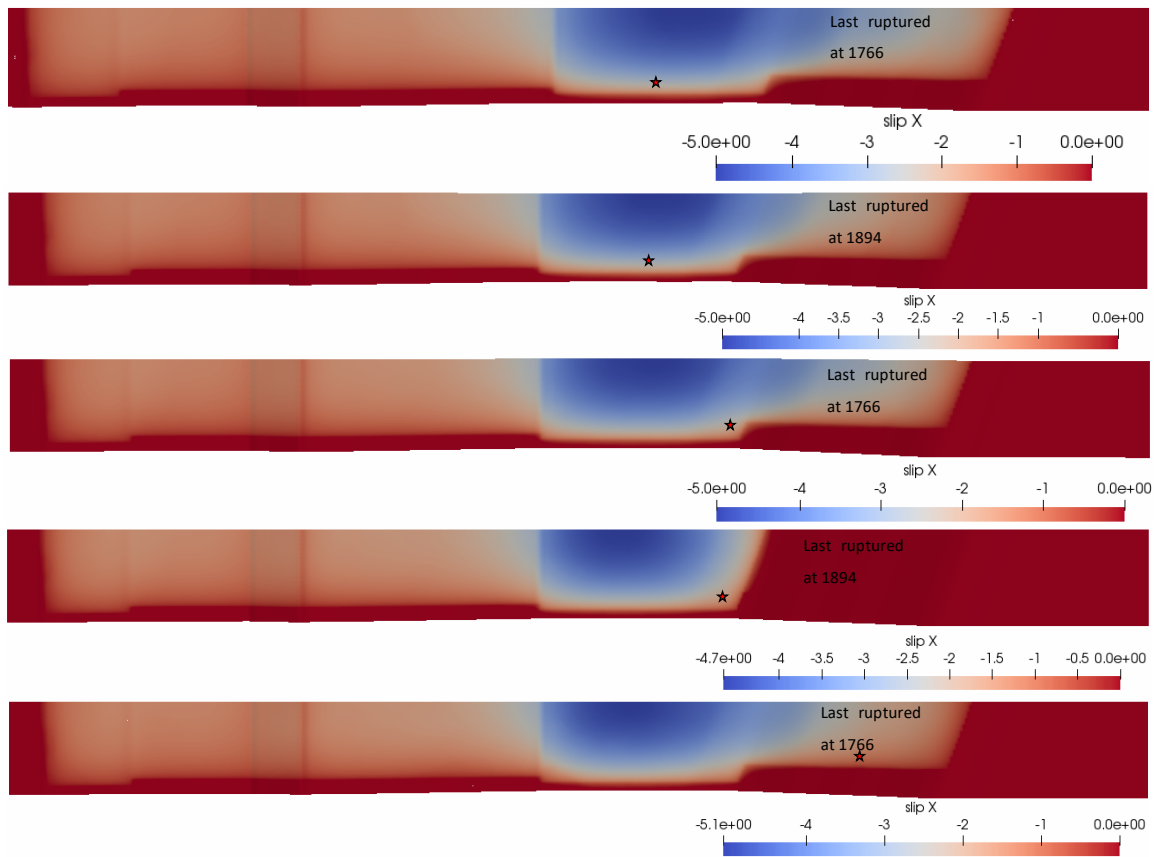
Figure 6.12. Final slip distributions for cases C1-1. Cases 1, 49, 17, 65 and 33 are shown, respectively (Table 6.1). Red stars are initiation points.

Furthermore, in terms of selected strike angle (312°) for the maximum principal compressive stress axis in the Eastern Ganos Region, rupture does not enter into the segment A, as it was already ruptured during 1912 earthquake (Fig. 6.10, 6.11 and 6.12). Nevertheless, when the strike angle of the maximum principle compressive stress axis is rotated from 1° to 3° in the clockwise direction, the segment A is broken again, 108 years after the 1912 event like segment B, showing the importance of 1° rotation of stress axes.

Contrary to super-shear rupture velocity findings of previous studies (Aochi and Ulrich, 2015; Oglesby and Mai, 2012), sub-shear rupture velocities are derived in this thesis study. The maximum obtained value of rupture velocity is 2.55 m/s, ignoring fully locked cases (Table 6.1). Sub-shear rupture velocities are valid for fully locked cases, as well. In addition, relatively larger rupture velocities are observed for scenarios Cx-2 where locked layers of partially creeping segments are located at zero depth although physically we don't expect such shallow locking depths (Fig. 6.8). Briefly, rupture velocity is 2.16 ± 0.19 km/s for 1766 rupture at PI segment, and 2.10 ± 0.20 km/s for 1894 rupture at PI segment. The reason for sub-shear rupture velocities and relatively lower magnitude values compared to previous studies (Aochi and Ulrich, 2015; Oglesby and Mai, 2012) is that we model a realistic (shallower) fault model and consider partially creeping behavior of the WH and CMB segments.

As a result of many iterations, some important changes in the data arrival times and amplitudes of the waveforms are possible if different static friction coefficients are used in partially creeping segments, especially for the rupture initiations at the KB segment. Additionally, it is found that the use of different friction coefficients effects the termination of the rupture. Therefore, fixed static and dynamic friction coefficients are used in our scenarios.
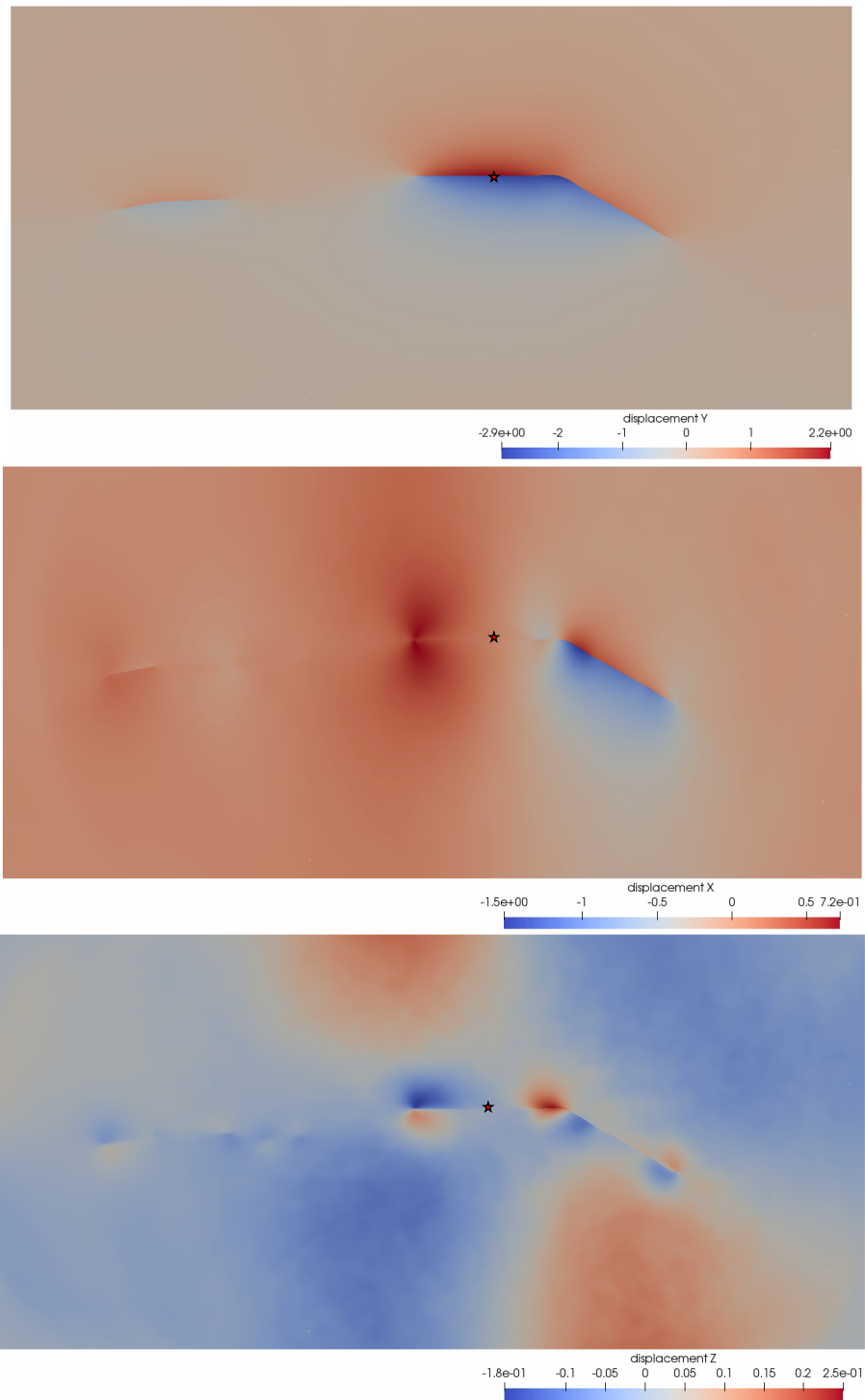
Figure 6.13. Final ground surface displacements in the along strike (top), fault perpendicular (middle) and up-dip (bottom) directions for case 10 (KB-in_PI-1766_C2-5) (Table 6.1). PI segment last ruptured at 1766 earthquake. Units are in meters.
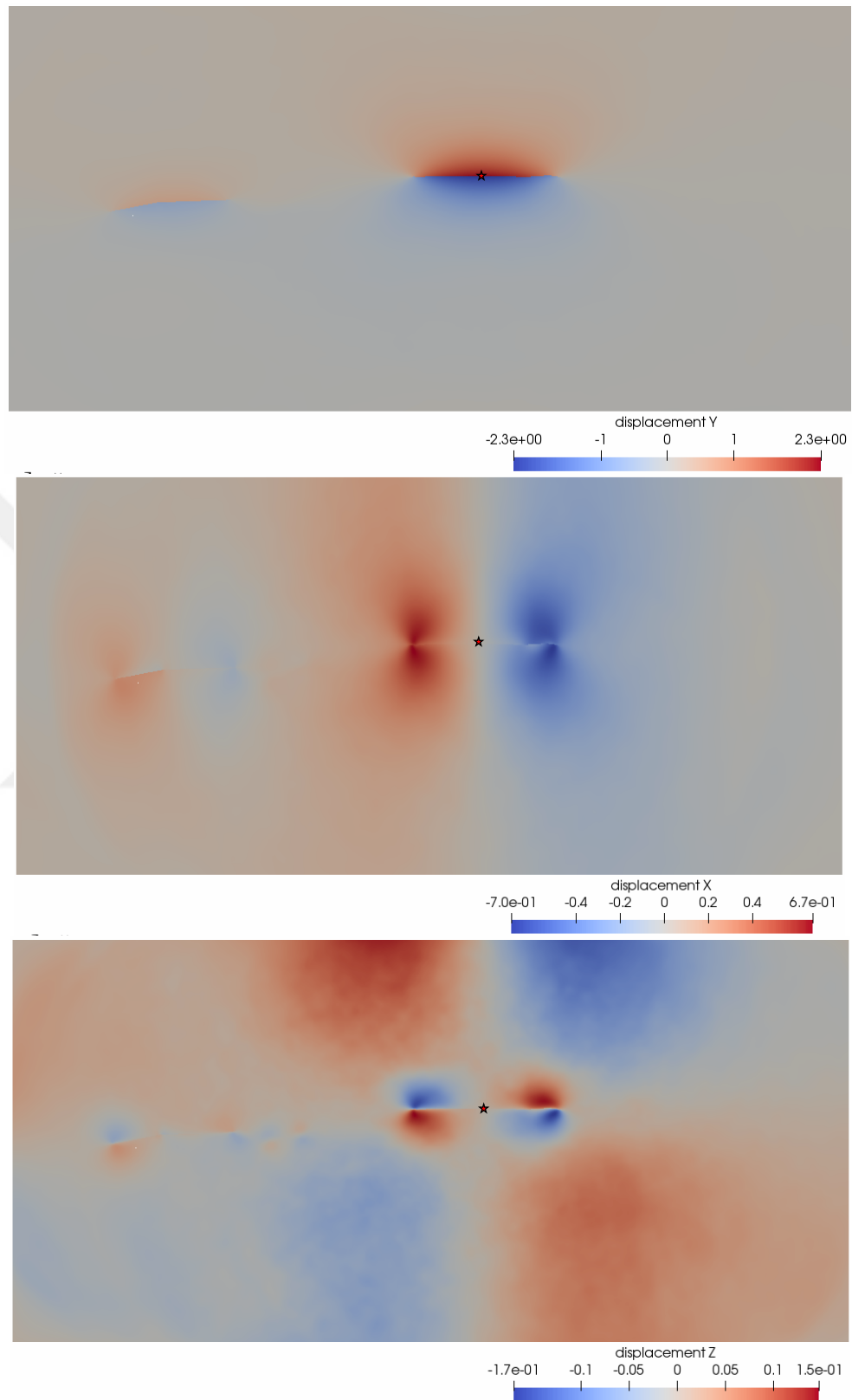
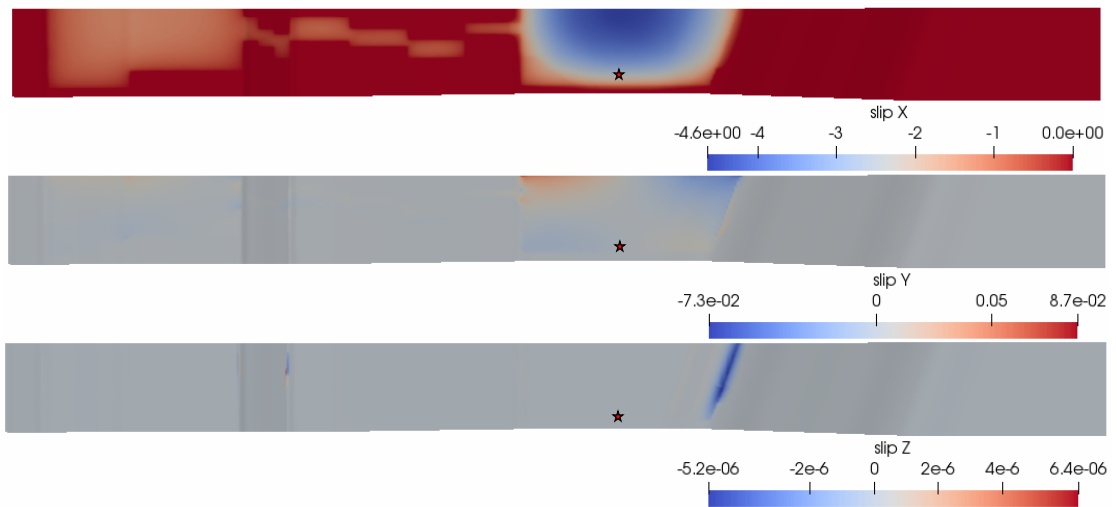Figure 6.14. Final ground surface displacements in the along strike (top), fault perpendicular (middle) and up-dip (bottom) directions for case 58 (KB-in_PI-1894_C2-5) (Table 6.1). PI segment last ruptured at 1894 earthquake. Units are in meters.

When fully locked fault models are not considered, the largest slip and displacement are observed only at KB segment and the second largest slip and displacement are found out at PI segment (Fig. 6.12, Fig. 6.13 and Fig. 6.14). This evidence does not depend on 1984 or 1766 rupture cases for PI segment, as an indicator of the importance of the geometry. Slip and displacement at segments B, C, D and E (Fig. 5.7) are almost less than half comparing slip and displacement at segments F (KB) and G (PI) (Fig. 6.10, 6.11, 6.12, 6.13 and 6.14). Furthermore, largest slip in the along strike direction is changing between 4.9 m and 5.1 m (~5.0 m) for the 1766 rupture at PI segment and it is changing between 4.6 m and 5.0 m for the 1894 rupture at PI segment. Especially for the 1894 rupture, maximum slip amounts are smaller in eastern KB initiation cases than central KB initiation cases. As a result, slip is 5.0 ± 0.04 m for 1766 rupture at PI segment and 4.7 ± 0.11 m for 1894 rupture at PI segment.

Moreover, slip in the fault perpendicular direction (normal to the fault surface) is less than 10 cm or equals zero considering all scenarios, and slip in the up-dip direction is zero for all scenarios. No tsunami is expected owing to up-dip fault slip, so it may be generated by landslides. Moreover, larger maximum slip amounts are observed at scenarios Cx-1 where partially creeping areas don't have asperities (Fig. 6.9).

Along strike displacements are ~0.1 m smaller in the case of eastern KB initiation comparing with central KB initiation. Fault perpendicular displacements are also smaller for eastern KB initiation, while it is not the case for the displacements in the up-dip direction (Table 6.1, dz). Furthermore, ~0.6 m along strike ground surface displacement decrease is realized if PI last ruptured at 1894 (Fig. 6.13 and 6.14, top maps). Displacement in the fault normal direction also almost half (Fig. 6.13 and 6.14, middle figures). In addition, no difference is found in the displacements of up-dip direction, as it is expected to be zero for strike-slip faults.
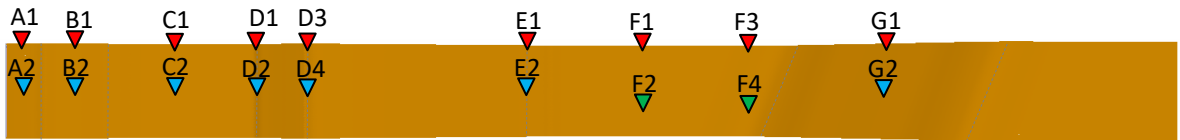
Figure 6.15. Selected observation points on the fault surface. Red triangles are located at zero depth. Blue triangles are located at 7.5 km depth while green triangles are at 10.0 km depth.
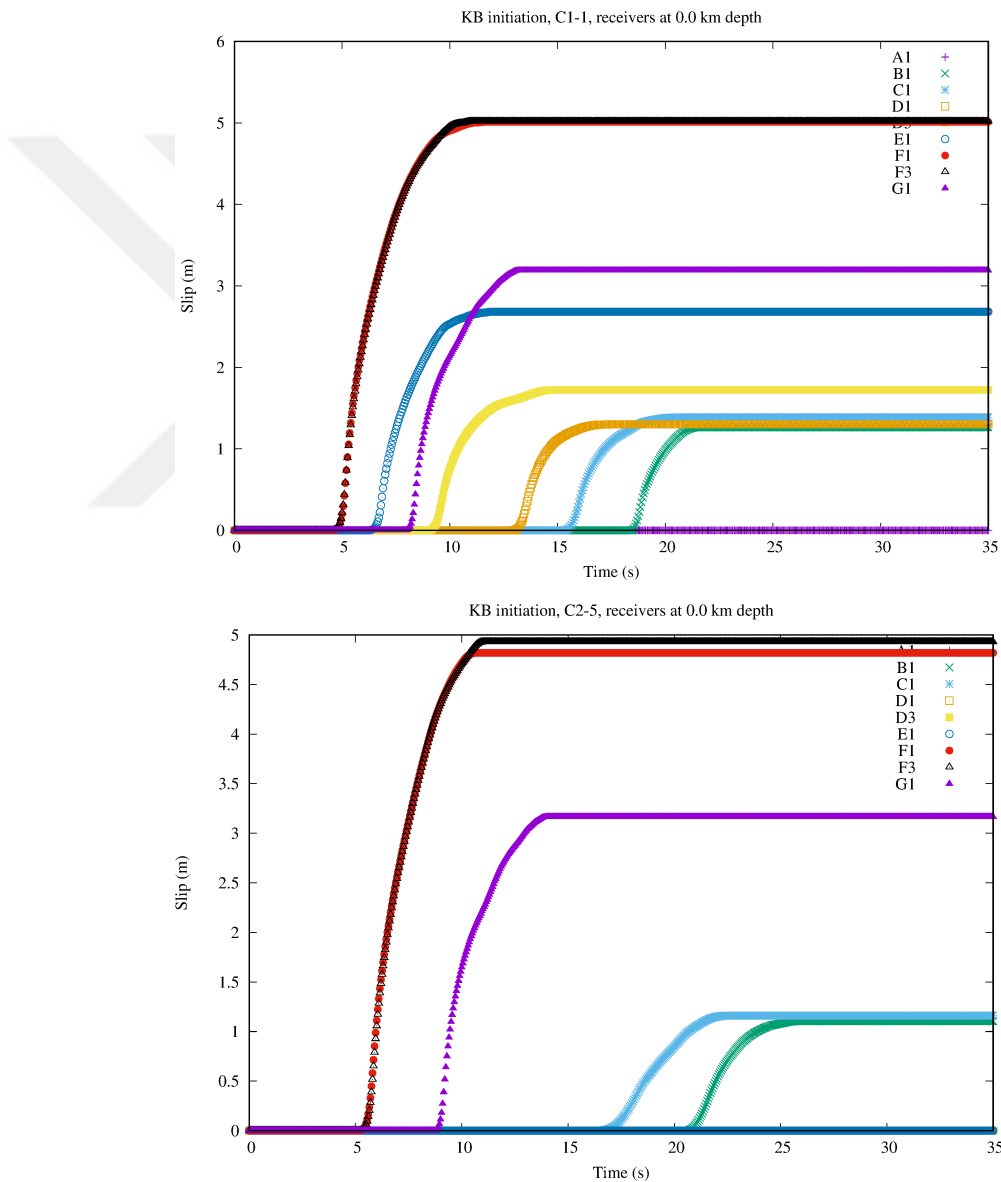
Figure 6.16. Temporal slip change graphics for cases 'KB-in_PI-1766_C1-1' (top) and 'KB-in_PI-1766_C2-5' (bottom) (Table 6.1). Receivers are located at zero depth. Receiver locations are shown in Fig.6.15.
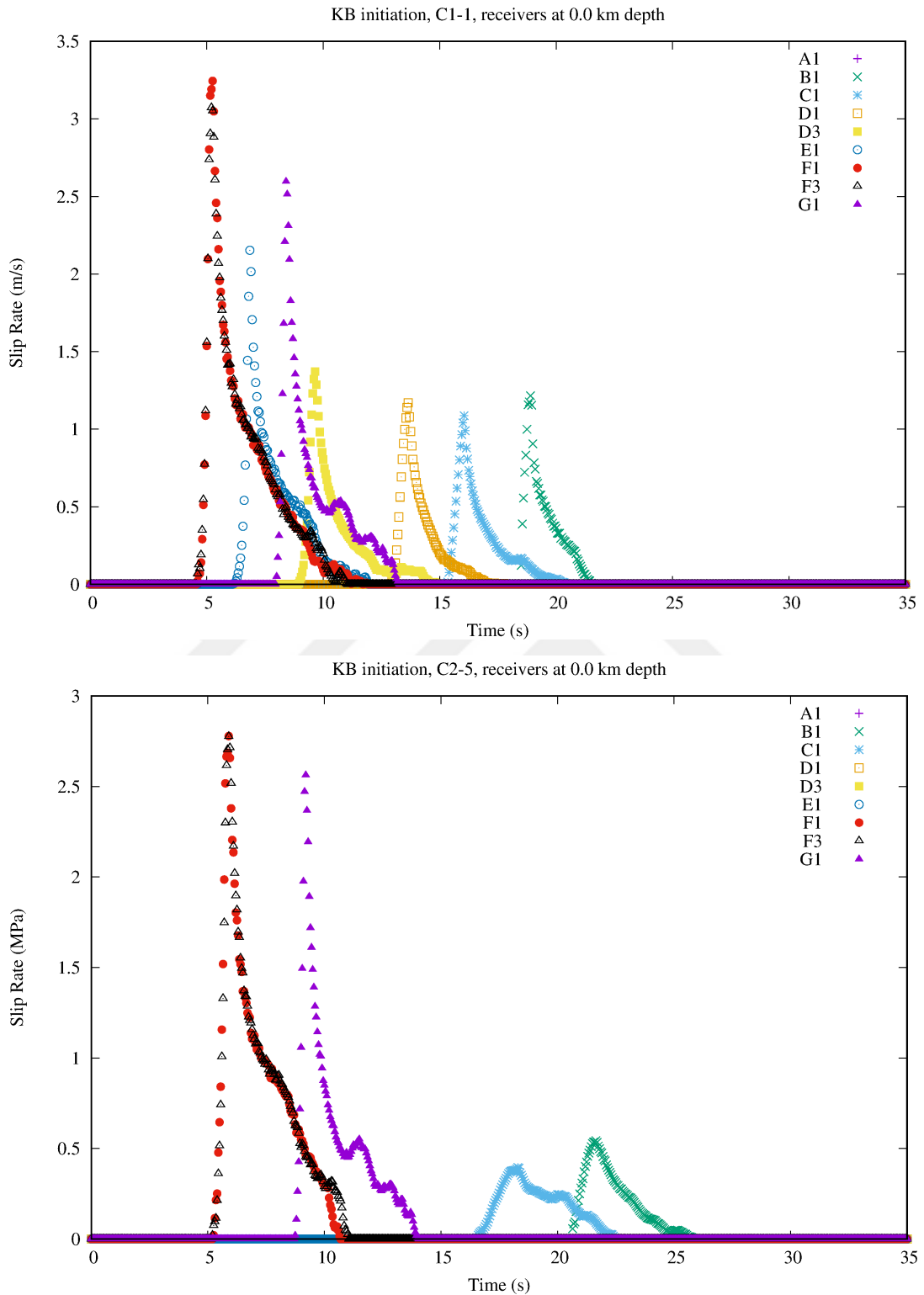
Figure 6.17. Temporal slip-rate graphics for cases 'KB-in_PI-1766_C1-1' (top) and 'KB-in_PI-1766_C2-5' (bottom) (Table 6.1). Receivers are located at zero depth. Receiver locations are shown in Fig.6.15.
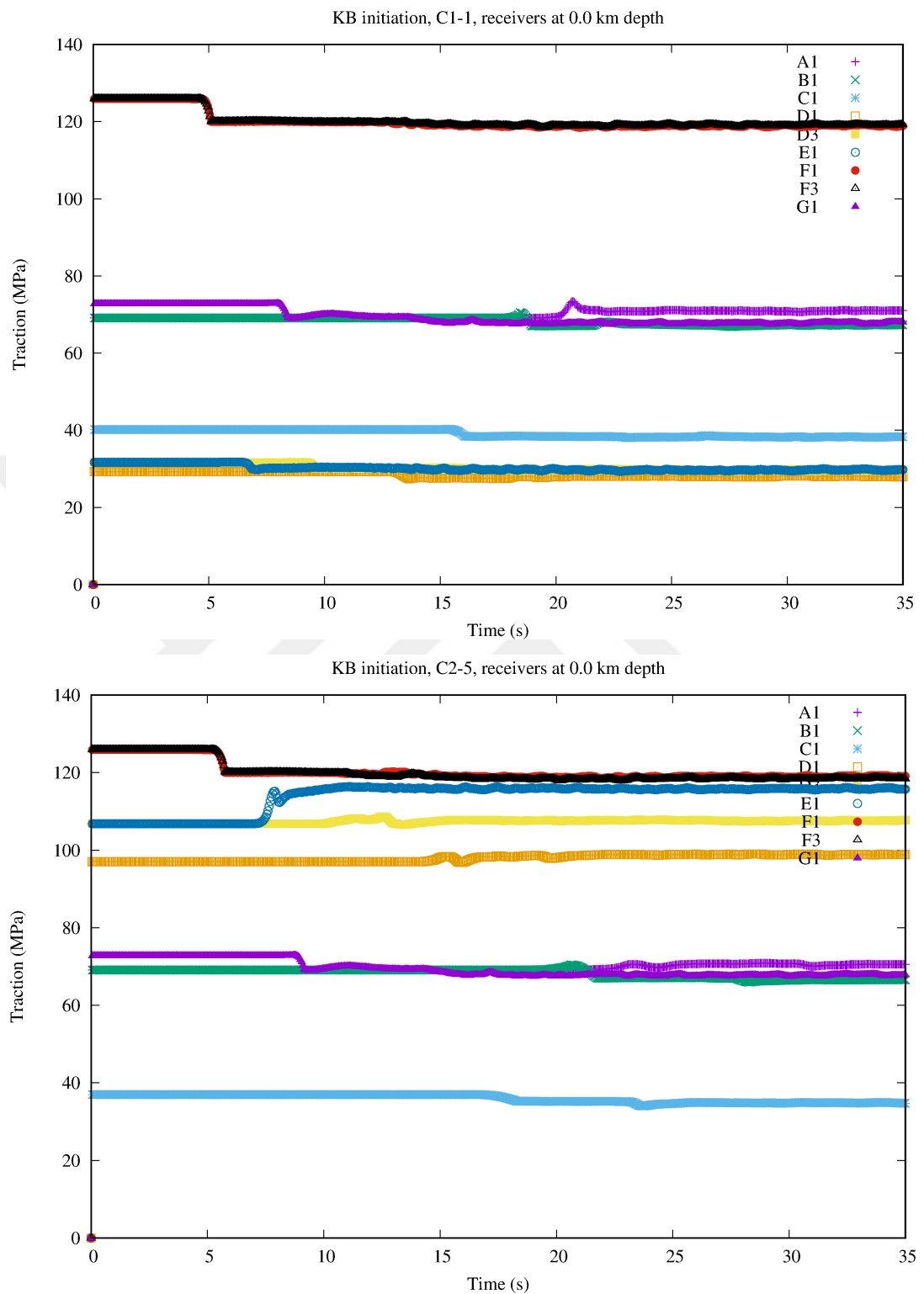
Figure 6.18. Temporal traction change graphics for cases 'KB-in_PI-1766_C1-1' (top) and 'KB-in_PI-1766_C2-5' (bottom) (Table 6.1). Receivers are located at zero depth. Receiver locations are shown in Fig.6.15.
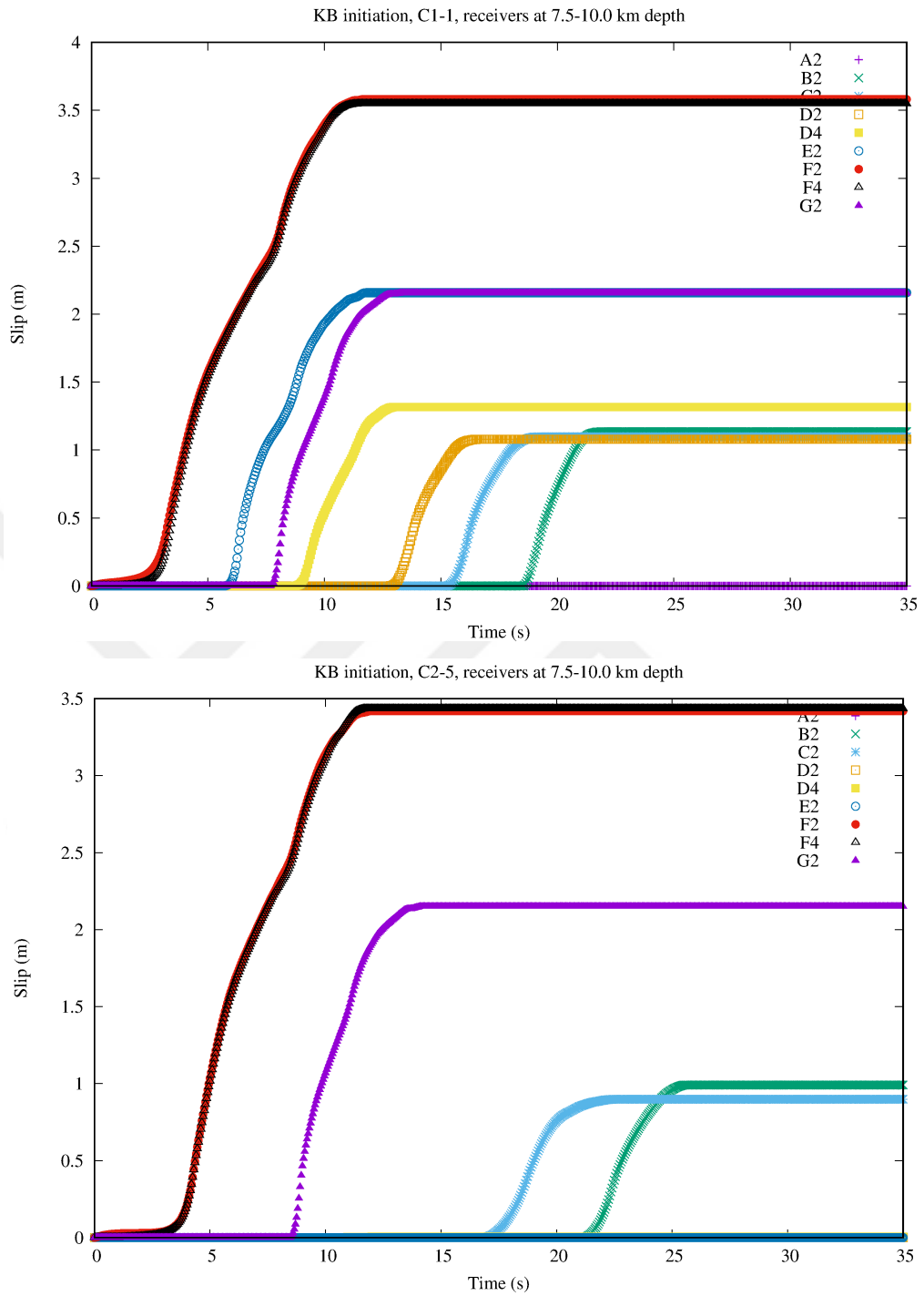
Figure 6.19. Temporal slip change graphics for cases 'KB-in_PI-1766_C1-1' (top) and 'KB-in_PI-1766_C2-5' (bottom) (Table 6.1). Receivers are located at 7.5 and 10.0 km depths. Receiver locations are shown in Fig.6.15.
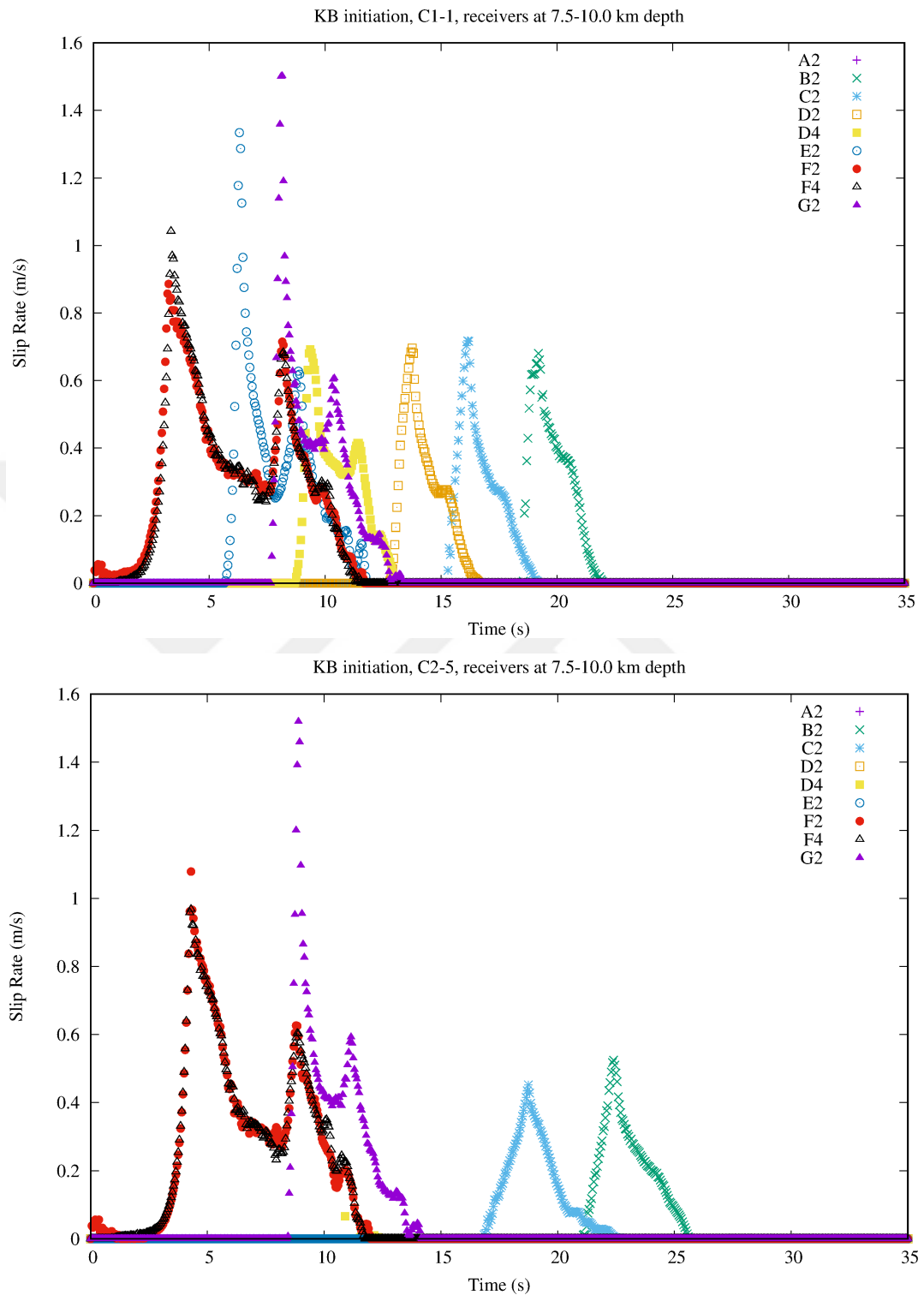
Figure 6.20. Temporal slip-rate change graphics for cases 'KB-in_PI-1766_C1-1' (top) and 'KB-in_PI-1766_C2-5' (bottom) (Table 6.1). Receivers are located at 7.5 and 10.0 km depths. Receiver locations are shown in Fig.6.15.
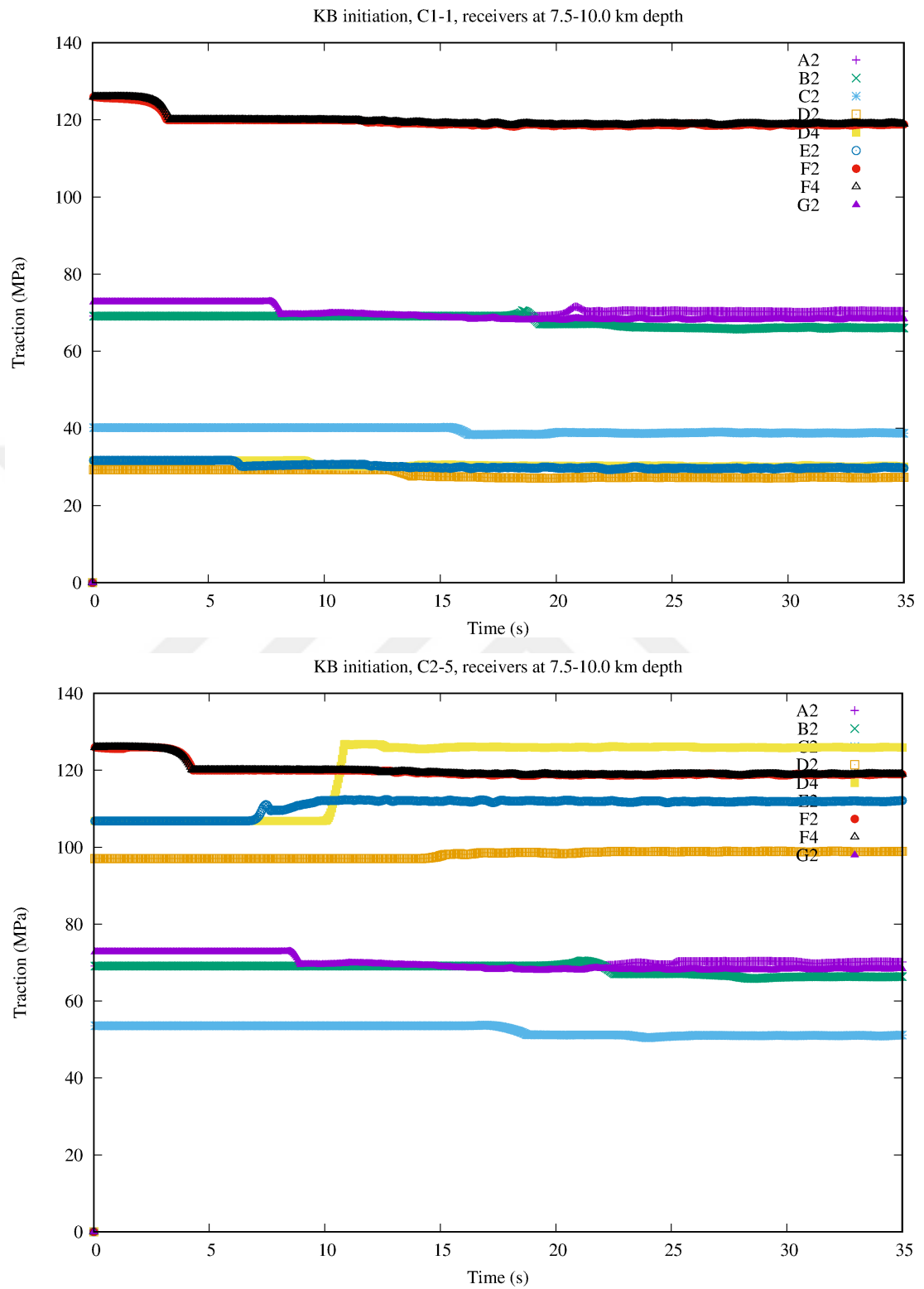
Figure 6.21. Temporal traction change graphics for cases 'KB-in_PI-1766_C1-1' (top) and 'KB-in_PI-1766_C2-5' (bottom) (Table 6.1). Receivers are located at 7.5 and 10.0 km depths. Receiver locations are shown in Fig.6.15.
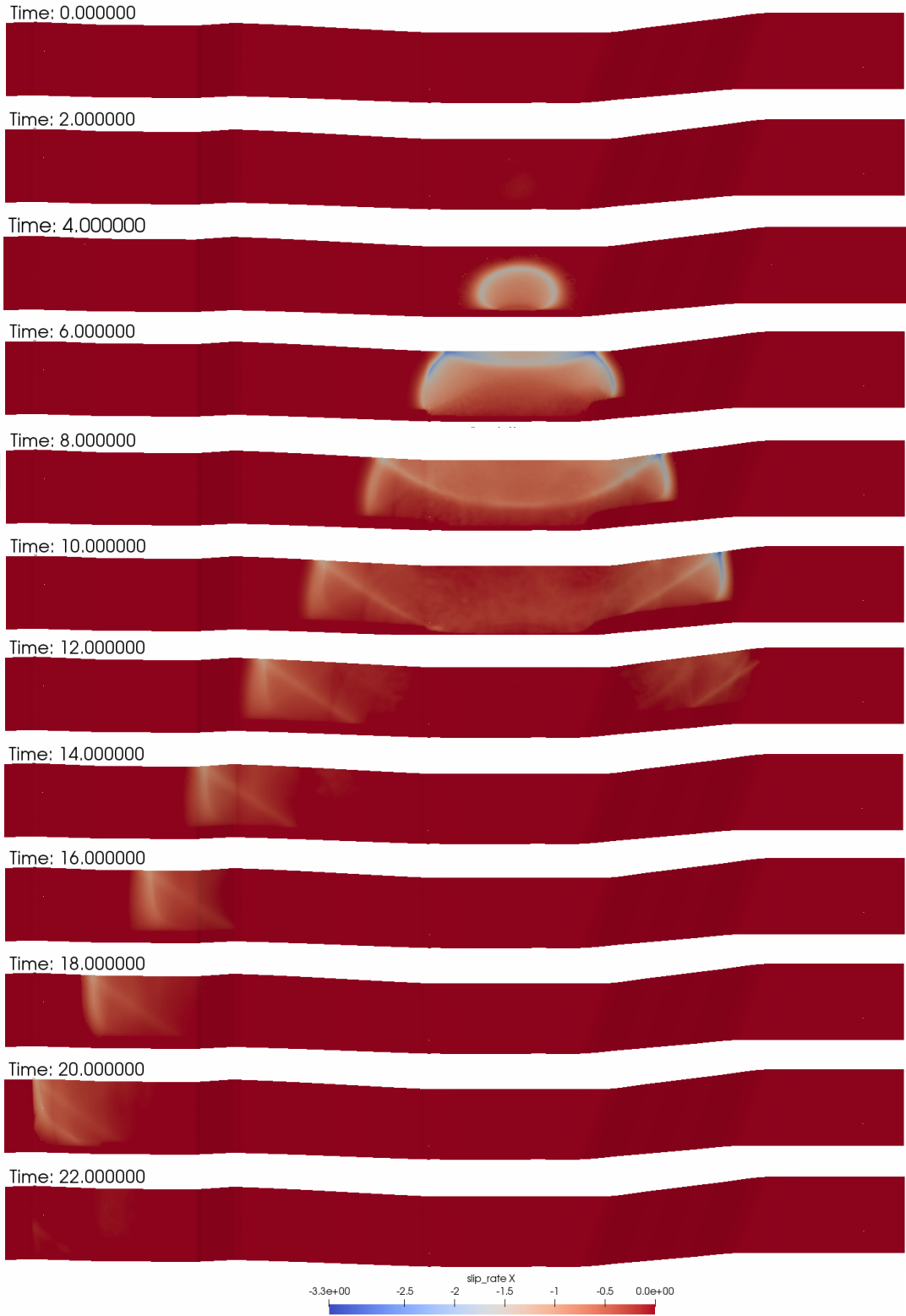
Figure 6.22. Slip-rate time snapshots for 2 seconds intervals for the rupture initiation at central KB for the case 1 (KB-in_PI-1766_C1-1).
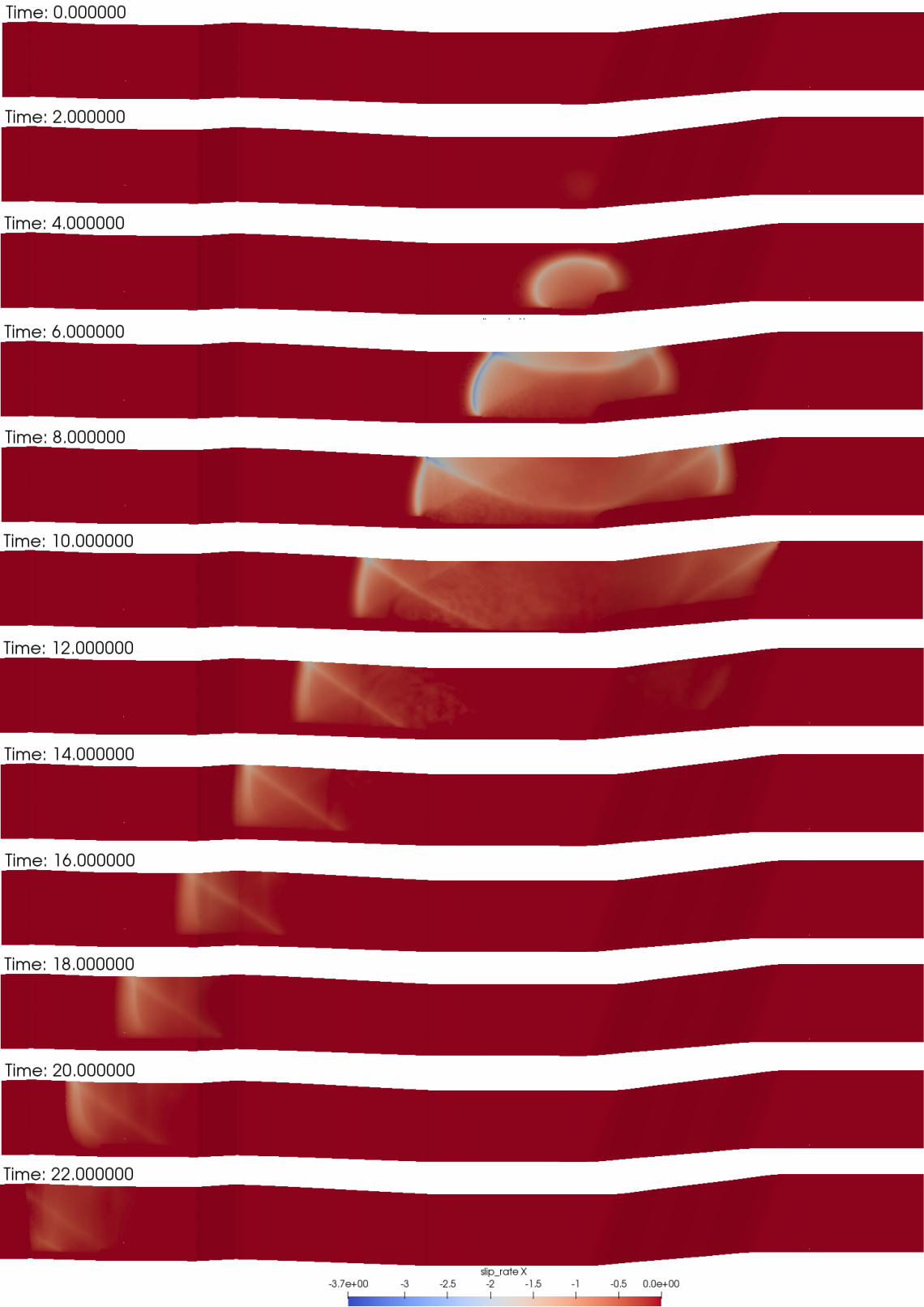
Figure 6.23. Slip-rate time snapshots for 2 seconds intervals for the rupture initiation at eastern KB for the case 17 (KBeast-in_PI-1766_C1-1).

Figure 6.24. Slip-rate time snapshots for 2 seconds intervals for the rupture initiation at PI for the case 33 (PI-in_PI-1766_C1-1).

It has been noticed that rupture does not enter into the PI fault segment if it last ruptured at 1894 and Yamamoto et al. (2019)'s assumption (%74 lock, tempering) is valid for WH region for central and eastern KB initiations (Fig. 6.11). Namely, rupture can extent into east if WH segment is %75 locked. This may be a result of effect of dynamic stress transfer. Therefore, it is probable that rupture may not extend into the PI segment if it last ruptured during 1894 earthquake.

Since we have thousands of points on the fault and ground surfaces, 9 points at the shallow and 9 points at the deep part of the fault surface are selected as observation points (Fig. 6.15). Points A1-2, B1-2, C1-2, F1-2 and G1-2 are located at the centers of related segments, and points D1-2, E1-2 and F3-4 are located at segment boundaries. Hence, E1 and E2 are located at the entrance to the partially creeping section in central Marmara Basin segments.

Slip, slip-rate and traction graphs are plotted for these 18 observation points for our 80 cases. Considering very dense data set and the high probability of initiation of the expected earthquake at KB fault segment, only time dependent along strike slip, slip-rate and traction graphics for cases 1 (KB-in_PI-1766_C1-1) and 10 (KB-in_PI-1766_C2-5) are depicted in this section as for central KB initiations (Source is at F2) (Table 6.1).

Total slip at F and G are slightly larger for the cases with homogeneous partially creeping areas ('…C1-1'; Fig. 5.8) compared to the cases with complex partially creeping areas at ('…C2-5'; Fig. 5.9) (Fig. 6.16 and 6.19, top graphs). In addition, slip at G1 is larger than the slip at E1, since the initial stress is higher even if the receiver G1 is further than the source (Fig. 6.15 and Fig. 6.16). Also, it is the same for receivers C1 and D1 due to higher initial stress at the segment C (Fig. 6.18). In addition, total slip is higher at point B2 comparing C2 and D2 (Fig. 6.19, both graphs).

Generally higher slip-rates are observed when partially creeping segments are homogenously stressed ('…C1-1'; Fig. 5.8), so lower slip-rates are derived when complex partially creeping models ('…C2-5'; Fig. 5.9) are used (Fig. 6.17 and 6.20). Also, rupture terminates within 22 seconds for the case '…C1-1', and within 26 seconds for '…C2-5' for 1766 rupture at segment PI. Slip and slip-rates at points A, D and E (Fig. 6.15) are zero for

the '…C2-5' case owing to the fact that these local areas are totally creeping, being not attributed as asperities.

Traction change at observation points D4 (Fig. 6.21) and E1 (Fig. 2.6.12) are different from other locked and creeping points for the case '…C2-5' (the complex partially creeping model at CB) in comparison to the results for the case '…C1-1' in that final shear tractions becomes very high and close to the static friction level (T_y) (Fig. 6.18 and 6.21, bottom graphs). Therefore, CB segments may rupture for a second time through being triggered by the aftershock activity. In addition, a second stress drop motion is observed at receiver A1 for the case '…C1-1' due to dynamic stress change (Fig. 6.18 and 6.21, Top graphic, purple peak).

Higher peak slip-rate values are observed for eastern KB initiation compared to the central KB initiation. For example, peak slip-rates are 3.7 m/s for eastern KB initiation and 3.3 m/s for central KB initiation for the homogeneous initial stress distributions at partially creeping segments ('…C1-1') (Fig. 6.23 and 6.22). The difference between peak slip-rates are higher when complex asperities are embedded into the partially creeping segments ('…C2-5'), as it is 3.6 m/s for eastern KB initiation, and 2.9 m/s for central KB initiation.

Our simulation results present that duration of the expected MMF earthquake may not be longer than 30 seconds for the rupture initiation at central or eastern KB, as M7.4 1999 İzmit event is finalized in ~45 seconds. On the other hand, the rupture time of PI initiation case may last a few seconds longer (~34) as it is expected due to the longer distance from source to receiver (segment B) (Fig. 6.24). Considering latest turbidity records of 1894 earthquake on the PI fault segment (Drab et al., 2015), the cases for PI last ruptured at 1894 may become more realistic. Therefore, the magnitude of the expected Main Marmara Fault Earthquake may not exceed M_w7.1 (Table 6.1).

7. CONCLUSION

In this study, dynamic earthquake rupture scenarios were generated for the Main Marmara Fault using realistic initial stress conditions based on previous work. Historical earthquake data and turbidity records are merged in order to determine last rupture times of each fault segment, and annual slip-rate deficits are selected from recent geodetic studies. When loading the stress, also the heterogeneity of the coupling of the fault interface is considered. Thus, local loaded shear stresses are calculated. Orientations of maximum principal compressive stress axes are defined by recent studies. Therefore, the regional normal stress is constrained with the local stress orientation information of each segment.

Partially creeping segments of the Marmara Sea is adapted into our simulations considering recent repeating earthquake and extensometer analyzes. Therefore, Western High and Central Basin segments are evaluated separately, and the effect of partial creep in these segments is investigated by making 80 scenarios for various types of partial creep using three-dimensional dynamic earthquake fracture simulations in the Sea of Marmara.

It has been observed that the type of the partial creep can lead 0.5 to 1.0 moment magnitude difference, and 10 cm to 30 cm along-strike slip difference. These differences are smaller if the Prince's Island segment last ruptured during 1766 earthquake, and they are larger if the last rupture of the Prince's Island segment is the 1894 event.

Consequently, it has been found out that the expected Main Marmara Fault earthquake most probably can initiate at Kumburgaz Basin Segment, and the largest ground surface displacements can occur at the surrounding area of this segment. Since this segment is close to İstanbul Metropolitan area, its destructive effect is very important. If the Prince's Island fault is last ruptured at 1766, it can also be an initiation point and rupture can extend into this segment independent of the location of the initiation point. On the other hand, if it last ruptured at 1894, rupture can't start at PI segment and it may not extend into this segment, depending on the type of the partially creeping segments. Also, the required strength excess is larger for the initiation at segment PI than the initiation at KB. This is an indicator of that

central or eastern KB initiation has a high possibility. It is noticed that eastern and central Kumburgaz Basin initiations of rupture do not present large differences in slip amounts. The highest moment magnitude we obtained for the rupture scenarios is Mw7.2 and most scenarios end up with an earthquake around Mw7.0.

Moreover, sub-shear velocities are observed for all 80 scenarios. When heterogeneous interseismic behavior is considered we find that for most scenarios possible earthquake magnitude does not exceed Mw7.2. Also, if PI segment last ruptured at 1894 earthquake (Drab et al., 2015), the moment magnitude of the expected earthquake may not be larger than Mw7.1.

REFERENCES

Aagaard, B., M. Knepley, and C. Williams, 2017, "PyLith v2.2.1. Davis, CA: Computational Infrastructure of Geodynamics", DOI: 10.5281/zenodo.8866.00.

Aagaard, B., M. Knepley, M., and C. Williams, 2012, "Crustal Deformation Modelling Tutorial".

Abrahamson, N., and W. Silva, 2008, "Summary of the Abrahamson & Silva NGA Ground Motion Relations", *Earthquake Spectra,* Vol. 24, pp. 67-97.

Aki, K., and P. G. Richards, 1980, "Quantitative Seismology, Theory and Methods", H. Freeman and Co., San Francisco, California. Vol. 1.

Aki, K., and P. G. Richards, "Quantitative Seismology", *2nd ed. University Science Books*, Sausalito, CA, USA, 2002.

Aksoy, M. E., M. Meghraoui, M. Vallee, and Z. Çakır, 2010, "Rupture Characteristics of the A.D. 1912 Mürefte (Ganos) Earthquake Segment of the North Anatolian Fault (Western Turkey)", *Geology*, Vol. 38, No. 11, p. 991-994, DOI: 10.1130/G31447.1.

Aksu, A. E., T. J. Calon, R. N. Hiscott, and D. Yaşar, 2000, "Anatomy of the North Anatolian Fault Zone in the Marmara Sea Western Turkey: Extensional Basin above a Continental Transform", *GSA Today*, Vol. 10, pp. 1-2.

Ambraseys, N. N., 2002, "The Seismic Activity of the Marmara Sea Region over the Last 2000 Years", *Bulletin of the Seismological Society of America*, Vol. 92, No. 1, pp. 1–18.

Ambraseys, N. N. and C. F. Finkel, Seismicity of Turkey and Adjacent Areas, A Historical Review, 1500-1800. Eren Yayincilik ve Kitapcilik Ltd., 1995.

Ambraseys, N. N., "Earthquakes in the Mediterranean and Middle East: A Multidisciplinary Study of Seismicity up to 1900", Cambridge University Press, Imperial College, London, ISBN 978 0 521 87292 8, 2009.

Ambraseys, N. N., and C. F. Finkel, 1987, "The Saros-Marmara Earthquake of 9 August 1912", *Earthquake Engineering and Structural Dynamics,* Vol. 15, pp. 189–211.

Ambraseys, N. N., and J. A. Jackson, 2000, "Seismicity of the Sea of Marmara (Turkey) since 1500", *Geophysical Journal International*, Vol. 141, pp. F1-F6.

Andrews, D. J, 1976, "Rupture Velocity of Plane - Strain Shear Cracks", *Journal of Geophysical Research*, Vol. 81, pp. 5679-5687.

Aochi, H., and A. Kato, 2010, "Dynamic Rupture of Crosscutting Faults: A Pos - Sible Rupture Process for the 2007 M_W 6.6 Niigata-ken Chuetsu-Oki Earth - Quake", *Journal of Geophysical Research*, Vol. 115, No. B05310, DOI: 10.1029/2009JB006556.

Aochi, H., and T. Ulrich, 2015, "A Probable Earthquake Scenario near Istanbul Determined from Dynamic Simulations", *Bulletin of the Seismological Society of America*, Vol. 105, No. 3, pp. 1468–1475, DOI: 10.1785/0120140283.

Aochi, H., E. Fukuyama, M. Matsu'ura, 2003, "Spontaneous Rupture Propagation on a Non-planar Fault in 3-D Elastic Medium", *Pure and Applied Geophys*ics, Vol. 157 pp. 2003–2027.

Armijo, R., B. Meyer, S. Navarro, G. King, and A. Barka, 2002, "Asymmetric Slip Partitioning in the Sea of Marmara Pull-Apart: A Clue to Propagation Processes of the North Anatolian Fault?", *Terra Nova,* Vol. 14, pp. 80–86.

Armijo, R., N. Pondard, B. Meyer, G. Uçarkus, B. M. de Lepinay, J. Malavieille , S. Dominguez, M. Gustcher, S. Schmidt, C. Beck, N. Çagatay, Z. Çakir, C. Imren, K. Eris, B. Natalin, S. Özalaybey, L. Tolun, I. Lefevre, L. Seeber, L. Gasperini, C. Rangin, O. Emre, and K. Sarikavak, 2005, "Submarine Fault Scarps in the Sea of Marmara Pull-Apart (North Anatolian Fault): Implications for Seismic Hazard in İstanbul", *AGU and the Geochemical Society,* ISSN: 1525-2027.

Bayrakci, G., M. Laigle, A. Becel, A. Hirn, T. Taymaz, S. Yolsal-Çevikbilen, and SEISMARMARA team, 2013, "3-D sediment-basement tomography of the Northern Marmara trough by a dense OBS network at the nodes of a grid of controlled source profiles along the North Anatolian fault", *Geophysical Journal International.*

Barış, Ş., J. Nakajima, A. Hasegawa, Y. Honkura, A. Ito, and B. Üçer, 2005, "Three Dimensional Structure of Vp, Vs and Vp/Vs in the Upper Crust of the Marmara Region, NW Turkey", *Earth Planets and Space*, Vol. 57, pp. 1019-1038.

Barka, A. and K. Kadinsky-Cade, 1988, "Strike-Slip Fault Geometry and its Influence on Earthquake Activity", *Tectonics, Vol*. 7, pp. 663-684.

Barka, A., 1992, "The North Anatolian Fault Zone", *Annales Tectonicae*, Vol. 6, pp. 164-195.

Barka, A., G. Uçarkuş, and T. Taymaz, 2002, "Obituary", *Turkish Journal of Earth Sciences*, Vol. 11, pp. 83-85.

Başarır Baştürk, N., N. Meral Özel, Y. Altınok, and T. Y. Duman, "Türkiye ve Yakın Çevresi İçin Geliştirilmiş Tarihsel Dönem (MÖ 2000 - MS 1900) Deprem Kataloğu", 2017.

Başarır Baştürk, N., N. Meral Özel, and M. Caciagli, 2016, "Seismic parameters re-determined from historical seismograms of 1935-Erdek–Marmara Island and 1963-Çınarcık Earthquakes", *Earth, Planets and Space*, 68:158 DOI 10.1186/s40623-016-0528-8.

Beck, C., B. M. de Lepinay, J. L. Schneider, M. Cremer, N. Çağatay, E. Wendenbaum, S. Boutareaud, G. Menot, S. Schmidt, O. Weber, K. Eris, R. Armijo, B. Meyer, N. Pondard, M. A. Gutscher, and the MARMARACORE Cruise Party, J. L. Turon, L. Labeyrie, E. Cortijo, Y. Gallet, H. Bouquerel, N. Gorur, A. Gervais, M. H. Castera, L. Londeix, A. de Resseguier, A. Jaouen, 2007, "Late Quaternary co-seismic sedimentation in the Sea of Marmara's deep Basin", *Sedimentary Geology,* Vol. 199 pp. 65-89.

Beyhan, G., and H. H. Selim, 2007, "Tectonics of the North Anatolian Fault Located in the Sea of Marmara According to Seismic Reflection Data", International Earthquake Symposium Kocaeli.

Bizzarri, A., and M. Cocco, 2003, "Slip-weakening behavior during the propagation of dynamic ruptures obeying rate- and state-dependent friction laws", *Journal Of Geophysical Research*, Vol. 108, No. B8, 2373, DOI: 10.1029/2002JB002198.

Bizzarri, A., 2010, "An efficient mechanism to avert frictional melts during seismic ruptures", Earth and Planetary Science Letters Vol. 296, pp. 144–152. DOI: 10.1016/j.epsl.2010.05.012.

Bizzarri, A., 2012, "Rupture speed and slip velocity: What can we learn from simulated earthquakes?", *Earth and Planetary Science Letters*, Vol. 317-318 pp. 196–203.

Boaz, R., 2009, PQL II. http://www.passcal.nmt.edu/content/pql-ii-program-viewing-data.

Bohnhoff, M., H. Grosser, and G. Dresen, 2006, "Strain Partitioning and Stress Rotation at the North Anatolian Fault Zone from Aftershock Focal Mechanisms of the 1999 İzmit *M*w = 7.4 Earthquake", *Geophysical Journal International,* Vol. 160, pp. 373-385.

Bohnhoff, M., F. Bulut, G. Dresen, P. E. Malin, T. Eken, and M. Aktar, 2013, "An earthquake gap South of Istanbul", Nature Communications, DOI: 10.1038/ncomms2999.

Bohnhoff, M., C. Wollin, D. Domigall, L. Küperkoch, P. Martinez-Garzon, G. Kwiatek, and P. E. Malin, 2017, "Repeating Marmara Sea earthquakes: indication for fault creep", *Geophysical Journal International*, Vol. 210, pp. 332–339.

Bohnhoff, M., G. Dresen, F. Bulut, M. Nurlu, D. Akin, T. Kilic, H. Ito, and P. Malin, 2012, "GONAF – A deep Geophysical Observatory at the North Anatolian Fault", *Borehole Seosmology*.

Bouchon, M., M. N. Toksöz, H. Karabulut, M. P. Bouin, M. Dietrich, M. Aktar, and M. Edie, 2002, "Space and Time Evolution of Rupture and Faulting during the 1999 İzmit (Turkey) Earthquake", *Bulletin of the Seismological Society of America,* Vol. 92, pp. 256–266, DOI: 10.1785/0120000845.

Boore, D. M., and G. M. Atkinson, 2008, "Ground motion prediction equations for the average horizontal component of PGA, PGV, and 5%-damped PSA at spectral periods be- tween 0.01 s and 10 s", *Earthquake Spectra*, Vol. 24, pp. 99–138.

Bulut, F., and M. Aktar, 2007, "Accurate relocation of I: Izmit earthquake (Mw = 7.4, 1999) aftershocks in Çınarcık Basin using double difference method", *Geophysical Research Letters*, Vol. 34, L10307, DOI: 10.1029/2007GL029611.

Bulut, F., M. Bohnhoff, W. L. Ellsworth, M. Aktar, and G. Dresen, 2009, "Microseismicity at the North Anatolian Fault in the Sea of Marmara offshore Istanbul, NW Turkey", *Journal of Geophysical Research*, Vol. 114, B09302, DOI: 10.1029/2008JB006244.

Çağatay, M. N., L. Erel, L. G. Bellucci, A. Polonia, L. Gasperini, K. K. Eriş, Ü. Sancar, D. Biltekin, G. Uçarkuş, U. B. Ülgen, and E. Damcı, 2012, "Sedimentary earthquake records in the İzmit Gulf, Sea of Marmara, Turkey", *Sedimentary Geology*, Vol. 282 pp. 347-359.

Carlson, J. and J. Langer, 1989, "Mechanical model of an earthquake fault", *Physical Review A*, Vol. 40, pp. 6470– 6484.

Cochard, A. and R. Madariaga, 1994, "Dynamic faulting under rate-dependent friction", *Pure Applied Geophysics*, Vol. 142, pp. 419– 445.

Çakir, Z., J-B. de Chabalier, R. Armijo, B. Meyer, A. Barka, and G. Peltzer, 2003, "Coseismic and early postseismic slip associated with the 1999 Izmit earthquake (Turkey), from SAR interferometry and tectonic field observations", *Geophysical Journal International*, 155, 93-110.

Dewey, J. F., R. E. Holdswoth and R. A. Strachan, 2012, "Transpression and Transtension Zones", *http://sp.lyellcollection.org*.

Dieterich, J. H., 1972, "Time-dependentfrictioninrocks", *Journal of Geophysical Research*, Vol. 77, No. 20, pp. 3690–3697.

Douilly, R., H. Aochi, E. Calais, and A. M. Freed, 2015, "Three-dimensional dynamic rupture simulations across interacting faults: The M_W 7.0, 2010, Haiti earthquake", *Journal of Geophysical Research*, DOI: 10.1002/2014JB011595.

Douilly, R., H. Aochi, E. Calais, and M. Freed, 2014, "Three-dimensional dynamic rupture simulations across interacting faults: The M_W7.0, 2010, Haiti earthquake", *Journal of Geophysical Research*, Solid Earth, Vol. 120, pp. 1108-1128, DOI: 10.1002/2014JB011595.

Drab, L., "Marine Paleoseismology and Paleomagnetism in Marmara Sea", (Ph.D. Thesis) Paris Sud University, pp. 113-127, 2012.

Drab, L., A. Hubert Ferrari, S. Schmidt, and P. Martinez, 2013, "The earthquake sedimentary record in the western part of the Sea of Marmara, Turkey", *Natural Hazards and Earth System Sciences*, Vol. 12, pp. 1235-1254.

Drab, L., A. Hubert-Ferrari, S. Schmidt, P. Martinez, J. Carlut, and M. El Ouahabi, 2015, "Submarine Earthquake History of the Çınarcık Segment of the North Anatolian Fault

in the Marmara Sea, Turkey", *Bulletin of the Seismological Society of America*, Vol. 105, No. 2A, pp. 622–645, DOI: 10.1785/0120130083.

Dresen,   G., M. Bohnhoff, M. Aktar, and H. Eyidogan, 2008, "Drilling the North Anatolian Fault", *Workshop Reports,* DOI: 10.2204/iodp.sd.6.10.2008.

Erdik, M., M. Demircioglu, K. Sesetyan, E. Durukal, and B. Siyahi, 2004, "Earthquake hazard in Marmara Region, Turkey", *Soil Dynamics and Earthquake Engineering*, Vol. 24 pp. 605–631.

Erdik, M., 2013, "Earthquake Risk in Turkey", *Science,* Vol. 341, pp. 724, DOI: 10.1126/science.1238945.

Ergintav, S., R. E. Reilinger, R. Çakmak, M. Floyd, Z. Çakır, U. Doğan, R. W. King, S. McClusky, and H. Özener, 2014, "Istanbul'searthquakehotspots:Geodeticconstraints on strain accumulation along faults in the Marmara seismic gap", *Geophysical Research Letters*, DOI: 10.1002/2014GL060985.

Ergun, M., and E. Ozel, 1995, "Structural relationship between the Sea of Marmara Basin and the North Anatolian Fault Zone", *Terra Nova*, Vol. 7, pp. 278-288.

Fukuyama, E., and K. X. Hao, 2013, "Subparallel dipping faults that ruptured during the 2008 Wenchuan earthquake", *Bulletin of the Seismological Society of America*, Vol. 103, pp. 2128–2134.

Geli, L., P. Henry, T. Zitter, S. Dupré, M. Tryon, M. N. Çağatay, B. Mercier de Lépinay, X. Le Pichon, A. M. C. Şengör, N. Görür, B. Natalin, G. Uçarkuş, S. Özeren, D. Volker, L. Gasperini, P. Burnard, S. Bourlange, 2008, "Gas emissions and active tectonics within the submerged section of the North Anatolian Fault zone in the Sea of Marmara", *The Marmara Scientific Party.*

Gu, J. C., J. R. Rice, A. R. Ruina and S. TSE, 1984, "Slip Motion and Stability of a Single Degree of Freedom Elastic System with Rate- and State-dependent Friction", *Journal of the Mechanics and Physics of Solids*, Vol. 32, pp. 167-196.

Guidoboni, E., G. Traina, A. Comastri, 1994, "Catalogue of ancient earthquakes in the Mediterranean area up to the 10th century", INGV, Rome. ISBN 88-85213-06-5.

Gürbüz, C., M. Aktar, H. Eyidoğan, A. Cisternas, H. Haessler, A. Barka, M. Ergin, N. Türkelli, O. Polat, B. Üçer, H. S. Kuleli, S. Barış, B. Kaypak, T. Bekler, E. Zor, F. Biçmen, and A. Yörük, 2000, "The seismotectonics of the Marmara Region (Turkey): Results from a microseismic experiment", *Tectonophysics*, Vol. 316, pp. 1–17.

Harris, R. A., and S. M. Day, 1999, "Dynamic 3D simulations of earth- quakes on en echelon faults", *Geophysical Research Letters,* Vol. 26, pp. 2089–2092.

Hergert, T., and O. Heidbach, 2010, "Slip-rate variability and distributed deformation in the Marmara Sea fault system", *Nature Geoscience*, Vol. 3, pp. 132–135.

Hergert, T., and O. Heidbach, 2011, "Geomechanical model of the Marmara Sea region— II. 3-D contemporary background stress field", *Geophysical Journal International*, Vol. 185, pp. 1090–1102.

Hubert-Ferrari, A., A. Barka, E. Jacques, S. S. Nalbant, B. Meyer, R. Armijo, P. Tapponnier, and G. C. P. King, 2000, "Seismic Hazard in the Marmara Sea Region Following the 17 August 1999 Izmit Earthquake, *Nature*, Vol. 404, pp. 269–273.

Horiuchi, S., G. Rocco, and A. Hasegawa, 1995, "Discrimination of Fault Planes from Auxiliary Planes Based on Simultaneous Determination of Stress Tensor and a Large Number of Fault Plane Solutions", *Journal of Geophysical Research,* pp. 8327-8338.

Ito, A., S. B. Ucer, S. Baris, Y. Honkura, A. Nakamura, T. Kono, R. Pektas, T. Komut, A. Hasegawa, and A. M. Isikara, 2002, "Aftershock Activity of 1999 İzmit Earthquake,

Turkey, Revealed from Microearthquake Observations", *Bulletin of the Seismological Society of America,* pp. 418–427.

İnan, S., S. Ergintav, R. Saatçılar, B. Tüzel, and Y. İravul, 2007, "Turkey Makes Major Investments in Earthquake Research", *EOS Transactions*, Vol. 88, pp. 333-334.

Imren, C., X. Le Pichon, C. Rangin, E. Demirbag, B. Ecevitoglu, N. Görür, 2001, "The North Anatolian Fault within Sea of Marmara: a new interpretation based on multi-channel seismic and multi-beam bathymetry data", *Earth and Planetary Science Letters*, Vol. 186, pp. 143–158.

Kame, N., S. Fujita, M. Nakatani, and T. Kusakabe, 2012, "Effects of a revised rate- and state-dependent friction law on aftershock triggering model", *Tectonophysics*, Vol. 600, pp. 187–195, DOI: 10.1016/j.tecto.2012.11.028.

Kanamori, H., 1997, "The Energy Release in Great Earthquakes", *JGR*, https://doi.org/10.1029/JB082i020p02981.

Karabulut, H., M. P. Bouin, M. Bouchon, M. Dietrich, C. Cornou, and M. Aktar, 2002, "The seismicity in the Eastern Marmara Sea after the 17 August 1999 Izmit Earthquake", *Bulletin of the Seismological Society of America*, Vol. 92, No. 1, pp. 387–393.

Karabulut, H., S. Ozalabey, T. Taymaz, A. Aktar, O. Selvi, and A, Kocaoglu, A., 2003, "A tomographic image of the shallow crustal structure in the Eastern Marmara", *Geophysical Research Letters*, Vol. 30 pp. 2277.

Karabulut, H., J. Schmittbuhl, S. Özalaybey, O. Lengliné, A. Kömeç-Mutlu, V. Durand, M. Bouchon, G. Daniel, and M. P. Bouin, 2011, "Evolution of The Seismicity in the Eastern Marmara Sea a Decade Before and After the 17 August 1999 Izmit Earthquake", *Tectonophysics*, Vol. 510, pp. 17–27.

Kase, Y., 2010, "Slip-Length Scaling Law for Strike-Slip Multiple Segment Earthquakes Based on Dynamic Rupture Simulations", *Bulletin of the Seismological Society of America,* Vol. 100, pp. 473–481, DOI: 10.1785/0120090090.

King, G. C. P., A. Hubert-Ferrari, S. S. Nalbant, B. Meyer, R. Armijo, and D. Bowman, 2001, "Coulomb Interactions and the 17 August İzmit, Turkey Earthquake", *Earth and Planetary Sciences,* pp. 557-569.

Kiratzi, A. A., 2002, "Stress Tensor Inversions along the Westernmost North Anatolian Fault Zone and Its Continuation into the North Aegean Sea", *Geophysical Journal International,* pp. 360-376.

Klein, E., Z. Duputel, F. Masson, H. Yavasoglu, and P. Agram, 2017, "Aseismic Slip and Seismogenic Coupling in the Marmara Sea: What Can We Learn from Onland Geodesy?", *Geophysical Research Letters*, DOI: 10.1002/2017GL072777.

Koller, M. G., M. Bonnet, and R. Madariaga, 1992, "Modeling of Dynamical Crack Propagation Using Time-domain Boundary Integral Equations", *Wave Motion*, Vol. 16, pp. 339–366.

Korkusuz Öztürk, Y., N. Meral Özel, and A. D. Özbakır, 2015, "States of Local Stresses in the Sea of Marmara through the Analysis of Large Numbers of Small Earthquakes", *Tectonophysics*, Vol. 665, pp. 37-57, https://doi.org/10.1016/j.tecto.2015.09.027.

Korkusuz Öztürk, Y., and N. Meral Özel, 2018, "Relative Locations of Clustered Earthquakes in the Sea of Marmara and States of Local Stresses in the East of the Central Marmara Basin", *Springer Nature*, pp. 453-480. https://doi.org/10.1007/978-3-319-77359-9_20.

Kostrov, B. V., and S. Das, 2005, Principles of Earthquake Source Mechanics, *Chambridge Monographs on Mechanics and Applied Mathematics*, USA.

Kozdon, J. E., and E. M. Dunham, 2013, "Rupture to the Trench: Dynamic Rupture Simulations of the 11 March 2011 Tohoku Earthquake", *Bulletin of the Seismological Society of America,* Vol. 103, No. 2B, pp. 1275–1289, DOI: 10.1785/0120120136.

Le Pichon, X., T. Taymaz, and A. M. C. Şengör, 1999, "The Marmara Fault and the Future İstanbul Earthquake", *Proc. ITUIAHS International Conference on the Kocaeli Earthquake, İstanbul,* pp. 41-54.

Le Pichon, X., A. M. C. Şengör, E. Demirbağ, C. Rangın, C. Imren, R. Armijo, N. Görür, N. Çağatay, B. Mercier De Lepinay, B. Meyer, R. Saatçiler and B. Tok, 2001, "The Active Main Marmara Fault", *Earth and Planetary Science Letters,* Vol. 192, pp. 595–616.

Le Pichon, X., N. Chamot-Rooke, and C. Rangin, 2003, "The North Anatolian fault in the Sea of Marmara", Journal of Geophysical Research, Vol. 108, DOI:10.1029/2002JB001862.

Lienert, B. R. E., "Report on modifications made to Hypocenter, Technical report, Institute of Solid Earth Physics", University of Bergen (Bergen, Norway), 1991.

Lienert, B. R. E., E. Berg, and L. N. Frazer, 1986, "Hypocenter: An earthquake location method using centered, scaled, and adaptively least squares", *Bulletin of the Seismological Society of America*, Vol. 76, pp. 771–783.

Lienert, B. R., and J. Havskov, 1995, "A Computer Program for Locating Earthquakes Both Locally and Globally", *Seismological Research Letters,* Vol. 66, No. 5.

McHugh, C. M. G., L. Seeber, M. H. Cormier, J. Dutton, N. Cagatay, A. Polonia, W. B. F. Ryan, and N. Gorur, 2006, "Submarine earthquake geology along the North Anatolia Fault in the Marmara Sea, Turkey: A model for transform Basin sedimentation", *Earth and Planetary Science Letters*, Vol. 248, pp. 661–684.

McHugh, C. M. G., N. Braudy, M. N. Çağatay, C. Sorlien, M. H. Cormier, L. Seeber, and P. Henry, 2014, "Seafloor fault ruptures along the North Anatolia Fault in the Marmara Sea, Turkey: Link with the adjacent Basin turbidite record", *Marine Geology,* Vol. 353, pp. 65-83.

Meade, B. J., B. H. Hager, S. C. McClusky, R. E. Reilinger, S. Ergintav, L. Onur, A. Barka, and H. Özener, 2002, "Estimates of Seismic Potential in the Marmara Sea Region from Block Models of Secular Deformation Constrained by Global Positioning System Measurements", *Bulletin of the Seismological Society of America,* Vol. 92, pp. 208–215.

Mikumo, T., K. B. Olsen, E. Fukuyama, Y. Yagi, 2003, "Stress–Breakdown Time and Slip-Weakening Distance İnferred from Slip–Velocity Functions on Earthquake Faults", *Bulletin of the Seismological Society of America,* Vol. 93, pp. 264–282.

Oglesby, D. D., and P. M. Mai, 2012, "Fault Geometry, Rupture Dynamics and Ground Motion from Potential Earthquakes on the North Anatolian Fault under the Sea of Marmara", *Geophysical Journal International*, Vol. 188, pp. 1071–1087.

Oglesby, D. D., S. M. Day, Y. G. Li, and J. E. Vidale, 2003, "The 1999 Hector Mine earthquake: The Dynamics of a Branched Fault System", *Bulletin of the Seismological Society of America,* Vol. 93, pp. 2459–2476.

Okay, A. I., A. Kaşlılar-Özcan, C. İmren, A. Boztepe-Güney, E. Demirbağ, and İ. Kuşçu, 2000, "Active Faults and Evolving Strike-Slip Basin in the Marmara Sea, Northwest Turkey: A Multichannel Seismic Reflection Study", *Tectonophysics,* pp. 189-218.

Örgülü, G., and M. Aktar, 2001, "Regional Moment Tensor Inversion for Strong Aftershocks of the August 17, 1999 İzmit Earthquake (Mw = 7.4)", *Geophysical Research Letters,* Vol. 28, No. 2, pp. 371–374.

Örgülü, G., 2011, "Seismicity and Source Parameters for Small-Scale Earthquakes along the Splays of the North Anatolian Fault (NAF) in the Marmara Sea", *Geophysical Journal International*, Vol. 184, pp. 385-404.

Özalaybey, S., M. Ergin, M. Aktar, C. Tapırdamaz, F. Biçmen, and A. Yörük, 2002, "The 1999 İzmit Earthquake Sequence in Turkey: Seismological and Tectonic Aspects", *Bulletin of the Seismological Society of America,* pp. 376-386.

Parejas, E., I. H. Akyol, and E. Altinli, 1942, "Le Tremblement de Terre d'Erzincan du 17 Decembre 1939", *Rev. Fac. Sci. Univ. NVI,* pp. 177-222.

Parke, J. R., T. A. Minshull, G. Anderson, R. S. White, D. McKenzie, I. Kuşçu, J. M. Bull, N. Görür, and C. Şengör, 1999, "Active Faults in the Sea of Marmara, Western Turkey, Imaged by Seismic Refection Profiles", *Terra Nova*, Vol. 11, pp. 223-227.

Parsons, T., 2004, "Recalculated Probability of MZ7 Earthquakes Beneath the Sea of Marmara", *Journal of Geophysical Research*, Vol. 109, No. B05304.

Pınar, A., Y. Honkura, and K. Kuge, 2001, "Seismic Activity Triggered by the 1999 İzmit Earthquake and Its Implications for the Assessment of Future Seismic Risk", *Geophysical Journal International,* Vol. 146, pp. F1–F7.

Pınar, A., K. Kuge, and Yoshimori Honkura, 2003, "Moment Tensor Inversion of Recent Small to Moderate Sized Earthquakes: Implications for Seismic Hazard and Active Tectonics beneath the Sea of Marmara", *Geophysical Journal International,* pp. 133-145.

Pınar, A., S. B. Ucer, Y. Honkura, N. Sezgin, A. Ito, S. Baris, D. Kalafat, M. Matsushima, and S. Horiuchi, 2009, "Spatial Variation of Stress Field Along the Fault Rupture Zone of the 1999 İzmit Earthquake", *Earth, Planets and Space,* pp. 1-14.

Pınar, A., Z. Coşkun, A. Mert, and D. Kalafat, 2016, "Frictional Strength of North Anatolian fault in Eastern Marmara Region", *Earth, Planets and Space*, Vol. 68, No. 62 DOI: 10.1186/s40623-016-0435-z.

Polat, O., H. Haessler, A. Cisternas, H. Philip, H. Eyidogan, M. Aktar, M. Frogneux, D. Comte, and C. Gürbüz, 2002, "The İzmit (Kocaeli), Turkey Earthquake of 17 August 1999: Previous Seismicity, Aftershocks, and Seismotectonics", *Bulletin of the Seismological Society of America,* pp. 361-375.

Pondard, N., R. Armijo, G. C. P. King, B. Meyer, and F. Flerit, 2007, "Fault interactions in the Sea of Marmara pull-apart (North Anatolian Fault): earthquake clustering and propagating earthquake sequences", *Geophysical Journal International,* Vol. 171, pp. 1185–1197.

Rangin, C., E. Demirbag, C. Imren, A. Crusson, A. Normand, E. Le Drezen, and A. Le Bot, 2001, "Marine Atlas of the Sea of Marmara (Turkey)", Ifremer, Brest, France.

Reilinger, R., S. McClusky, and P. Vernant, et al., 2006, "GPS constraints on continental deformation in the Africa‑Arabia‑Eurasia continental collision zone and implications for the dynamics of plate interactions", *Journal of Geophysical Research,* DOI:10.1029/ 2005JB004051.

Reilinger, R., S. McClusky, D. Paradissis, S. Ergintav, and P. Vernant, 2010, "Geodetic Constraints on the Tectonic Evolution of the Aegean Region and Strain Accumulation along the Hellenic Subduction Zone ", *Tectonophysics,* pp. 22-30.

Reuter, H. I., A. Nelson, A. Jarvis, 2007, "An Evaluation of Void Filling Interpolation Methods for SRTM Data", *International Journal of Geographic Information Science*, Vol. 21, No. 9, pp. 983-1008.

Rice, J. R., and A. Ruina, 1983, "Stability of Steady Frictional Slipping", *Journal of Applied Mechanics*, Vol. 50, pp. 343-349.

Sakic, P., H. Piete, V. Ballu, J. Y. Royer, H. Kopp, D. Lange, F. Petersen, M. S. Özeren, S. Ergintav, L. Geli, P. Henry, and A. Deschamps, 2016, "No Significant Steady State Surface Creep along the North Anatolian Fault offshore Istanbul: Results of 6months of Seafloor Acoustic Ranging", *Geophysical Research Letters*, DOI: 10.1002/2016GL069600.

Sato, T., J. Kasahara, T. Taymaz, M. Ito, A. Kamimura, T. Hayakawa, and O. Tan, 2004, "A Study of Microearthquake Seismicity and Focal Mechanisms within the Sea of Marmara (NW Turkey) Using Ocean Bottom Seismometers (OBSs)", *Tectonophysics,* pp. 303-314.

SCEC, web page, 2019 May 27, http://scecdata.usc.edu/cvws/cgi-bin/cvws.cgi.

Schmittbuhl, J., H. Karabulut, O. Lengline, and M. Bouchon, M., 2015, "Seismicity Distribution and Locking Depth along the Main Marmara Fault, Turkey", *Geochemistry, Geophysics, Geosystems*, DOI: 10.1002/2015GC006120.

Schmittbuhl, J., H. Karabulut, O. Lengline, and M. Bouchon, 2016, "Long-Lasting Seismic Repeaters in the Central Basin of the Main Marmara Fault", *Geophysical Research Letters*, DOI: 10.1002/2016GL070505.

Seeber, L., O. Emre, M. H. Cormier, C. C. Sorlien, C. M. G. McHugh, A. Polonia, N. Ozer, and N. Cagatay, 2004, "Uplift and Subsidence from Oblique Slip: the Ganos–Marmara Bend of the North Anatolian Transform, Western Turkey", *Tectonophysics,* pp. 239-258.

Siyako, M., T. Tanış, and F. Şaroğlu, 2000, "Marmara Denizi Aktif Fay Geometrisi", *TUBITAK, Bilim Teknik Dergisi,* Vol. 388, pp. 66-71.

Sosyal, H., S. Sipahioğlu, D. Kolçak, and Y. Altınok, "Türkiye ve Çevresinin Tarihsel Deprem Kataloğu, (M.O. 2100 - M.S. 1900)", *TÜBİTAK Proje No: TBAK-341*, İstanbul, 1981.

Şaroğlu, F., Ö. Emre, and İ. Kuşçu, "Active Fault Map of Turkey at Scale 1:1 000 000, Mineral Research and Explorations Institute of Turkey Publication", Ankara, 1992.

Suppe, J., "Fluid Overpressures and Strength of the Sedimentary upper Crust", 2014, *Journal of Structural Geology* , http://dx.doi.org/10.1016/j.jsg.2014.07.009.

Şengör, A.M.C., N. Görür, and F. Saroglu, 1985, "Strike-slip faulting and related Basin formation in zones of tectonic escape: Turkey as a case study. In: Biddle, K.T., Christie-Blick, N. (Eds.), Strike-slip Faulting and Basin Formation:" *Society of Econ. Paleont. Min. Sec. Pub.,* Vol. 37, pp. 227–264.

Şengör, A. M. C., O. Tüysüz, C. İmren, M. Sakınç, H. Eyidoğan, N. Görür, X. Le Pichon, and C. Rangin, 2005, "The North Anatolian Fault: a new look", *Annual Reviews of Earth and Planetary Sciences*, Vol. 33, pp. 37-112.

Tanircan, G., L. Dalguer, F. N. Bekler, and N. Meral Özel, 2017, "Dynamic Rupture Modelling of the 1999 Du̇zce, Turkey Earthquake", *Pure and Applied Geophys*ics, Vol. 174, pp. 3343–3355.

Taymaz, T., J. A. Jackson, and D. McKenzie, 1991, "Active Tectonics of the North and Central Aegean Sea", *Geophysical Journal International*, Vol. 106, pp. 433-490.

Tinti, E., Bizzarri, A., Piatanesi, A., Cocco, M., 2004, "Estimates of slip weakening distance for different dynamic rupture models", *Geophysical Research Letters,* Vol. 31, No. L02611, DOI: 10.1029/ 2003GL018811.

Tsuda, K., S. Iwase, H. Uratani, S. Ogawa, T. Watanabe, J. Miyakoshi, and J. P. Ampuero, 2017, "Dynamic Rupture Simulations Based on the Characterized Source Model of the 2011 Tohoku Earthquake", *Pure and Applied Geophysics*, DOI: 10.1007/s00024-016-1446-1.

Tunç, B., D. Çaka, T. S. Irmak, H. Woith, S. Tunç, Ş. Bariş, M. F. Özer, B. G. Lühr, E. Günther, H. Grosser, and J. Zschau, 2011, "The Armutlu Network: An Investigation

into the Seismotectonic Setting of Armutlu-Yalova-Gemlik and the Surrounding Regions", *Annals of Geophysics,* DOI: 10.4401/ag-4877.

Uchida, N., A. Pınar, and D. Kalafat, 2018, "Repeating earthquakes and interplate coupling along the North Anatolian Fault", Japan Geoscience Union Meeting.

Uçarkuş, G., Z. Çakır, and R. Armijo, 2011, "Western Termination of the Mw 7.4, 1999 İzmit Earthquake Rupture: Implications for the Expected Large Earthquake in the Sea of Marmara", *Turkish Journal of Earth Sciences,* Vol. 20, pp. 379–394, DOI: 10.3906/yer-0911-72.

Uchida, N., A. Pınar, and D. Kalafat, 2019, "Repeating earthquakes and interplate coupling along the North Anatolian Fault", SCG53-P15.

Waldhauser, F., 2001, "HYPODD -- A Program to Compute Double-Difference Hypocenter Locations".

Waldhauser, F., W. L. Ellsworth, 2000, "A double-difference earthquake location algorithm: Method and application to the northern Hayward fault", *Bulletin of the Seismological Society of America*, Vol. 90, pp. 1353-1368.

Wollin, C., M. Bohnhoff, M. Patricia, K. Ludger, and R. Christina, 2018, "A unified earthquake catalogue for the Sea of Marmara Region, Turkey, based on automatized phase picking and travel-time inversion: Seismotectonic implications", *Tectonophysics,* pp.416-444.

Wong, H. K., T. Lüdmann, A. Uluğ, and N. Görür, 1995, "The Sea of Marmara: a plate boundary sea in an escape tectonic regime", *Tectonophysics*, Vol. 244, pp. 231-250.

Wright, T., E. Fielding, and B. Parsons, 2001, "Triggered Slip: Observations of the 17 August 1999 İzmit (Turkey) Earthquake Using Radar Interferometry", *Geophysical Research Letters,* Vol. 28, pp. 1079– 1082, DOI: 10.1029/2000GL011776.

Yaltırak, C., 2002, "Tectonic evolution of the Marmara Sea and its surroundings", *Marine Geology,* Vol. 190, pp. 493-529.

Yamamoto, Y., N. Takahashi, S. Citak, D. Kalafat, A. Pinar, C. Gurbuz, and Y. Kaneda 2015, "Offshore seismicity in the western Marmara Sea, Turkey, revealed by ocean bottom observation", Earth Planets Space, 67, 147, DOI:10.1186/s40623-015-0325-9.

Yamamoto, R., M. Kido, Y. Ohta, N. Takahashi, Y. Yamamoto, D. Kalafat, A. Pinar, S. Ozeren , and Y. Kaneda, 2016, "Creep rate measurement and fault modelling at the North Anatolian Fault, beneath the Sea of Marmara, Turkey, by means of acoustic ranging, paper presented at Japan Geoscience Union meeting 2016", Chiba, Japan, S-CG59-07.

Yamamoto,Y., N. Takahashi, A. Pınar, D. Kalafat, S. Citak, M. Comoglu, R. Polat, and Y. Kaneda, 2017, "Geometry and segmentation of the North Anatolian Fault beneath the Marmara Sea, Turkey, deduced from long-term ocean bottom seismographic observations", *Journal of Geophysical Research: Solid Earth*, Vol. 122, pp. 2069-2084, DOI: 10.1002/2016JB013608.

Yamamoto, R., M. Kido, Y. Ohta, N. Takahashi, Y. Yamamoto, A. Pinar, D. Kalafat, H. Özener, and Y. Kaneda, 2019, "Seafloor geodesy revealed partial creep of the North Anatolian Fault submerged in the Sea of Marmara", *American Geophysical Union*, DOI: 10.1029/2018GL080984.

Zachariasen, J., and K. Sieh, 1995, "The Transfer of Slip between, En Echelon Strike-Slip Faults: A Case Study from the 1992 Landers Earthquake, Southern California", *Journal of Geophysical Research,* Vol. 100-15, pp. 281-301.